Numerical and Experimental Modelling of an Oscillating Wave Surge Converter Model in Partially Standing Wave Fields

by

Bryce Bocking
B. Eng., University of Victoria, 2014

A Thesis Submitted in Partial Fulfillment
of the Requirements for the Degree of

MASTER OF APPLIED SCIENCE

in the Department of Mechanical Engineering

Numerical and Experimental Modelling of an Oscillating Wave Surge Converter Model in Partially Standing Wave Fields

by

Bryce Bocking
B. Eng., University of Victoria, 2014

Supervisory Committee

Dr. Brad Buckham, Department of Mechanical Engineering

Co-Supervisor

Dr. Peter Oshkai, Department of Mechanical Engineering

Co-Supervisor

Abstract

Supervisory Committee

Dr. Bradley Buckham, Department of Mechanical Engineering

Supervisor

Dr. Peter Oshkai, Department of Mechanical Engineering

Co-Supervisor

In the field of ocean wave energy converters (WECs), active areas of research are on a priori or in situ methods for power production estimates and on control system design. Linear potential flow theory modelling techniques often underpin these studies; however, such models rely upon small wave and body motion amplitude assumptions and therefore cannot be applied to all wave conditions. Nonlinear extensions can be applied to the fluid loads upon the structure to extend the range of wave conditions for which these models can provide accurate predictions. However, careful consideration of the thresholds of wave height and periods to which these models can be applied is still required. Experimental modelling in wave tank facilities can be used for this purpose by comparing experimental observations to numerical predictions using the experimental wave field as an input.

This study establishes a recommended time domain numerical modeling approach for power production assessments of oscillating wave surge converters (OWSCs), a class of WEC designed to operate in shallow and intermediate water depths. Three candidate models were developed based on nonlinear numerical modelling techniques in literature, each with varying levels of complexity. Numerical predictions provided by each model were found to be very similar for small wave amplitudes, but divergence between the models was observed as wave height increased.

Experimental data collected with a scale model OWSC for a variety of wave conditions was used to evaluate the accuracy of the candidate models. These experiments were conducted in a small-scale wave flume at the University of Victoria. A challenge with this experimental work was managing wave reflections from the boundaries of the tank, which were significant and

impacted the dynamics of the scale model OWSC. To resolve this challenge, a modified reflection algorithm based upon the Mansard and Funke method was created to identify the incident and reflected wave amplitudes while the OWSC model is in the tank. Both incident and reflected wave amplitudes are then input to the candidate models to compare numerical predictions with experimental observations.

The candidate models agreed reasonably well with the experimental data, and demonstrated the utility of the modified wave reflection algorithm for future experiments. However, the maximum wave height generated in the wave tank was found to be limited by the stroke length of the wavemaker. As a result, no significant divergence of the candidate model predictions from the experimental data could be observed for the limited range of wave conditions, and therefore a recommended model could not be selected based solely on the experimental/numerical model comparisons.

Preliminary assessments of the annual power production (APP) for the OWSC were obtained for a potential deployment site on the west coast of Vancouver Island. Optimal power take-off (PTO) settings for the candidate models were identified using a least-squares optimization to maximize power production for a given set of wave conditions. The power production of the OWSC at full scale was then simulated for each bin of a wave histogram representing one year of sea states at the deployment site. Of the three candidate models, APP estimates were only obtained for Model 1, which has the lowest computational requirements, and Model 3, which implements the most accurate algorithm for computing the fluid loads upon the OWSC device. Model 2 was not considered as it provides neither advantages of Models 1 and 3.

The APP estimates from Models 1 and 3 were 337 and 361 MWh per year. For future power production assessments, Model 3 is recommended due to its more accurate model of the fluid loads upon the OWSC. However, if the high computational requirements of Model 3 are problematic, then Model 1 can be used to obtain a slightly conservative estimate of APP with a much lower computational effort.

Table of Contents

List of Tables

List of Figures

Nomenclature

Acronyms

APP	Annual power production
BEM	Boundary element method
CFD	Computational fluid dynamics
FSI	Fluid-structure interaction
OWSC	Oscillating wave surge converter
PIV	Particle image velocimetry
PTO	Power take-off
RAO	Response amplitude operator
SPH	Smooth particle hydrodynamics
THD	Total harmonic distortion

Symbols

A	Complex wave amplitude
A_c	Added inertia coefficient
A_∞	Infinite added inertia coefficient: $A_\infty = \lim_{\omega \to \infty} A_c(\omega)$
A_I	Complex incident wave amplitude
A_R	Complex reflected wave amplitude
A^*	Correction to the added inertia coefficient
B_c	Radiation damping coefficient
C	Hydrostatic stiffness coefficient
C_d	Empirical drag coefficient
C_g	Group velocity
C_m	Empirical inertia coefficient

C_p	Phase velocity
D	Characteristic length scale
E	Error function
E_A	Error in the incident wave amplitude
E_{rel}	Relative error between numerical predictions and experimental observations
E_{res}	Error in the residuals of the wave reflection algorithm
E_{amp}	Error in the amplitude of the numerical model prediction
E_{phase}	Error in the phase of the numerical model prediction
E_β	Relative difference between the optimal power take-off damping coefficients obtained from linear and nonlinear numerical models
E_θ	Error between numerical and experimental pitch response amplitude spectra
H	Wave height: $H = 2A$
H^*	Commanded wave height
H_b	Breaking wave height limit
I	Inertia about hinge axis
$\mathbf{J}$	Jacobian matrix
K	Z-transform of the radiation impulse response function
K_R	Reflection coefficient: $K_R = \lvert A_R \rvert / \lvert A_I \rvert$
KC	Keulegan-Carpenter number. $KC = u_a T / D$
L_C	Capture width
M_{FK}	Froude-Krylov moment
M_S	Scattered wave moment
M_e	Total wave excitation moment: $M_e = M_{FK} + M_S$
M_b	Buoyancy moment
M_g	Gravity moment
M_d	Drag moment
M_{ext}	External moment
M_f	Friction moment
M_{PTO}	Power take-off moment
M_m	Measured moment

$\hat{M}_m$	Fourier transform of the measured moment
M_{num}	Numerical model prediction for the total wave moment
M_i	Regular wave hours of occurrence corresponding to histogram bin *i*
M_{tot}	Total number of regular wave hours of occurrence
N_p	Number of wave probes
N_q	Number of Gaussian quadrature points
N_1, N_2, N_3, N_4	Shape functions
N_i	Irregular wave hours of occurrence in histogram bin *i*
$\bar{P}$	Mean power generated by the power take-off
$\bar{P}_w$	Mean power per unit wave crest
R	Rotation matrix
Re	Reynolds number. $\mathrm{Re} = u_a D / \nu$
S	Wetted body surface or wavemaker stroke
$S(\omega)$	Variance density spectrum
$S_{PM}(\omega)$	Pierson-Moskowitz spectrum
T_e	Energy period
T_p	Peak period
THD	Total harmonic distortion
W	Weight factor or body width
X	Spectral component of the wavemaker motion profile for irregular wave generation
X_{FK}	Complex Froude-Krylov moment amplitude in regular waves of unit amplitude
X_R	Complex radiation moment amplitude for regular pitch motion of unit amplitude
X_S	Complex scattered wave moment amplitude in regular waves of unit amplitude
$\forall$	Wetted body volume
a_I, b_I	Real and imaginary components of the incident wave amplitude: $A_I = a_I + ib_I$
a_R, b_R	Real and imaginary components of the reflected wave amplitude: $A_R = a_R + ib_R$
d	Water depth

dA	Element of body cross-sectional area
dS	Element of wetted body surface
$d\forall$	Element of wetted body volume
g	Gravity constant
$\vec{i}, \vec{j}, \vec{k}$	Unit vectors in x, y, z directions
k	Wave number or radiation impulse response function
k_e	Inverse Fourier transform of the complex amplitudes of the total wave excitation moment in regular waves
k_S	Inverse Fourier transform of the complex amplitudes of the total wave excitation moment in regular waves
$\hat{k}$	Fourier transform of the radiation impulse response function
m	Mass
m_n	Spectral moment of n^{th} order
$\vec{n}$	Normal vector, pointing towards interior of body
p	Gauge fluid pressure
p_{dyn}	Dynamic fluid pressure
p_R	Dynamic pressure due to wave radiation
p_S	Dynamic pressure due to wave scattering
$\vec{p}_k$	Position of panel corner k relative to hinge axis
$\vec{q}$	Position of Gaussian quadrature point relative to hinge axis
q_x, q_y, q_z	Components of the quadrature point position vector
$\vec{r}$	Position vector relative to hinge axis
r	Distance from hinge axis
r_b	Distance of centre of buoyancy from hinge axis
r_g	Distance of centre of gravity from hinge axis
s, t	Natural coordinates
t	Time
t_s	Sample rate
$\vec{u}$	Fluid velocity vector
$\vec{u}_r$	Relative velocity vector
u, v, w	Fluid velocity components

u_a	Fluid velocity amplitude in the x direction
u_n	Fluid velocity normal to body
u_b	Body velocity in the x direction
x, y, z	Global reference frame coordinates
x_p, y_p	Wave probe coordinates
x', y', z'	Panel fixed reference frame coordinates (y' is normal to the panel)
Φ	Velocity potential
Φ_0	Velocity potential of incident wave
Φ_R	Velocity potential of radiated wave
Φ_S	Velocity potential of scattered wave
Φ_D	Velocity potential of diffracted wave: $\Phi_D = \Phi_0 + \Phi_S$
α, β	Real and imaginary components of the pitch response amplitude operator: $\hat{\theta} = \alpha + i\beta$
α_m, β_m	Real and imaginary components of the Fourier transform of the measured pitch motion: $\hat{\theta}_m = \alpha_m + i\beta_m$
β	Power take-off damping coefficient
β_{opt}	Optimal power take-off damping coefficient
β_{linear}	Optimal power take-off damping coefficient obtained from a linear numerical model
$\beta_{nonlinear}$	Optimal power take-off damping coefficient obtained from a nonlinear numerical model
β_b	Brake damping coefficient
ε	Residual error
η	Free surface elevation
η_c	Free surface elevation at panel centroid
$\hat{\eta}$	Fourier transform of the free surface elevation
$\hat{\eta}_n^{(p)}$	Component *n* of the Fourier transform of free surface measured by wave probe *p*
$\hat{\eta}_{D+}^{(p)}$	Complex amplitude of the diffracted wave at probe *p* produced by a regular wave of unit amplitude propagating in the positive *x* direction
$\hat{\eta}_{D-}^{(p)}$	Complex amplitude of the diffracted wave at probe *p* produced by a regular wave of unit amplitude propagating in the negative *x* direction

$\hat{\eta}_R^{(p)}$	Complex amplitude of the radiated wave at probe *p* produced by regular pitch motion of unit amplitude
$\theta, \dot{\theta}, \ddot{\theta}$	Pitch angle, angular velocity and angular acceleration
$\hat{\theta}$	Pitch response amplitude in regular waves, or the pitch response amplitude operator
θ_m	Measured pitch motion
$\hat{\theta}_n$	Component *n* of the Fourier transform of the measured pitch motion
θ_{num}	Numerical model prediction for pitch motion
$\hat{\theta}_{num}$	Fourier transform of the numerical model prediction for pitch motion
θ_{bi}	Pitch angle at which the braking moment begins to engage
θ_{bf}	Pitch angle at which the braking moment is fully engaged
λ	Wavelength
ρ	Density
φ	Phase offset
ω	Angular frequency
ω^*	Commanded wave frequency

Acknowledgments

I would like to thank everyone who supported me along the way to completing this thesis. Thanks to my supervisors Dr. Buckham and Dr. Oshkai for their knowledge and expertise, and for inspiring me to pursue such an interesting avenue of research. In addition, thank you to Dr. Bailey and Dr. Robertson for their knowledge and expertise in ocean waves and hydrodynamics, Rodney Katz for his valuable expertise in design and manufacturing, and Mostafa Rahimpour for his assistance and guidance in the flume tank. Thank you all for putting up with my many questions, without all your help this thesis would not have been possible.

Thanks to all my friends in the WCWI and IESVic research groups for making this research such a fun experience. And finally, thanks to my amazing wife Richelle and my family for your love and support, and for tolerating my grad student life for all these years.

This research would not have been possible without the financial assistance provided by the Natural Sciences and Engineering Research Council of Canada (NSERC).

Dedication

To Logan and Kenzie.

Chapter 1: Introduction

As global energy demands increase, there is a need to diversify the portfolio of available energy production methods. Combined with the need to reduce global greenhouse gas emissions, this situation puts emphasis on developing clean, renewable forms of energy production. For renewable energy sources to penetrate the global energy market to the degree needed to mitigate climate change, all available renewable sources will have to be utilized. A diverse collection of clean energy technologies is required to ensure that at any specific location on the planet, renewable energy is harnessed no matter the form of the locally dominant renewable option. For coastal communities, which account for around 37% of the global population (within 90km of the coast) [1], ocean wave energy has the potential to satisfy a significant portion of energy demands. The west coast of Canada is a particularly promising location for wave energy technology development as it features one of the most energetic wave climates in the world, receiving on average 40-50 kW of wave power per meter of wave crest [2].

Wave energy converters (WECs) aim to convert the mechanical energy of ocean waves into a useful commodity - electricity and desalinated water being prime examples [3]. Many classes of WECs exist, and while numerous studies have been conducted to compare the performance of these classes ([4], [5]), there has yet to be convergence to an industry standard design. This is in part because each class of device works off a different dynamic phenomenon within the water wave and thus each is the preferred technology for certain environmental conditions. For example, point absorbers operate in heave and utilize circular water orbitals beneath waves in deep water, while oscillating wave surge converters (OWSCs) operate in shallow water and utilize the large

horizontal accelerations from the elliptic orbitals occurring beneath shallow water waves [6]. The various classes of WEC devices therefore form their own diverse portfolio of technology options that can be drawn upon to ensure that the most suitable device is deployed at a given location based upon environmental properties such as water depth, the prominent wave periods and the variability in the principle direction of the wave propagation.

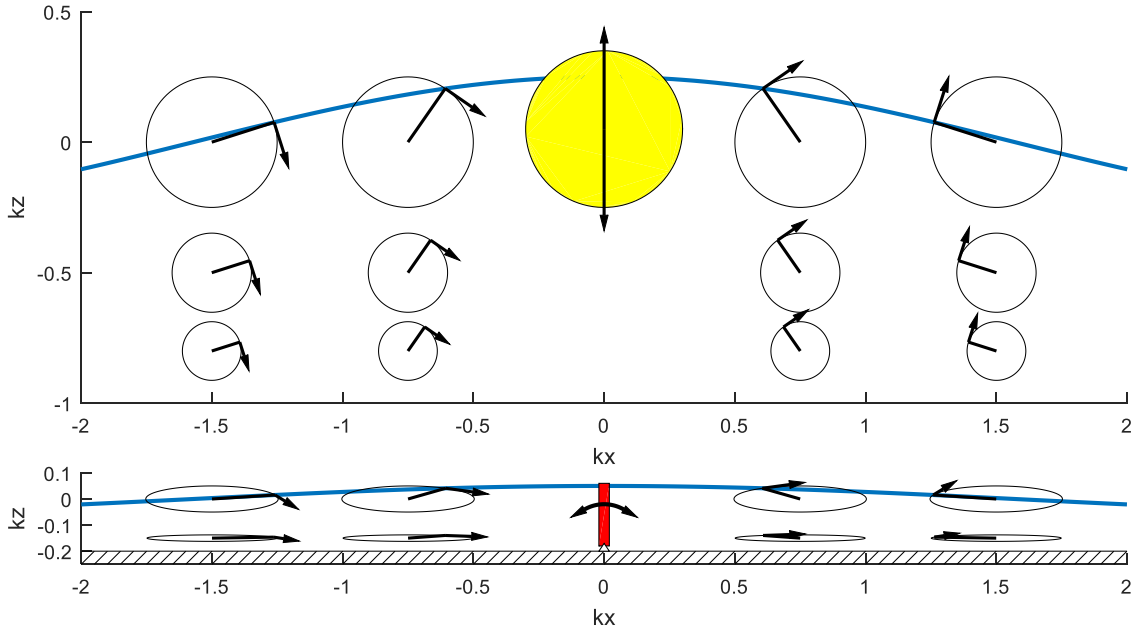

Figure 1-1: Water orbitals and primary directions of motion for point absorbers in deep water (top in yellow) and OWSCs in shallow water (bottom in red). The arrows on each orbital indicates the direction of fluid motion.

1.1 Motivation

To date, there are many unanswered questions related to WEC design, such as optimal control strategies for maximizing power output, and predicting maximum wave loads on WEC structures. Much of the current research into wave energy converter technology is focused on addressing these problems using numerical modelling techniques. Each problem requires a different approach. For example, short term simulations in extreme conditions use fully nonlinear solvers such as CFD

and SPH to complete survivability analyses (determine the maximum structural loads) [7]–[9]. However, their high computation requirements make them less suitable for long-term simulations for power production estimates or for designing optimal control systems. Alternatively, for performance assessments that consider less extreme wave heights, and thus lower fluid velocities, the overall fluid loading on the WEC due to the complete fluid-structure interaction (FSI) can be approximated as a superposition of various force layers, such as buoyancy, radiation damping and viscous drag. Each layer represents a hydrodynamic phenomenon known to contribute to the actual FSI problem and defines a component force acting on the body in terms of the body and fluid flow kinematics.

The definition of the force contributed by each layer is usually available in a simplified form for common body geometries or through experimental trials that establish explicit semi-empirical expressions for specific geometries. This type of analysis assumes that the simplified solutions for each layer are independent. For example, the viscous drag force arises from flow separation about the submerged body, while the radiation forces are based on the premise that flow separation does not occur. In reality, these layers are not independent and the superposition of these layers is subject to error. The level of error changes in different wave conditions; structures in small amplitude waves are typically modelled quite well by this approach, but the layer approximations, as well as the accuracy of the superposition of these layers, break down in extreme (large wave height) sea states [10].

The simplified solutions for the layers of the FSI problem are often applied under small amplitude wave and body motion assumptions so that the resulting forces for each layer are linear in terms of the body or flow velocity and acceleration. However, WECs are typically designed to experience large amplitude motions and are deployed in energetic wave climates where large wave heights often occur. Recent studies have shown that designing control systems using fully linear models can lead to less efficient power production when implemented in actual physical systems experiencing significant non-linear forces [11]. Many recent models of WECs have therefore implemented nonlinear extensions to the dominant layers of the FSI problem, where the fluid loads are computed using the instantaneous wetted surface of the body rather than the mean wetted surface [12]–[14].

Experimental study of physical scale models in wave tanks is a necessary component of WEC development. Scale model studies are commonly used to identify the coefficients fundamental to the semi-empirical representations of the non-linear hydrodynamic effects such as drag, to validate assembled numerical models and identify any hydrodynamic effects missing from the model. Real world sea states can be difficult to replicate in wave tanks as the waves are generated in a bounded domain, resulting in wave reflections from the tank walls. While large facilities can mitigate this problem by implementing advanced passive or active wave absorption techniques, they are often costly to use making it infeasible for some WEC developers to test their designs. On the other hand, smaller facilities may be cheaper to use, but are prone to undesired fluid motions due to wave reflections that pollute the measured forces and motions on the model and must be accounted for.

The University of Victoria uses an existing flume for small scale tests of an OWSC device. The dimensions of the tank result in unique challenges which must be addressed before the experimental results can be used to validate candidate numerical OWSC models. The main challenge is accounting for reflections from the end of the flume; these reflections combine with the incident waves to produce a partially standing wave profile, where the incident wave height appears to vary across the length of the tank. This introduces uncertainty as to what the true wave height is at the experimental model and thus uncertainty in the derived hydrodynamic coefficients.

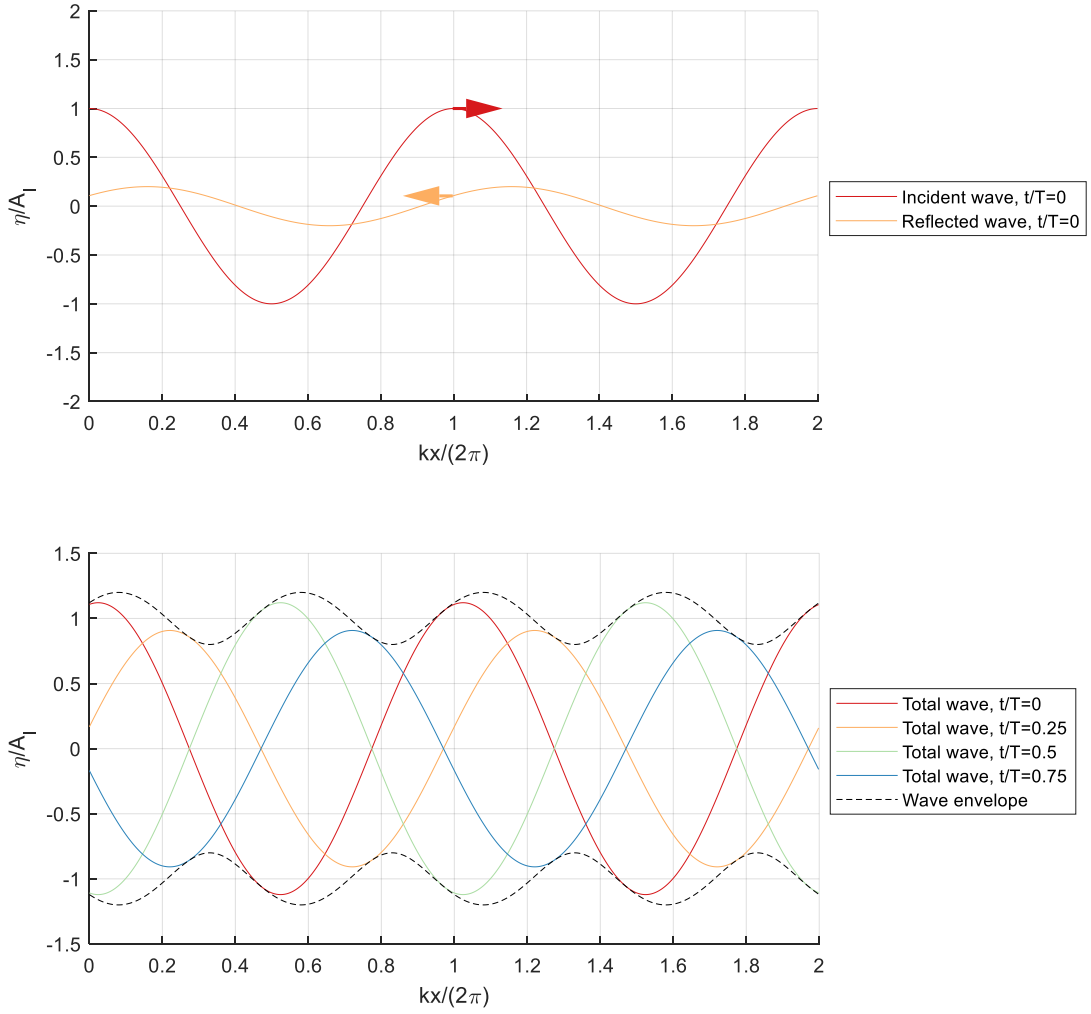

Figure 1-2: A sample partially standing wave field resulting from wave reflections. The top figure shows the unperturbed incident and reflected wave components which constitute the partially standing wave field. The bottom figure shows the total wave elevation at various time instances, along with the wave envelope representing the extreme values of the free surface over the length of the tank. In this example, the amplitude of the reflected wave is 20% of the incident wave amplitude A_I.

1.2 Thesis Objectives

The focus of this thesis is on experimental and numerical modelling of an OWSC device. OWSCs are suitable for shallow and intermediate water conditions (10 to 20m water depths [15]), and are a promising candidate for deploying near shore along the coast of Vancouver Island in British Columbia. Various numerical OWSC models are developed and compared with experimental data to develop a recommended modelling approach to be used in power production assessment exercises for this type of WEC. In the process, annual energy production is estimated at a deployment site near Amphitrite Bank, a promising WEC deployment site[16].

An existing small-scale wave tank at the University of Victoria (UVic) is used to conduct the experimental investigations of the dynamics of the OWSC. Experimental data gathered from scale model trials is used to calculate the coefficients that underpin the various OWSC hydrodynamic force layers, as well as to compare multiple approaches for combining these hydrodynamic layers in a numerical OWSC dynamics model. The candidate models are then used to estimate the annual power production of a single OWSC device at a site off the coast of Vancouver Island.

To properly compare the candidate model predictions with experimental observations, a methodology for analyzing experimental data collected in the small-scale wave tank at UVic must be created that correctly accounts for the presence of wave reflections from the end of the short tank and from the experimental model. Most tank facilities are long so that even if wave reflections are present, a given test can be conducted for a long enough period before these reflections affect the model dynamics. Any data collected after reflections become problematic can then simply be rejected. However, with UVic's tank, the short length causes reflected waves to disturb the model dynamics very early in any trial. Thus, the impact of these reflected waves must be identified and removed from experimental measurements prior to a parameter identification exercise or a comparison with numerical model output.

Existing wave reflection algorithms are designed to calculate incident and reflected wave heights without any objects in the tank. However, when a moving body such as a scale model OWSC is placed in the tank, the wave system is disturbed by additional waves which are radiated and scattered by the body. In this thesis, the wave reflection algorithm must account for the presence of the moving scale model OWSC.

1.3 Background

The following sections introduce the relevant theory for the remainder of the thesis. First, linear (Airy) wave kinematic equations are developed and applied to both irregular sea states in the ocean and partially standing wave systems in wave tanks. The rigid body dynamics of OWSCs are then discussed, along with an overview of the hydrodynamic loads that act upon the device. Relevant literature for each topic is also reviewed in these sections.

1.3.1 Ocean Waves

Airy Wave Kinematics

The profile of a small amplitude, monochromatic ocean wave was originally derived by Airy and Laplace [17]. By assuming small amplitude waves along with incompressible, inviscid and irrotational flow, they solved Laplace's equation for a progressive wave over a flat-bottom seafloor of depth d. The resulting velocity potential for the fluid domain and corresponding free surface profile are [17]:

$$\Phi = \mathrm{Im}\left\{\frac{Ag}{\omega}\frac{\cosh\left(k(z+d)\right)}{\cosh\left(kd\right)}\exp\left[i(kx-\omega t)\right]\right\} \tag{1.1}$$

$$\eta = \mathrm{Re}\left\{A\exp\left[i(kx-\omega t)\right]\right\} \tag{1.2}$$

where A is the wave amplitude, and k is the wave number defined relative to wavelength λ by

$$k = \frac{2\pi}{\lambda}$$

The wavenumber is also related to wave frequency ω by the dispersion relation for gravity water waves [17]:

$$\omega^2 = gk\tanh(kd) \tag{1.3}$$

The dispersion relation can be simplified if deep water ($d/\lambda > 0.5$) or shallow water ($d/\lambda \leq 0.04$) conditions are satisfied. Many of the sea states considered in this thesis do not satisfy either condition: the wave conditions considered at the candidate deployment site, and

recreated in the small scale tank, are intermediate depth waves and therefore the dispersion relation given in Eq. (1.3) is used herein.

The Wave Spectrum

Ocean waves are typically irregular, and are approximated as the superposition of multiple Airy waves with different amplitudes, frequencies and directions. If the sea state is unidirectional, such as in a wave flume, then the fluid velocity potential and free surface elevation can be expressed as:

$$\Phi(x,z,t) = \mathrm{Im}\left\{\sum_n \frac{A_n g}{\omega_n}\frac{\cosh\left(k_n(z+d)\right)}{\cosh\left(k_n d\right)}\exp\left[i\left(k_n x-\omega_n t\right)\right]\right\} \tag{1.4}$$

$$\eta(x,t) = \mathrm{Re}\left\{\sum_n A_n \exp\left[i\left(k_n x-\omega_n t\right)\right]\right\} \tag{1.5}$$

where $k_n = k(\omega_n)$ and A_n is the complex amplitude of the n^{th} spectral component of the wave spectrum, with modulus (magnitude) $|A_n|$ and argument (phase) $\angle A_n$. For a discretely sampled irregular wave profile, the amplitude spectrum is evaluated at discrete frequencies ω_n that are evenly spaced by $\Delta\omega$, which is directly dependent on the duration of the free surface measurements.

Ocean waves are often described by their variance density spectrum $S(\omega)$ rather than a series of amplitudes, periods and phases as in Eq. (1.4) and (1.5). The discrete variance density spectrum $S_n = S(\omega_n)$ is related to the complex amplitude spectrum by [18]:

$$S_n = \frac{|A_n|^2}{2\Delta\omega} \tag{1.6}$$

and has units of $m^2/(rad/s)$. A sample discrete variance density spectrum is shown in Figure 1-3. Note that the variance S_n applies across the entire width $\Delta\omega$ of the bin located at ω_n, and represents the accumulation of variance across waves located within the narrow frequency band of this bin.

A given wave spectrum can be summarized by its significant wave height H_s and energy period T_e, defined as [18], [19]:

$$H_s = 4.004\sqrt{m_0} \tag{1.7}$$

$$T_e = 2\pi \frac{m_0}{m_1} \tag{1.8}$$

where m_k is the k^{th} spectral moment given by [18]

$$m_k = \sum_{n=1}^{N} \omega_n^k S_n \Delta\omega \tag{1.9}$$

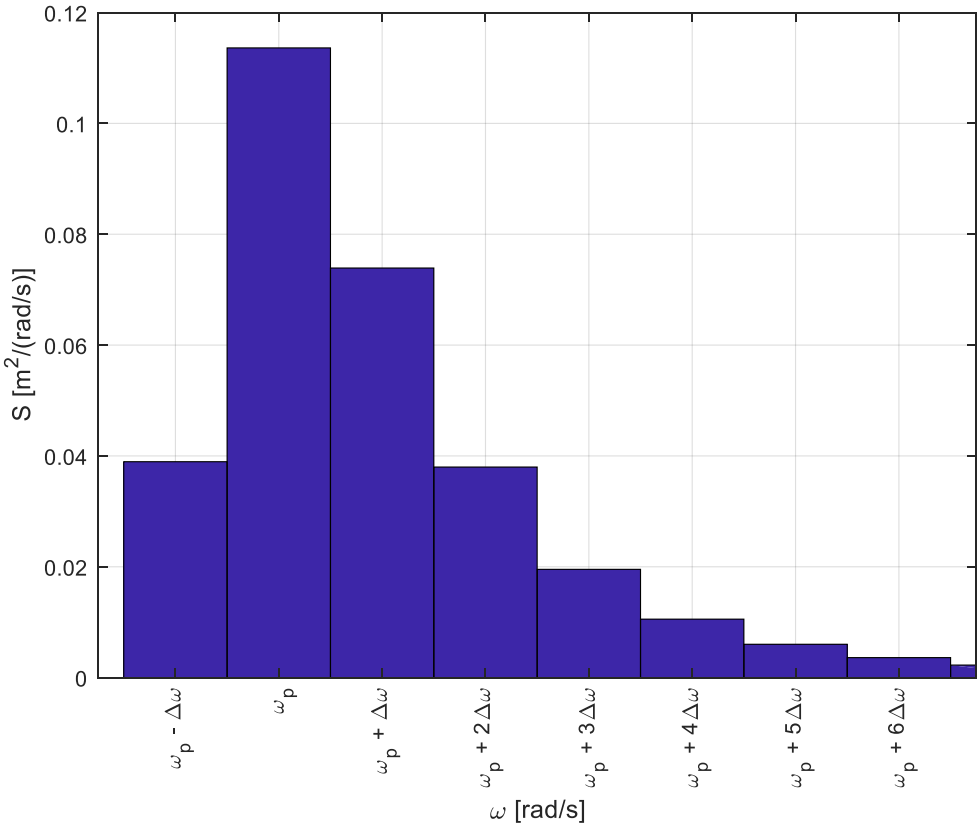

Figure 1-3: Sample variance density spectrum illustrating the definition of the peak period $T_p = 2\pi/\omega_p$. This sample is produced from a Pierson-Moskowtiz model with $H_s = 1\ m$, $T_p = 8\ s$ and $\Delta\omega = 0.2\ rad/s$.

Instead of energy period, irregular waves can also be described in terms of peak period T_p, which is the wave period corresponding to frequency at the center of the frequency bin having the maximum value of S_n, as shown in Figure 1-3.

Spectral models such as the Pierson-Moskowitz and JONSWAP spectra have been developed using oceanographic data to recover the shape of the wave spectrum provided scalar values for significant wave height and peak period. For example, the Pierson-Moskowitz spectrum is [20]:

$$S_{PM}(\omega_n) = \frac{5}{16} H_s^2 \omega_p^4 \omega_n^{-5} \exp\left[-\frac{5}{4}\left(\frac{\omega_n}{\omega_p} \right)^{-4} \right] \tag{1.10}$$

where $\omega_p = 2\pi / T_p$. These spectral models can be used to synthesize an irregular wave profile when a free surface time series data is not available. Short-term sea states are generated by randomly selecting the magnitude of each spectral component A_n using a Rayleigh distribution whose mean square value is given by [18]:

$$E\left[|A_n|^2 \right] = 2 S_n \Delta\omega \tag{1.11}$$

The phase $\angle A_n$ for each spectral component is randomly selected from the interval $[0, 2\pi]$. Equation (1.5) can then be used to simulate the free surface.

1.3.2 Experimental Waves

Waves produced in wave tanks differ from ocean wave systems due to the bounded fluid domain, resulting in wave reflections from the walls of the tank. This section presents reflection algorithms for separating wave profiles into incident and reflected components, and then proves analytical expressions for the fluid properties (pressure and velocity) for these wave systems.

Wave Reflection Algorithms

A partially standing wave field consists of two waves of the same period but different amplitudes propagating in opposite directions. Such wave fields arise when a wave encounters some sort of obstacle, resulting in a reflected wave propagating in the opposite direction. If the incident wave

is regular with complex amplitude A_I, and the complex amplitude of the reflected wave is A_R, then the free surface profile is given by

$$\eta(x,t) = \mathrm{Re}\left\{A_I \exp\left[i(kx-\omega t)\right]\right\} + \mathrm{Re}\left\{A_R \exp\left[i(-kx-\omega t)\right]\right\} \tag{1.12}$$

Note the negative sign in front of k for the reflected wave due to the negative propagation direction. In addition, the phases of the incident and reflected waves, $\angle A_I$ and $\angle A_R$, can be different due to the reflection process [21].

The significance of wave reflections is quantified by the reflection coefficient, defined as

$$K_R = \frac{|A_R|}{|A_I|} \tag{1.13}$$

If the reflection coefficient is unity, i.e. the magnitudes of the incident and reflected wave amplitudes are equal, then the wave system is fully standing. Otherwise a partially standing wave arises, where the incident wave appears to vary in height as it propagates. Both systems are illustrated in Figure 1-4, which plots the wave envelope for fully and partially standing wave fields.

Partially standing waves commonly arise in tank testing environments due to reflections from the end of the tank. These reflections are problematic as they cause the wave height at a certain location to become uncertain. Reflections can be mitigated with passive wave absorbing beaches or active wave absorption systems, and well-designed systems can achieve reflection coefficients of under 5% [20].

Reflection algorithms developed by Goda and Suzuki [22] and Mansard and Funke [23] can be used to calculate the reflected wave amplitude given two or more wave probes, assuming all probes are placed between the wavemaker and the source of the wave reflections. While the Goda and Suzuki reflection algorithm requires only two wave probes, careful consideration of the probe spacing is required to avoid large errors. The Mansard and Funke method builds upon Goda and Suzuki's method by adding a third probe and using a least squares minimization procedure to obtain the incident and reflected wave components with reduced error. That algorithm can be

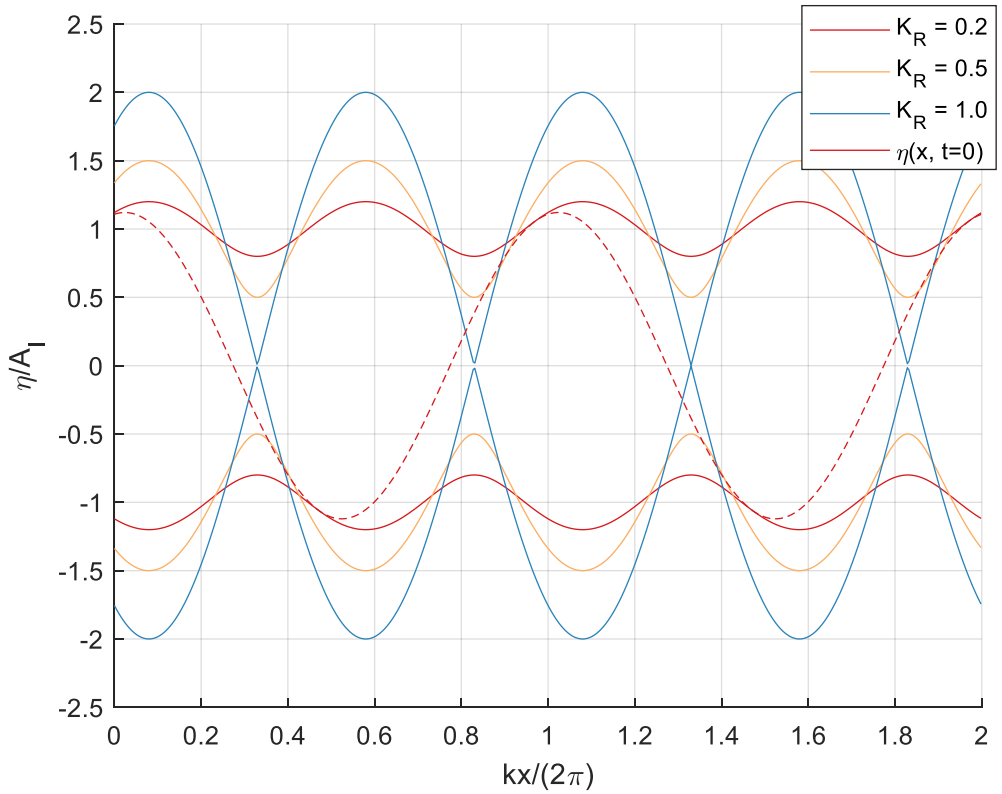

Figure 1-4: Sample wave envelope for three different reflection coefficients. The wave envelopes are normalized by A_I, the amplitude of the incident wave. The dashed line shows a sample free surface profile at $t = 0$ for $K_R = 0.2$.

generalized for an arbitrary number of probes N_p to further reduce measurement errors. Ultimately the objective is to find the complex amplitudes $A_{I,n} = A_I(\omega_n)$ and $A_{R,n} = A_R(\omega_n)$ that minimize the least-squares error between the wave probe measurement and (1.12):

$$\min_{A_I, A_R} \sum_{p=1}^{N_p} \left[\hat{\eta}_n^{(p)} - A_{I,n} \exp\left(ik_n x_p\right) - A_{R,n} \exp\left(-ik_n x_p\right) \right]^2 \tag{1.14}$$

where $\hat{\eta}_n^{(p)} = \hat{\eta}^{(p)}(\omega_n)$ is the n^{th} component of the discrete Fourier transform of the free surface measured by wave probe p, and x_p is the probe location. The solution is obtained from the following system of equations:

$$\begin{bmatrix} \sum_{p=1}^{N_p} \exp(2ik_n x_p) & N_p \\ N_p & \sum_{p=1}^{N_p} \exp(-2ik_n x_p) \end{bmatrix} \begin{bmatrix} A_{I,n} \\ A_{R,n} \end{bmatrix} = \begin{bmatrix} \sum_{p=1}^{N_p} \hat{\eta}_n^{(p)} \exp(ik_n x_p) \\ \sum_{p=1}^{N_p} \hat{\eta}_n^{(p)} \exp(-ik_n x_p) \end{bmatrix} \tag{1.15}$$

This optimization is performed for each spectral component *n* in the Fourier transform of the measured free surface profiles $\hat{\eta}^{(p)}$. Note however that at some frequencies, Eq. (1.15) can become indeterminate depending on the relative position of the wave probes [23]. Probe spacing therefore requires careful consideration to ensure singularities do not arise at wave frequencies of interest. This problem can be mitigated by further increasing the number of wave probes.

Partially Standing Wave Kinematics

The partially standing wave field given in Eq. (1.12) applies if the incident and reflected waves are both regular. More general expressions for partially standing wave fields consisting of multiple wave segments can be obtained by extending the summation in Eq. (1.4) and (1.5) to include negative indices *n*. The negative indices *n* correspond to reflected wave segments, while the positive indices correspond to incident waves:

$$\Phi(x,z,t) = \mathrm{Im}\left\{ \sum_n \frac{A_n g}{\omega_n} \frac{\cosh\left(\tilde{k}_n (z+d)\right)}{\cosh\left(\tilde{k}_n d\right)} \exp\left[i\left(\tilde{k}_n x - \omega_n t\right)\right] \right\} \tag{1.16}$$

$$\eta(x,t) = \mathrm{Re}\left\{ \sum_n A_n \exp\left[i\left(\tilde{k}_n x - \omega_n t\right)\right] \right\} \tag{1.17}$$

$$A_n = \begin{cases} A_{I,n} & n > 0 \\ 0 & n = 0 \\ A_{R,n} & n < 0 \end{cases} \tag{1.18}$$

$$\omega_n = |n| \Delta\omega \tag{1.19}$$

$$\tilde{k}_n = \begin{cases} k_n & n \geq 0 \\ -k_n & n < 0 \end{cases} \tag{1.20}$$

Note the negative sign in Eq. (1.20) ensures that the reflected wave segments propagate in the negative *x* direction.

Dynamic fluid pressure (gauge) and velocity are related to the velocity potential function in the fluid domain by [17]:

$$p_{dyn} = -\rho \frac{\partial \Phi}{\partial t} \tag{1.21}$$

$$\vec{u} = \nabla \Phi \tag{1.22}$$

The total (gauge) fluid pressure can then be obtained from the summation of dynamic and hydrostatic fluid pressures:

$$p = p_{dyn} - \rho g z \tag{1.23}$$

Expressions for pressure and velocity can then be obtained from the velocity potential function in Eq. (1.16). For a partially standing irregular wave field, the combined summation of incident and reflected wave segments results in the following expressions for fluid pressure and velocity:

$$p_{dyn}(x,z,t) = \rho g \,\mathrm{Re}\left\{ \sum_{n=-N}^{N} A_n \frac{\cosh\left(\tilde{k}_n (z+d)\right)}{\cosh(\tilde{k}_n d)} \exp\left[i(\tilde{k}_n x - \omega_n t) \right] \right\} \tag{1.24}$$

$$u(x,z,t) = \mathrm{Re}\left\{ \sum_{n=-N}^{N} \omega_n A_n \frac{\cosh\left(\tilde{k}_n (z+d)\right)}{\sinh(\tilde{k}_n d)} \exp\left[i(\tilde{k}_n x - \omega_n t) \right] \right\} \tag{1.25}$$

$$w(x,z,t) = \mathrm{Im}\left\{ \sum_{n=-N}^{N} \omega_n A_n \frac{\sinh\left(\tilde{k}_n (z+d)\right)}{\sinh(\tilde{k}_n d)} \exp\left[i(\tilde{k}_n x - \omega_n t) \right] \right\} \tag{1.26}$$

These equations are only valid below the mean water level ($z \le 0$). Various methods of estimating fluid properties in the wave crests exist, and are summarized in [20]. Here, Wheeler stretching is used because it performs well for measured free surface profiles [20], and is therefore well suited for experimental/numerical model comparisons. Wheeler stretching estimates the fluid properties in the wave crests by introducing:

$$z_c = \frac{d(z+\eta)}{d+\eta} \tag{1.27}$$

which replaces z in equations (1.24) to (1.26) so that they become:

$$p_{dyn}(x,z,t) = \rho g \,\mathrm{Re}\left\{\sum_n A_n \frac{\cosh\left(\tilde{k}_n(z_c+d)\right)}{\cosh(\tilde{k}_n d)} \exp\left[i(\tilde{k}_n x - \omega_n t)\right]\right\} \tag{1.28}$$

$$u(x,z,t) = \mathrm{Re}\left\{\sum_n \omega_n A_n \frac{\cosh\left(\tilde{k}_n(z_c+d)\right)}{\sinh(\tilde{k}_n d)} \exp\left[i(\tilde{k}_n x - \omega_n t)\right]\right\} \tag{1.29}$$

$$w(x,z,t) = \mathrm{Im}\left\{\sum_n \omega_n A_n \frac{\sinh\left(\tilde{k}_n(z_c+d)\right)}{\sinh(\tilde{k}_n d)} \exp\left[i(\tilde{k}_n x - \omega_n t)\right]\right\} \tag{1.30}$$

Equations (1.28) to (1.30) are used only if values for pressure and fluid velocity are required in the wave crest, for example in section 3.3 and 3.4.1 where nonlinear expressions for the fluid loads on the OWSC are discussed. Otherwise Eq. (1.24) to (1.26) are used.

1.3.3 OWSC Dynamics

OWSCs are constrained to move only in the pitch degree of freedom by an immovable hinge at the base of the flap. Therefore, the total moment and the mass distribution (inertia) relative to the hinge axis (y-axis) of the OWSC is of interest; structural integrity is not considered in this thesis and the net force acting upon the hinge joint is not considered. The FSI problem is complex due to the interaction between the dynamic pressure fields created by the incident wave field and by the OWSC body motion. Fully nonlinear techniques such as CFD and SPH have been successful at solving the governing equations for such systems [7], [9]; they are necessary for analyzing extreme cases when wave heights are large as they are the methods that will capture drastic changes in the waterplane areas, changes in the geometry of the displaced volume, wake formation around sharp edges, and impact loads upon the structure. However, these techniques are not suitable for certain design problems such as power assessment and control system design [24] due to the computational expense of solving the fluid pressure and velocity fields.

When not simulating extreme wave conditions, e.g. when studying OWSC motion in the power production regime, a common approach is to employ a purely inviscid, irrotational approximation to the fluid, and then reintroduce viscous forces as a separate layer using approximate semi-empirical equations. In this case, the standard Airy wave equations apply in the far field, and the

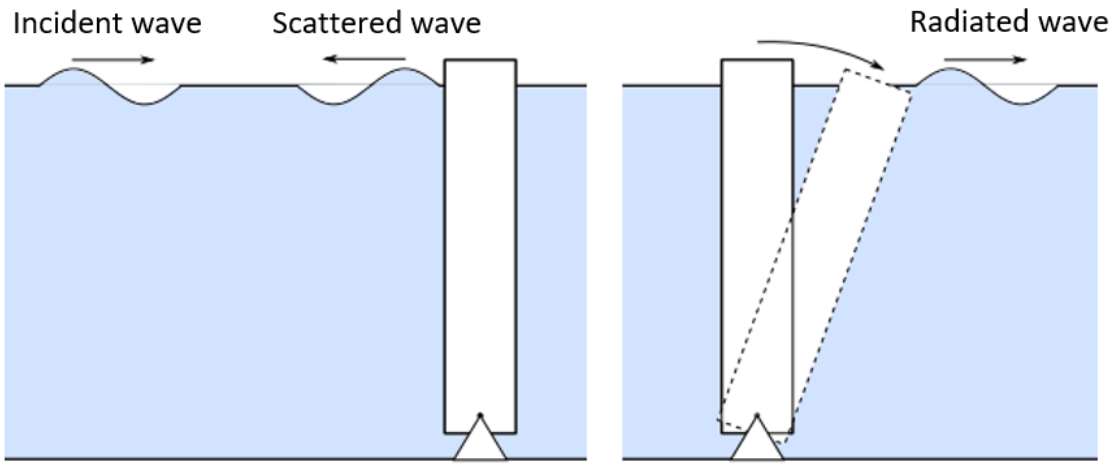

Figure 1-5: The wave diffraction and radiation problems. Wave diffraction consists of the combined wave fields from incident and scattered waves. Radiated waves are produced by body motion

perturbed flow around the OWSC can be determined by adding an impermeable condition at the OWSC surface to the original governing equations and boundary conditions that underpin Airy wave theory. The resulting modified fluid potential can be considered as the superposition of two contributions: diffraction and radiation potentials.

The wave diffraction problem satisfies the impermeability condition at the body surface when the OWSC is fixed upright in regular waves. As waves impinge upon the surface of the structure, a scattered wave is produced due to the impermeability of the structure. The combination of both incident and scattered waves is called the diffracted wave field.

The diffraction problem is supplemented by the radiation problem, which satisfies the impermeability condition when the OWSC oscillates at a constant frequency in still water. As the body oscillates, radiated waves are produced which alter the pressure fields around the body. The total potential is therefore obtained from the summation of incident, scattered and radiated wave potential functions:

$$\begin{aligned}\Phi_{total} &= \Phi_D + \Phi_R \\ &= \left(\Phi_0 + \Phi_S\right) + \Phi_R\end{aligned} \tag{1.31}$$

Note that Φ_0 is already known from Eq. (1.4).

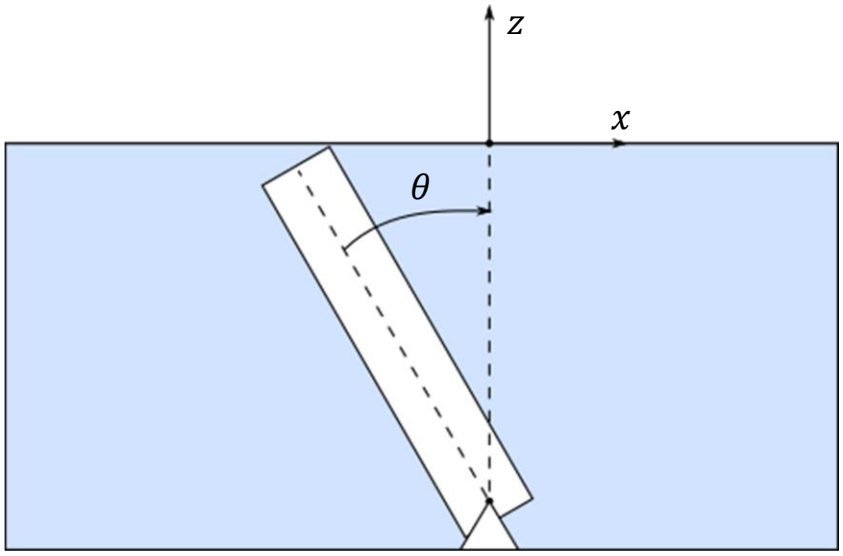

Figure 1-6: Coordinate system definition for the OWSC dynamics model. The global reference frame origin is located at the mean water level above the midpoint of the hinge axis

Given the total fluid velocity potential, the equation of motion for the OWSC can be expressed as:

$$I\ddot{\theta}(t) = M_{FK}(t) + M_S(t) + M_R(t) + M_b(t) + M_g(t) + M_d(t) + M_{ext}(t) \tag{1.32}$$

where θ is the OWSC pitch angle about the hinge axis parallel to the y-axis of the global reference frame, as shown in Figure 1-6. The moment arising from the undisturbed fluid potential Φ_0 is the Froude-Krylov moment and is commonly denoted as M_{FK} [17]. M_S and M_R are the moments arising from Φ_S and Φ_R, respectively. Viscous effects are reintroduced by adding a drag moment M_d to compensate for the inviscid flow assumptions required to derive the potential functions in Eq. (1.31) . The remaining moments are due to buoyancy M_b, gravity M_g and any externally applied moments M_{ext}.

Each moment on the right hand side of Eq. (1.32) is one instance of a layer of the FSI problem, and is calculated independently of the other layers under the assumption that the pressure field that

gives rise to each layer can indeed be superposed. A summary of the solutions for each layer is provided here:

Froude-Krylov, scattered wave and radiation moments

The moments M_{FK}, M_S and M_R are obtained by integrating the dynamic pressure fields corresponding to Φ_0, Φ_S and Φ_R over the wetted surface of the body:

$$M_{FK}(t) = \iint_S p_0(\vec{r} \times \vec{n})\vec{j}dS \tag{1.33}$$

$$M_S(t) = \iint_S p_S(\vec{r} \times \vec{n})\vec{j}dS \tag{1.34}$$

$$M_R(t) = \iint_S p_R(\vec{r} \times \vec{n})\vec{j}dS \tag{1.35}$$

where $p_0(x,z,t)$, $p_S(x,z,t)$ and $p_R(x,z,t)$ are obtained from the potential functions Φ_0, Φ_S and Φ_R using (1.21).

The solution for the pressure field p_0 assumes the body is hydrodynamically transparent [17] and therefore is independent of the body geometry. This pressure field is obtained from Eq. (1.24) and gives rise to the Froude-Krylov moment $M_{FK}(t)$ [18]. The other pressure fields however are dependent on body geometry, and their solutions are more complex.

A more common alternative to integrating the fluid pressure fields over the instantaneous wetted surface of the body is to assume small amplitude wave and body motions, allowing pressure to be integrated about the constant mean wetted surface of the body. The resulting solutions for the Froude-Krylov, radiation and scattering moments are linear, and are further discussed in Section 2.2.

Buoyancy and gravity moments

The buoyancy moment M_b is obtained by integrating the hydrostatic pressure field over the wetted surface of the body:

$$M_b(t) = \iint_S -\rho g z(\vec{r} \times \vec{n})\vec{j}dS \tag{1.36}$$

The buoyancy moment acts as a restoring moment bringing the OWSC upright. It is typically combined with the gravity moment, which counteracts buoyancy, to obtain a net restoring moment whose magnitude is dependent upon the pitch angle of the OWSC.

Viscous Drag

Viscous drag is a necessary force to consider when simulating WEC devices. If neglected, power production of an OWSC device can be significantly overestimated [25]. Models based upon potential flow assumptions incorporate viscous drag using a semi-empirical approximation such as Morison's equation [26], which was originally developed to calculate the force upon a fixed vertical cylinder (a piling) in a surging oscillatory flow, and is given by [17]:

$$dF = C_m \rho d \forall \dot{u} + C_d \frac{\rho}{2} dA u |u| \tag{1.37}$$

where C_d and C_m are empirical drag and inertia coefficients.

The first term in Eq. (1.37) consists of the inertial forces (Froude-Krylov and scattering), and the second term is the viscous drag force (both calculated only in the surge direction). The empirical coefficients C_d and C_m are dependent upon both Reynolds number *Re* and Keulegan-Carpenter *KC*. Estimating the drag coefficient C_d is important when predicting the power production of an OWSC, and can lead to $\pm 30\%$ error in energy absorption if incorrectly set [5]. A variety of methods can be employed for obtaining values for the empirical coefficients from physical model tests, and are summarized in [27]. Numerical results from CFD and SPH can also be used in place of physical tests [28].

Equation (1.37) provides the force on discrete elements of a stationary body in accelerating flow. For a moving body, the inertial forces on body elements near the free surface are different as the body produces radiated waves which complicate the calculation of the resulting moment. For OWSCs, common practice is therefore to only use the drag portion of Eq. (1.37), and the total moment due to the inertial forces over the entire body is instead solved under potential flow assumptions, using boundary element methods such as the commercial software WAMIT. Caska and Finnigan [29] note that the validity of this approach should be limited to conditions for which

$KC < 10$, where inertial forces dominate over viscous forces. This ensures that inertial forces solved using potential flow theory are not modified by viscous effects [29].

There are various methods in which Morison's equation can be applied to OWSC geometries:

1. A drag force is applied at a single reference point [30].
2. The WEC cross-section is divided into strips, and drag forces calculated for each strip are integrated over the WEC surface [11], [29].
3. The WEC surface is divided into panels, and drag forces calculated for each panel are integrated over the WEC surface [31].

In this thesis, only the strip method (2) and panel method (3) are considered, and are further discussed in Section 3.4.

1.4 Contributions

1) Develop candidate numerical OWSC models

The primary contribution of this thesis is establishing a recommended nonlinear time-domain model for OWSC power production assessments. Three candidate numerical models are developed based upon existing modelling techniques in literature. The first model is the same used in [11], where it was demonstrated that a nonlinear buoyancy moment calculation can lead to better estimates of the optimal PTO properties to maximize power capture. This model is then used as a foundation upon which the other two candidate models are developed that append:

1. The panel method for computing the drag moment used in [31]
2. The nonlinear Froude-Krylov moment calculation used in [12]–[14]

Experimental data collected using a scale model OWSC is used as a reference to observe divergence of the candidate model predictions from the true dynamics of the OWSC device. Deviations of the numerical model predictions from experimental observations are expected to arise as wave height increases, since the numerical models are fundamentally based upon small amplitude assumptions. However, the amount of deviation is expected to vary for each candidate

model due to the different modelling approaches. A complication with this analysis is the limited stroke length of the wavemaker piston, which prevents large amplitude waves from being generated. In case the candidate models all provide similar predictions for the range of wave conditions which can be experimentally produced, then the computational requirements of each model will also be considered when selecting a recommended model.

2) Establish methodology for experimental/numerical model comparisons

The second contribution is the development of a methodology for performing experimental/numerical model comparisons using UVic's small-scale wave tank. This methodology treats the experimental wave profile as a partially standing wave field, where the incident and reflected waves are identified using a modified reflection algorithm that accounts for the presence of the OWSC model in the fluid domain using potential flow solutions for the radiated and scattered waves produced by the OWSC. The algorithm allows the influence of reflected waves upon the OWSC model dynamics to be identified while the OWSC model is in the tank.

When comparing numerical and experimental results, the input wave system for the numerical simulations are partially standing wave systems using the results from the modified reflection algorithm. So rather than correcting the experimental data to remove the influence of wave reflections, numerical models are simulated using the exact wave conditions that occurred during each experimental trial, including the reflected wave segments. Note that this means that each simulation is performed for an irregular wave profile, even if the intended wave profile is regular. This approach may be valuable for other researchers experiencing similar issues with wave reflections.

3) Estimate annual power production at a potential OWSC deployment site

The final contribution is using the candidate numerical OWSC models to estimate the APP of a single OWSC device at a promising site on the west coast of BC. The wave climate at the site is estimated using a SWAN model developed by Robertson *et. al.* [19]. An ideal passive power take-off system (PTO) is included in the candidate OWSC models to represent the power generation process. Prior to estimating annual power production (APP), optimal PTO coefficients for the numerical OWSC models are obtained for all incident wave heights and periods at the deployment site using a least squares maximization procedure. Future studies can build upon this assessment

by incorporating more advanced PTO systems and control strategies into the recommended model to maximize power generation.

The resulting APP estimates from the candidate models, combined with the experimental/numerical model comparison results from Contribution 1, are used to obtain a final estimate of the power production of the OWSC device and to select a recommended model from the three candidate models.

1.5 Thesis Overview

This thesis consists of seven chapters. Chapters 2 and 3 cover the development of candidate nonlinear numerical models of the OWSC. Chapter 2 presents the linear theory upon which each model is founded, and provides linear hydrodynamic coefficients for the inviscid fluid loads upon the structure. Chapter 3 then augments these inviscid loads with nonlinear modelling techniques from the existing literature.

Chapter 4 presents a potential deployment site for the OWSC, and identifies suitable ranges of wave parameters that represent the wave climate at the deployment location. Initial experiments focussed at recreating these conditions in the small-scale wave tank are presented which demonstrate the significance of the reflected waves within the free surface profiles generated in the tank. Lastly, the modified wave reflection algorithm used to separate the wave system into incident and reflected components, with the OWSC model in the tank, is presented.

Chapter 5 provides experimental data collected with the OWSC model in the tank, and compares these results with numerical predictions from each of the candidate numerical models. Freed decay tests are used to identify experimental drag coefficient for the models. Tests conducted with the OWSC fixed vertically (i.e. constrained) are then used to evaluate the candidate numerical models of the wave excitation moment. The fixed OWSC tests also demonstrate the utility of the modified wave reflection algorithm. For the final round of tests, the OWSC model is left free to oscillate (i.e. unconstrained), and the resulting pitch motions in regular and irregular waves are observed. These results are used to evaluate the accuracy of the fully assembled candidate numerical models when simulating the full FSI problem.

Chapter 6 uses the candidate numerical models to estimate the APP of the OWSC at full scale and at the deployment site presented in Chapter 4. A linear passive damping PTO is used to represent the power generation process, and optimal PTO damping coefficients are obtained for each incident wave height and period. APP estimates are obtained for each candidate model to observe whether any significant differences in power production result from the different modelling approaches. Finally, this chapter selects a recommended modelling approach based on the experimental/numerical model comparisons, the APP estimates from each candidate model, and the computational requirements of each model.

Chapter 7 revisits the major findings of the research, discusses how the three contributions outlined in Section 1.4 can serve future research and gives recommendations for the direction of such future work.

Chapter 2: Baseline OWSC Model

This chapter introduces the geometry of the OWSC model and identifies the parameters required to develop a fully linear time-domain model based upon potential flow theory. This baseline linear model serves as a platform upon which nonlinear extensions can be applied to develop the three candidate numerical models, as discussed in Chapter 3. The geometry of the Resolute Marine Energy (RME)[1] OWSC was adopted for the study. It features curved edges to reduce viscous drag on the sides of the flap.

A 1:40 scale model of the original RME OWSC design, shown in Figure 2-1, is used for tank testing. This choice of scale is discussed in Chapter 4. The full-scale device is designed to operate in 8m of water, which at model scale corresponds to a tank depth of 20cm. The height of the model (Figure 2-1) is 22cm, so when oriented vertically the OWSC is surface piercing. The experimental model is constructed from both bonded Plexiglas and modelling foam. The foam is coated with Plastidip to seal it from water to prevent the inertial properties of the model from changing during tests. The flap pivots about a stainless-steel axis held within two plastic ball bearings mounted to a base structure fixed at the bottom of the tank.

Numerical modelling is also carried out at the 1:40 experimental model scale. In this chapter, expressions for the radiation and wave excitation moments upon the OWSC are quantified using potential flow theory. The radiation moment, along with the scattering component of the excitation

[1] http://www.resolutemarine.com/ [Last accessed on 09/18/2017]

moment, are used in all three candidate models and are fully linear hydrodynamic expressions in terms of the body kinematics. A linear expression is also obtained for the Froude-Krylov moment, however for some of the candidate numerical models it will be overridden by a nonlinear algorithm to be discussed in Chapter 3.

In anticipation of the comparison with experimental results, the amplitudes of the radiation and wave excitation moments are computed with and without the influence of tank walls to observe the significance of wall effects upon the dynamics of the scale model OWSC. In previous works, wall effects have been shown to change the resonant characteristics of WEC models due to transverse sloshing waves [32], and must therefore be accounted for to properly compare numerical and experimental results.

2.1 Mechanical Properties

The physical properties of the scale model OWSC were determined using a combination of direct measurements and numerical estimates from a SolidWorks model. The total mass, along with the mass of each subcomponent, are individually measured using a scale, then the center of mass is determined using the SolidWorks model along with the measured masses. This result is validated by measuring the moment required to hold the flap horizontal when hinged at the base. The center of buoyancy is also obtained from the SolidWorks model by modelling the displaced volume of fluid by the geometry of the flap, then calculating the center of gravity of the resulting model.

Inertia, along with coulomb friction in the bearings, is measured by hanging the flap vertically like a pendulum, and measuring the decay rate of the model. The following numerical pendulum model is fitted to the measured pitch decay to obtain inertia I and friction moment M_f.

$$I\ddot{\theta} = -mgr_g \sin\theta - M_f \operatorname{sign}\{\dot{\theta}\} \tag{2.1}$$

The resulting inertia and friction estimates are shown in Table 2-1, along with the other physical properties. Bearing friction is substantially less than the magnitude of the other moments on the system, and is therefore neglected.

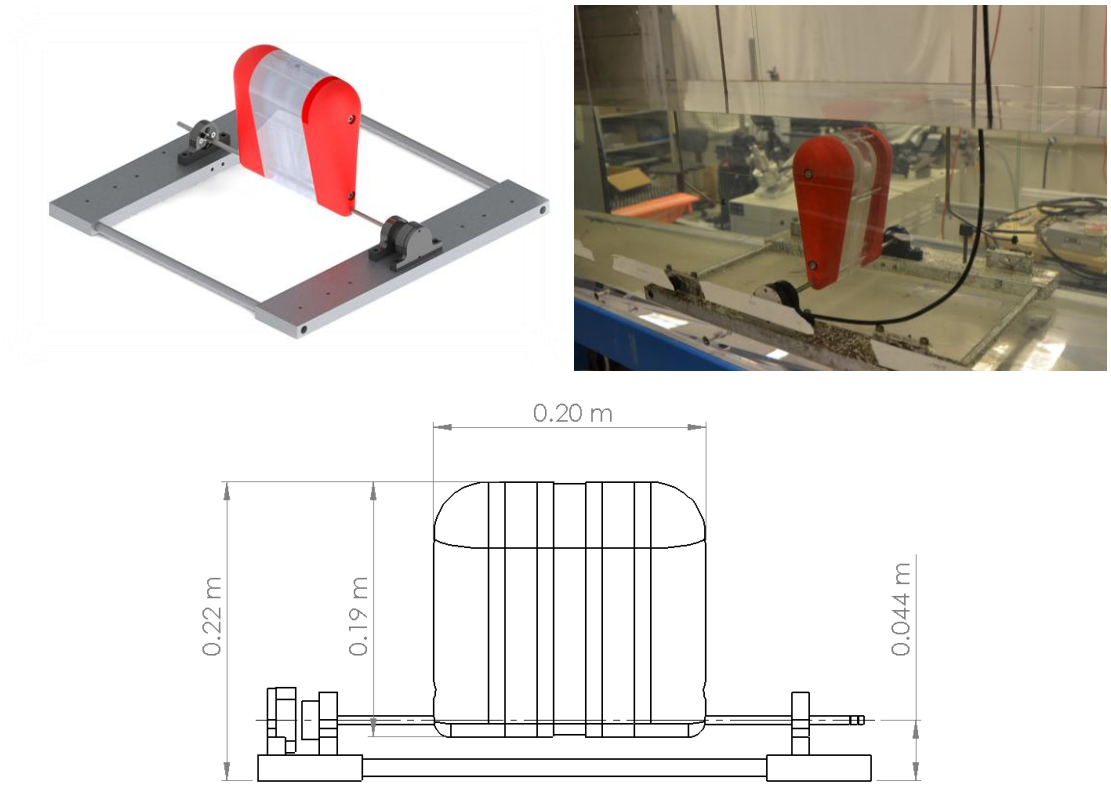

Figure 2-1: The scale model OWSC and base structure. Top left figure is a rendering of the SolidWorks model, and the top right image is of the physical model deployed in the tank. The bottom figure shows key dimensions for the model

Table 2-1: Physical properties of the scale model OWSC

Property	Symbol	Value	Units
Mass	m	1.15	kg
Inertia about hinge axis	I	0.0125	$kg \cdot m^2$
Center of gravity position	r_g	0.0875	m
Center of buoyancy position	r_b	0.0881	m
Bearing friction	M_f	1.75E-3	$N \cdot m$

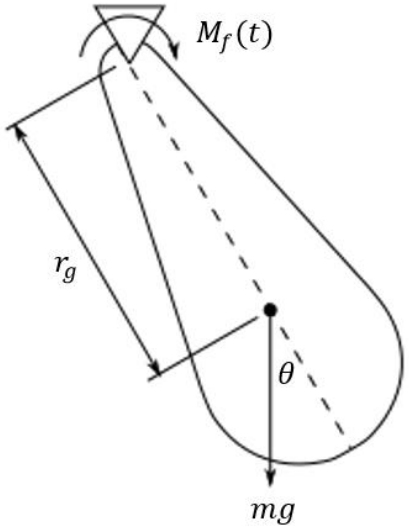

Figure 2-2: Free body diagram for the pendulum tests used to obtain inertia and bearing friction.

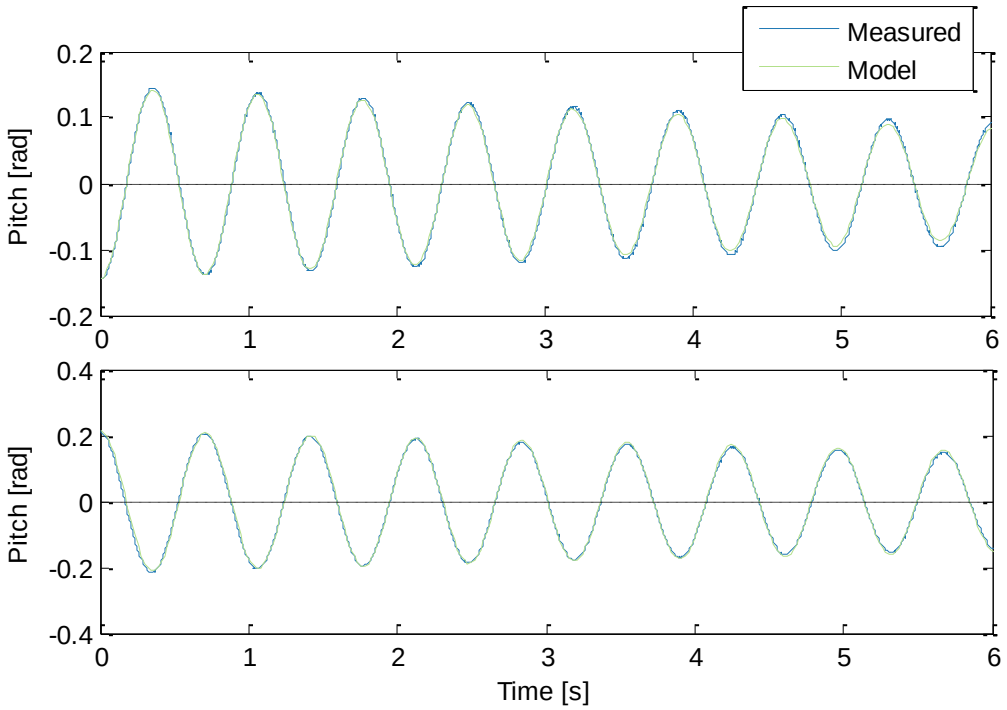

Figure 2-3: Sample comparisons of numerical model and measured pendulum

2.2 Linear OWSC Dynamics Model

Linear models rely upon small body motion and wave amplitude assumptions. Under these assumptions, in regular wave conditions, the fluid velocity potential functions in (1.31) can be solved about the mean wetted surface of the body using boundary element methods (BEM). The resulting solutions are dependent only upon the regular wave frequency and are used to derive the normalized complex amplitudes of the Froude-Krylov moment X_{FK}, scattered wave moment X_S and radiation moment X_R. Such models have been applied to OWSCs in previous works such as [15], [32], [33], and shown by Van't Hoff to agree with experimental results obtained in small wave amplitude conditions [34].

The time series of the hydrodynamic moments in Eq. (1.32) in regular wave conditions of amplitude A and angular frequency ω are given by:

$$M_{FK}(t) = \mathrm{Re}\left\{ X_{FK}(\omega) A e^{-i\omega t} \right\} \tag{2.2}$$

$$M_S(t) = \mathrm{Re}\left\{ X_S(\omega) A e^{-i\omega t} \right\} \tag{2.3}$$

$$\begin{aligned} M_R(t) &= \mathrm{Re}\left\{ X_R(\omega) \hat{\theta} e^{i\omega t} \right\} \\ &= \mathrm{Re}\left\{ \left[\omega^2 A_c(\omega) + i\omega B_c(\omega) \right] \hat{\theta} e^{-i\omega t} \right\} \end{aligned} \tag{2.4}$$

where $\hat{\theta}$ is the complex amplitude of pitch motion, $B_c(\omega)$ is the radiation damping coefficient and $A_c(\omega)$ is termed added inertia since it causes an apparent increase in the inertia of the body.

Because of the small amplitude assumptions, the buoyancy moment M_b can be combined with the gravity moment M_g to form a linear stiffness term:

$$M_b + M_g = C \sin\theta \approx C\theta \tag{2.5}$$

where the stiffness coefficient C arises from the linearization of gravity and buoyancy loads about the mean OWSC position and is given by [11]:

$$C = \rho g \forall r_b - mgr_g \tag{2.6}$$

By

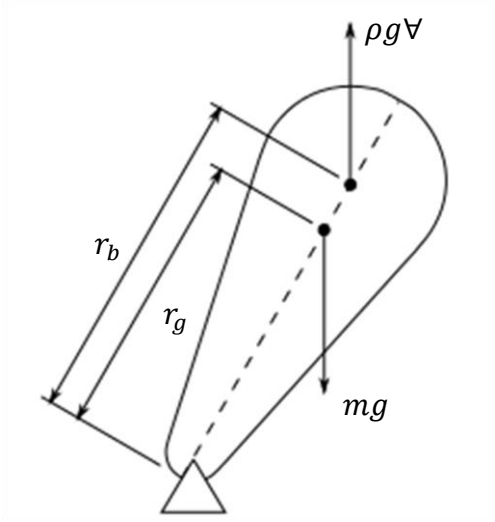

Figure 2-4: Free body diagram for deriving the stiffness coefficient.

substituting equations (2.2) to (2.5) into (1.32), assuming the drag moment M_d is negligible and there are no external loads, the equation of motion of the OWSC in regular waves becomes:

$$\left[-\omega^2\left(I + A_c(\omega)\right) - i\omega B_c(\omega) + C\right]\hat{\theta} = \left(X_{FK}(\omega) + X_S(\omega)\right)A \tag{2.7}$$

A more general representation of the equation of motion, one that can be applied to irregular wave systems and transient motions, is Cummin's equation [35], which for OWSCs is:

$$(I + A_\infty)\ddot{\theta} + \int_0^t k(t-\tau)\dot{\theta}(\tau)d\tau + C\theta = M_e(t) \tag{2.8}$$

where $A_\infty = \lim_{\omega\to\infty} A(\omega)$, and $k(t)$ is the radiation impulse response function (IRF). The time and frequency domain definitions of the radiation IRF are, respectively [36]:

$$k(t) = \frac{2}{\pi}\int_0^\infty B_c(\omega)\cos(\omega t)d\omega \tag{2.9}$$

$$k(\omega) = B_c(\omega) - i\omega(A_c(\omega) - A_\infty) \tag{2.10}$$

M_e is the total wave excitation moment and consists of both Froude-Krylov and scattered wave moments. It is given by

$$M_e(t) = M_{FK}(t) + M_S(t) = \int_{-\infty}^{\infty} k_e(\tau)\eta(t-\tau)d\tau \tag{2.11}$$

where $k_e(t)$ is the inverse Fourier transform of the sum of the complex amplitudes of the Froude-Krylov and scattered wave moments:

$$k_e(t) = \frac{1}{2\pi}\int_0^{\infty}\left[X_{FK}(\omega) + X_S(\omega)\right]e^{i\omega t}d\omega \tag{2.12}$$

Further details on the derivation of the linear equation of motion can be found in [36].

2.3 Hydrodynamic Coefficients for Radiation and Wave Excitation

The hydrodynamic coefficients for added inertia A_c and radiation damping B_c, along with the complex amplitudes for the linearized wave excitation moments X_{FK} and X_S, are solved using WAMIT. Version 7.2 is utilized as it introduces the option to place channel walls around the body, allowing blockage and resonance effects due to the tank walls to be accounted for when solving for the coefficients. A downside of the channel feature is that the added inertia at infinite frequency (A_∞) cannot be explicitly solved, therefore it must be approximated using the infinite added inertia computed without channel effects. WAMIT allows the magnitude of channel reflections to be

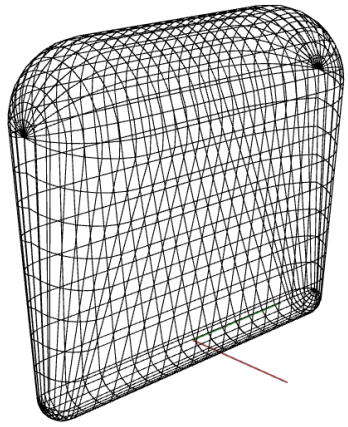

Figure 2-5: Sample mesh for obtaining the hydrodynamic coefficients of the OWSC

controlled by a reflection coefficient to account for any viscous or other nonlinear losses in the reflection process. This work assumes these losses are negligible and the tank wall reflection coefficient is set to 100%.

The linear hydrodynamic coefficients are solved using different meshes with resolutions ranging from 1280 to 16128 panels to ensure convergence of the BEM solutions. The converged solutions for the hydrodynamic coefficients with and without channel effects are presented in Figure 2-6 and Figure 2-7. Two key observations from the results can be made:

1. The total wave excitation moment within the range of wave frequencies is dominated by the scattered wave component of the diffraction problem, as opposed to the Froude-Krylov moment. This indicates that nonlinear Froude-Krylov may have little influence on numerical model results, while nonlinear extensions to the scattered wave moment may be worth investigating further

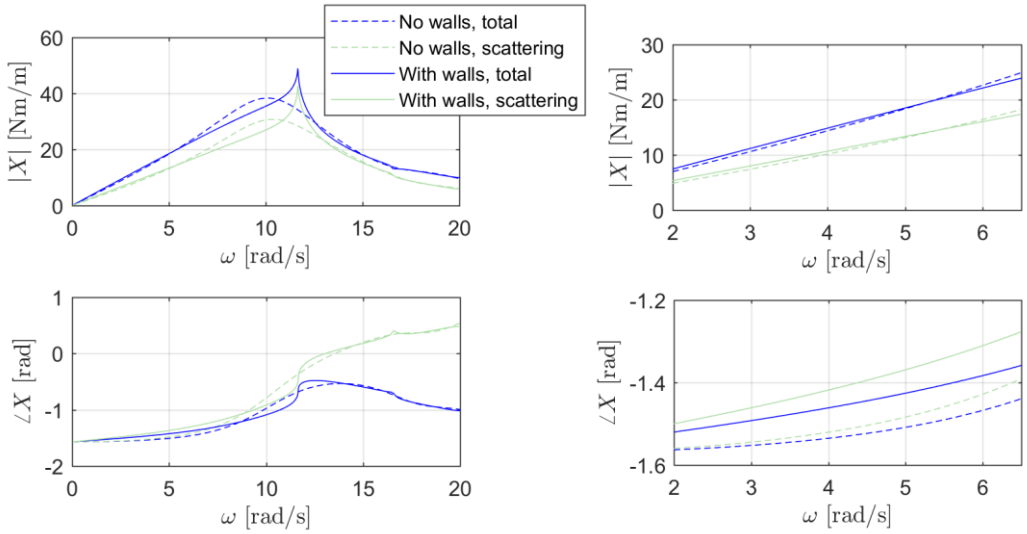

Figure 2-6: WAMIT results for the linear wave excitation moment. The complex moment amplitudes are plotted in terms of modulus (top row) and argument (bottom row). The plots compare results for the total and scattering component of the wave excitation, with and without tank walls. The figures in the right column are closer views of the figures in the left column over the range of ocean wave frequencies

2. Wall effects do have a significant effect on the hydrodynamic coefficients. Resonance can be observed at approximately 12 rad/s. The influence of wall effects upon the resonant frequency of the OWSC is investigated in Section 2.5

2.4 Time Domain Simulation of the Radiation Moment

In Section 2.2, it was shown that the radiation moment can be evaluated in the time domain by convolving the OWSC pitch velocity with a radiation IRF defined in Eq. (2.9). With the WAMIT results for added inertia and radiation damping coefficients, the resulting radiation IRF k for the scale

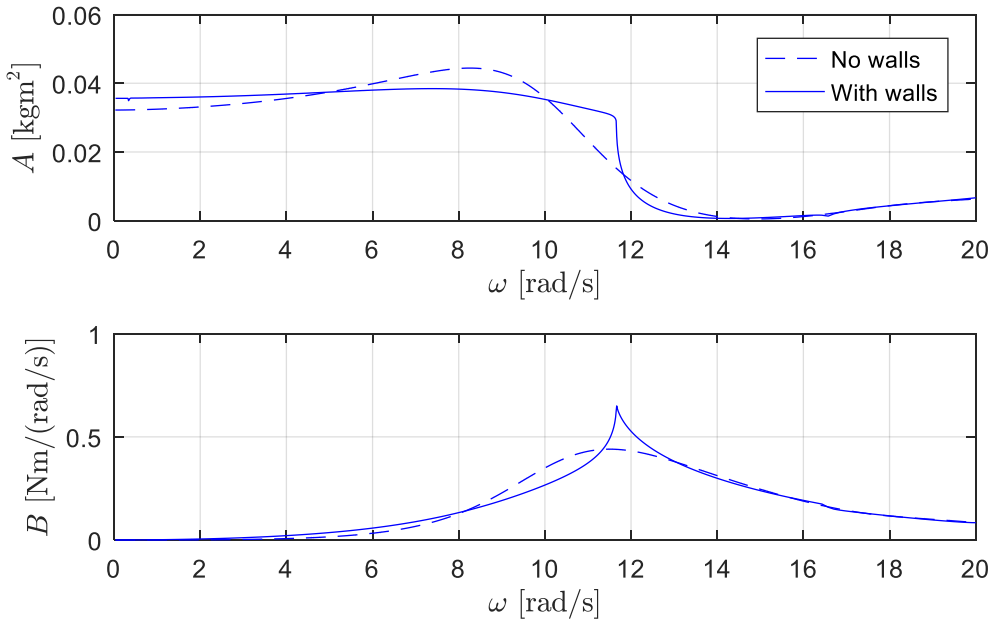

Figure 2-7: WAMIT results for added inertia and radiation damping, with and without tank walls.

model is given in Figure 2-8.

Simulating the OWSC in the time domain requires careful consideration of the numerical method of evaluating the convolution between the radiation kernel and pitch velocity. There are various methods of evaluating this moment. Ultimately, whichever method is used, the frequency response of the numerical method should closely approximate the frequency response of the IRF

given in Eq. (2.10). One approach is to perform a discrete time convolution between the radiation kernel and pitch velocity. This is equivalent to filtering the pitch velocity data with a discrete filter whose transfer function is:

$$K(z) = \sum_{n=0}^{N} k(nt_s) z^{-n} \tag{2.13}$$

The filter order N and time interval t_s are selected so that the kernel function at $k(nt_s)$ has effectively decayed to zero. The filter order needs to be carefully considered; too high will lead to high computational expense, while too low while lead to error between the filter frequency response and Eq. (2.10), as shown in Figure 2-9.

An alternative approach is to implement frequency domain identification techniques, for example using the MSS FDI Toolbox developed by Perez and Fossen [37]. For this work, a similar approach is implemented using the MATLAB function *ssest* to approximate the radiation IRF with a continuous-time state-space model whose frequency response matches the radiation frequency response computed by WAMIT. A 15th order state-space model approximates well the radiation frequency response over the range of incident wave frequencies, as shown in Figure 2-9.

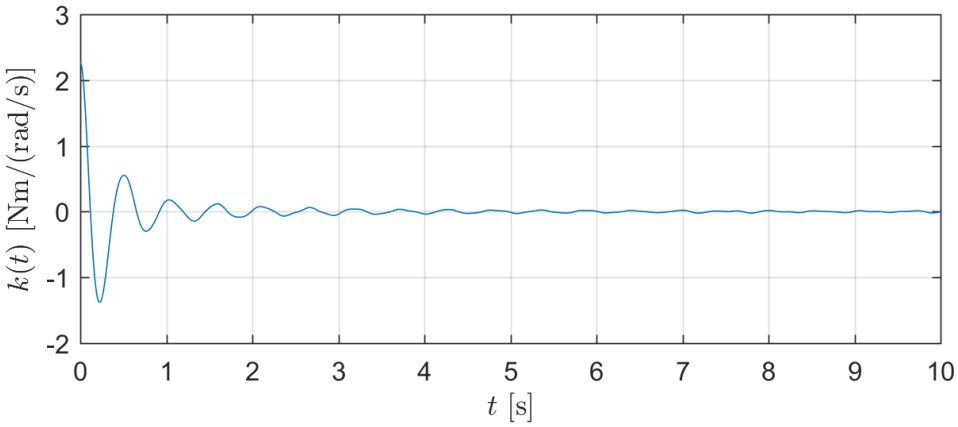

Figure 2-8: Radiation kernel function

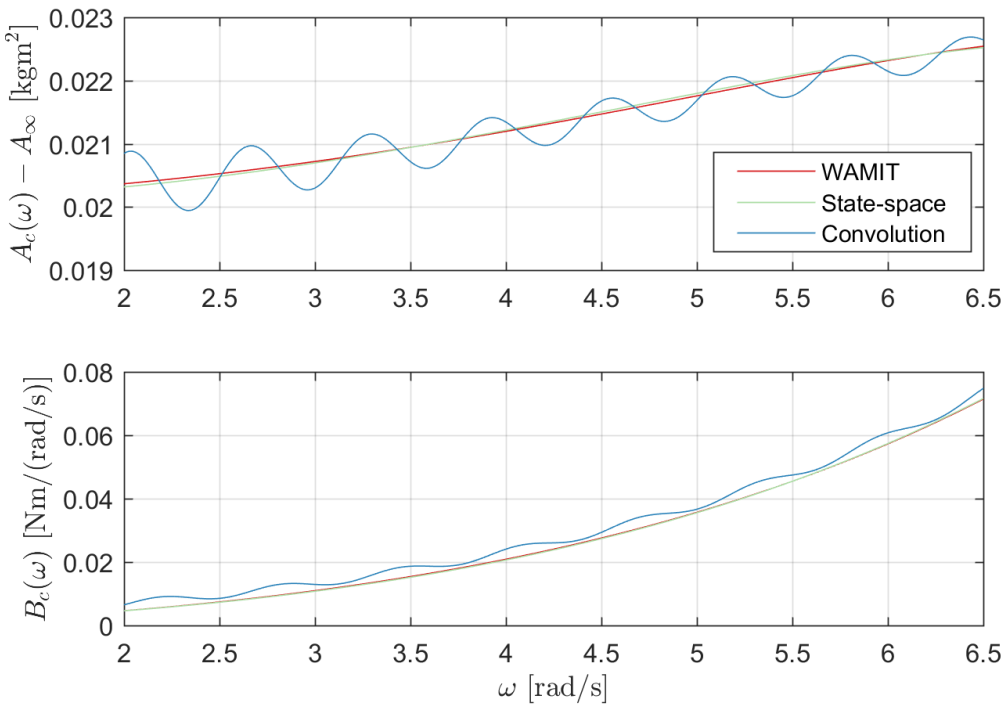

Figure 2-9: Frequency responses of the two methods to compute the radiation moment, compared with the original WAMIT data. The order of the discrete filter for the convolution method is 5000, while the order of the state-space model is 15.

2.5 Influence of Tank Walls upon OWSC Dynamics

At this stage, the response of the OWSC model to small amplitude regular waves can be estimated as a function of frequency using Eq. (2.7). The linear hydrodynamic coefficients are used to estimate the pitch response of the flap to a wave of unit amplitude, i.e. the pitch response amplitude operator (RAO), across the range of wave frequencies in the environment:

$$\hat{\theta}(\omega) = \frac{X_{FK}(\omega) + X_S(\omega)}{-\omega^2 (I + A_c(\omega)) - i\omega B_c(\omega) + C} A \tag{2.14}$$

where the stiffness coefficient C is obtained from Eq. (2.6). Equation (2.14) is evaluated twice, first using coefficients without tank walls and then using coefficients with tank walls. The resulting

frequency response curves are compared to observe the influence of wall effects upon the OWSC dynamics.

Figure 2-10 shows the resulting RAOs for $A = 1mm$ using the physical properties in Table 2-1 and the WAMIT results from Figure 2-6 and Figure 2-7. The figure shows that tank walls cause the resonant peak to shift to lower frequencies and therefore has a notable influence on the motion of the body near this frequency.

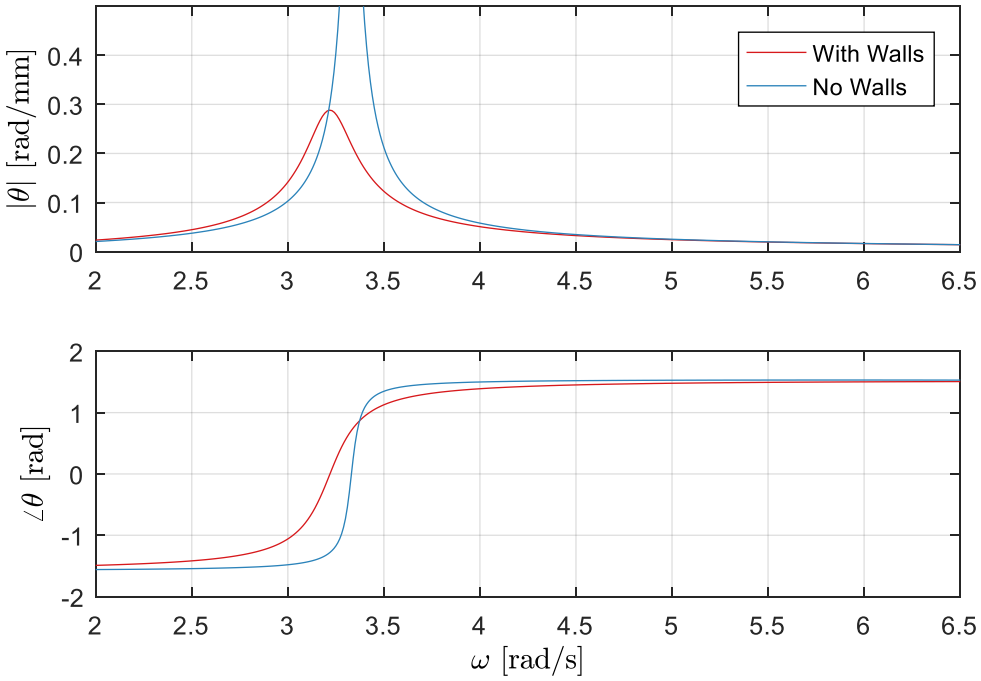

Figure 2-10: Influence of channel walls on the pitch response of the OWSC model. The top figure plots the modulus of the response amplitude, and the bottom figure plots the argument.

2.6 Chapter Summary

This chapter identified values for the physical properties of the OWSC, and calculated coefficients for the linear hydrodynamic model of the device, including added inertia, radiation damping and the complex amplitudes of the wave excitation moments under linear assumptions. The influence of wall effects was also considered, and plotting the response of the OWSC to regular waves showed that tank walls change the resonant frequency of the device and will therefore have a considerable influence of the motion of the flap near this frequency. In addition,

two methods of evaluating the radiation moment in time domain models were compared. The convolution method does not correctly reproduce the amplitude of the radiation moment predicted by WAMIT when subjected to regular waves, therefore a state-space model optimized to match the complex moment amplitudes from WAMIT will be used.

Wall effects have a significant effect on the OWSC dynamics, effectively shifting the peak motion frequency of the device to lower wave frequencies. These effects are therefore important to consider when comparing numerical and experimental results, for example when conducting experiments to derive a viscous drag coefficient; neglecting to account for wall effects could lead to incorrect estimates for the drag coefficient. Therefore, hydrodynamic coefficients with wall effects will be used in Chapter 5 when comparing experimental and numerical results, however coefficients without wall effects will be used in Chapter 6 for estimating annual power production at a potential deployment site in the ocean.

Chapter 3: Nonlinear Extensions to the OWSC Dynamics Model

In Chapter 1, the overall fluid moment on the OWSC is separated into 5 layers: buoyancy, Froude-Krylov, scattering, radiation and viscous drag. Chapter 2 demonstrates the calculation for each layer assuming wave and body motion amplitudes are small. However, with WECs these assumptions do not always apply, as WECs are designed to excite large amplitude motions within the range of wave frequencies. This chapter discusses the incorporation of nonlinear extensions into the baseline OWSC model developed in Chapter 2 to compensate for these small amplitude assumptions. These extensions are either additions to the baseline model, such as viscous drag which was neglected in Chapter 2, or are revisions of existing moments within the baseline model such as the buoyancy and Froude-Krylov moments. The candidate models are implemented in MATLAB/Simulink.

Section 3.1 reviews the nonlinear extensions which have been applied to OWSCs and other WEC devices in literature. Various combinations of these techniques are then combined to develop three candidate nonlinear time domain models. The amplitude responses predicted by each model in regular waves are then compared for various wave heights to observe differences between model predictions as wave height increases. The computational requirements of each model are also considered; if two modelling techniques provide equivalent predictions then computational efficiency is considered as a secondary objective.

3.1 Candidate OWSC Model Descriptions

Currently, many of the numerical models used for estimating power production and for designing control systems incorporate nonlinear extensions [11], [38]. While the baseline linear model given by Eq. (2.8) is convenient for these studies, it often does not sufficiently describe the motion of the OWSC, especially when the WEC is operating near resonance. If a control system is designed based on this model, it can lead to significantly lower power generation [38]. Incorporating nonlinear effects to improve the fidelity of time domain models is a key step towards designing effective control systems.

The nonlinear extensions considered here are classified based on whether they represent an inviscid or viscous phenomenon. Inviscid moments are considered first, as the equation of motion of the OWSC given in Eq. (2.8) must be redefined before nonlinear extensions to these moments can be applied. The viscous drag moment and the many ways it can be evaluated are then discussed.

Nonlinear extensions to the buoyancy and Froude-Krylov loads

One of the first nonlinear extensions implemented for OWSCs is to the buoyancy moment. In Chapter 2, both buoyancy and gravity moments were linearized about the upright position of the OWSC, resulting in a linear stiffness term. This approximation creates error because:

1. The OWSC can achieve large pitch amplitudes, therefore the small angle approximation $\sin\theta = \theta$ used in Eq. (2.5) becomes invalid
2. The buoyancy force changes in magnitude as the OWSC transitions from surface-piercing to fully submerged

One solution is to vary the stiffness coefficient with pitch angle, as in [30]. In this work, the stiffness coefficient function $C(\theta)$ is obtained prior to simulation by numerically integrating hydrostatic pressure beneath the still waterline at various pitch angles. The time domain model in Eq. (2.8) then becomes:

$$(I + A_\infty)\ddot{\theta} + \int_0^t k(t-\tau)\dot{\theta}(\tau)d\tau + C(\theta)\theta = M_e(t) + M_d(t) \tag{3.1}$$

Section 3.2 further discusses this method and presents the solution for $C(\theta)$ for the OWSC geometry considered in this thesis.

An alternative approach implemented in the works of [13], [14], [39] is to numerically integrate both hydrostatic and hydrodynamic fluid pressures beneath undisturbed waves over the instantaneous wetted surface of the body. In addition to revising the Froude-Krylov moment, it improves upon the stiffness coefficient function by accounting for wave crests and troughs, rather than integrating below the mean waterline. With this method, the equation of motion in Eq. (2.8) is modified to become

$$\begin{aligned}&(I+A_\infty)\ddot{\theta}+\int_0^t k(t-\tau)\dot{\theta}(\tau)d\tau \\ &=\left(M_b(t)+M_{FK}(t)\right)+M_S(t)+mgr_g\sin(\theta)+M_d(t)\end{aligned} \tag{3.2}$$

M_b+M_{FK} is evaluated by integrating the total undisturbed fluid pressure over the wetted surface of the body:

$$\left(M_b(t)+M_{FK}(t)\right)=\iint_S (p_{dyn}-\rho gz)(\vec{r}\times\vec{n})\,\vec{j}\,dS \tag{3.3}$$

where $-\rho gz$ is the hydrostatic pressure and p_{dyn} is the dynamic pressure due to the undisturbed incident wave, given in Eq. (1.28). The numerical integration to evaluate Eq. (3.3) is further discussed in Section 3.3.

The scattered wave moment M_S is computed using the same approach as the baseline model in Chapter 2. A new kernel function k_S is introduced; unlike k_e from Eq. (2.12), it is calculated using only the complex amplitudes of the scattered wave moments X_S obtained from WAMIT in Chapter 2:

$$k_S(t)=\frac{1}{2\pi}\int_0^\infty X_S(\omega)e^{-i\omega t}d\omega \tag{3.4}$$

The scattered wave moment is then calculated using:

$$M_S(t)=\int_{-\infty}^{\infty} k_S(\tau)\eta(t-\tau)d\tau \tag{3.5}$$

Giorgi *et. al.* [14] note that the buoyancy and Froude-Krylov moments are not the dominant moments acting upon the flap, and the relative importance of these moments is dependent upon the incident wave parameters. Therefore, in some wave conditions, implementing nonlinear extensions to these moments may have little influence on the OWSC dynamics. Nonetheless these extensions are considered here because unlike in [14], the experimental OWSC model is operating under uncontrolled conditions and may achieve larger motion amplitudes in certain conditions. A model containing nonlinear Froude-Krylov may therefore provide an extended range of wave heights for which it provides good predictions of the OWSC dynamics.

Numerical methods to evaluate viscous drag

A common method for calculating the drag moment on OWSC geometries is the strip method [11], [29]. With this approach, the total viscous drag moment is evaluated by integrating Morison's equation from the bottom to the top of the flap:

$$M_d(t) = \int_{r_1}^{r_2} \frac{1}{2} C_d \rho D (u_n - r\dot{\theta}) \,|\, u_n - r\dot{\theta} \,| r dr \tag{3.6}$$

where D is the flap width, r_1 and r_2 are the distances of the bottom and top edges of the OWSC from the hinge axis, and u_n is the fluid velocity normal to the OWSC cross-section.

A more general approach for computing the drag moment, one that can be applied to non-slender offshore structures, is the panel method implemented in [31] with the commercial software ProteusDS[2], where the body surface is discretized using a mesh and the drag force is computed on each panel. The drag force on each panel is then computed using the relative velocity of the fluid and the projected area of the panel onto each of the translational degrees of freedom. For example, the x-component of the drag force is computed using the following relation [31]:

[2] https://dsa-ltd.ca/proteusds/overview/ [Last accessed on 08/26/2017]

$$f_{i,x} = \frac{1}{2}\rho A_{i,\hat{x}} C_d (u - u_b)|u - u_b| \tag{3.7}$$

where $A_{i,\hat{x}}$ is the area of the panel projected onto the y-z plane of the global reference frame, u is the fluid velocity in the *x* direction and u_b is the body velocity in the *x* direction.

The numerical integration procedures for each approach are discussed in Section 3.4. Differences between the strip and the panel methods may arise due to the differences in force integration. The strip method uses the undisturbed flow velocity along the centerline of the body, while the panel method uses the flow velocity on the body surface. Therefore, in a situation where the flow varies significantly across the width of the body, differences between these methods may arise. Another difference between the two methods is the difference in the drag force direction on the discrete elements. With the strip method, the direction of the drag force on each strip is normal to the cross-section of the OWSC. However, with the panel method, the drag force on each panel is separated into 3 components in the x-y-z directions of the global reference frame. Due to these differences, separate drag coefficients may be required for the two methods of computing drag. These drag coefficients are determined experimentally in Section 5.1.

Candidate numerical models

In the previous sections, two methods for extending the buoyant and Froude-Krylov moments were presented:

1. Stiffness coefficient function
2. Surface integration of fluid pressure

In addition, two methods for approximating the drag moment were described:

1. Strip method
2. Panel method

This section presents three candidate models based on different combinations of these methods. Model 1 uses the stiffness coefficient function for computing buoyancy and the strip method for computing drag; of the three candidate models, it requires the fewest computations and is also

similar to other OWSC numerical models in literature [11]. Model 3 uses the surface integration approach to evaluate the buoyant and Froude-Krylov moments, along with the panel approach for viscous drag. In contrast to Model 1, it is the most computationally expensive as it requires calculating the buoyancy, Froude-Krylov and drag forces on each panel of a surface mesh of the OWSC body. Model 2 is intended as an intermediary model between Models 1 and 3, so that the influence of switching from the strip to panel method for computing drag on OWSC dynamics can be observed separately from the influence of the surface integration approach for evaluating the buoyancy and Froude-Krylov moments.

It is unlikely that Model 2 will be selected as the recommended model. It is more computationally expensive than Model 1 (due to the panel operations for computing viscous drag) and yet it does not gain the advantags of performing the surface integration of fluid pressure to compute the buoyancy and Froude-Krylov moments. In addition, since a mesh of the OWSC is already required for implementing the panel method, it is convenient to use the same mesh for the surface integration of the total fluid pressure.

Table 3-1 summarizes the equation of motion for each model and the equations for evaluating each moment within the model. Section 3.2 presents the solution for the stiffness coefficient function given by Eq. (3.8). Section 3.3 provides the numerical integration algorithm for evaluating Eq. (3.3) for the surface integration of fluid pressure. Finally, Section 3.4 describes the numerical algorithms for evaluating the viscous drag moment using the panel method (Eq. (3.24)) and the strip method (Eq. (3.25)).

Table 3-1: Summary of the candidate numerical models

<table>
<tr><th></th><th>Model 1</th><th>Model 2</th><th>Model 3</th></tr>
<tr><td>Equation of Motion</td><td>Eq. (3.1)</td><td>Eq. (3.1)</td><td>Eq. (3.2)</td></tr>
<tr><td>M_b</td><td>Stiffness coefficient function

Eq. (3.8)</td><td>Stiffness coefficient function

Eq. (3.8)</td><td rowspan="2">Surface integration of fluid pressure

Eq. (3.3)</td></tr>
<tr><td>M_{FK}</td><td rowspan="2">Linear

Eq. (2.11)</td><td rowspan="2">Linear

Eq. (2.11)</td></tr>
<tr><td>M_S</td><td>Linear

Eq. (3.5)</td></tr>
<tr><td>M_d</td><td>Strip method

Eq. (3.25)</td><td>Panel method

Eq. (3.24)</td><td>Panel method

Eq. (3.24)</td></tr>
</table>

3.2 Buoyancy Stiffness Coefficient Function

The first method for implementing nonlinear buoyancy and gravity is by making the stiffness coefficient *C* a function of pitch angle. This function is derived by numerically integrating hydrostatic fluid pressure below the mean water level at various static pitch angle poses of the OWSC. The stiffness coefficient is then obtained from:

$$C(\theta) = -\frac{M_b + M_g}{\theta} = -\frac{1}{\theta}\left(\iint_S -\rho g z (\vec{r} \times \vec{n}) \cdot \vec{j} dS + mgr_g \sin\theta \right) \tag{3.8}$$

Figure 3-1 shows the resulting function. Note that the OWSC is vertical when $\theta = 0$ (see Figure 1-6).

Since the integration in Eq. (3.8) is performed below the mean waterline, the stiffness coefficient function is independent of the incident wave profile and can be precomputed prior to simulation. The stiffness coefficient function can therefore be implemented as a lookup table and requires few additional computations.

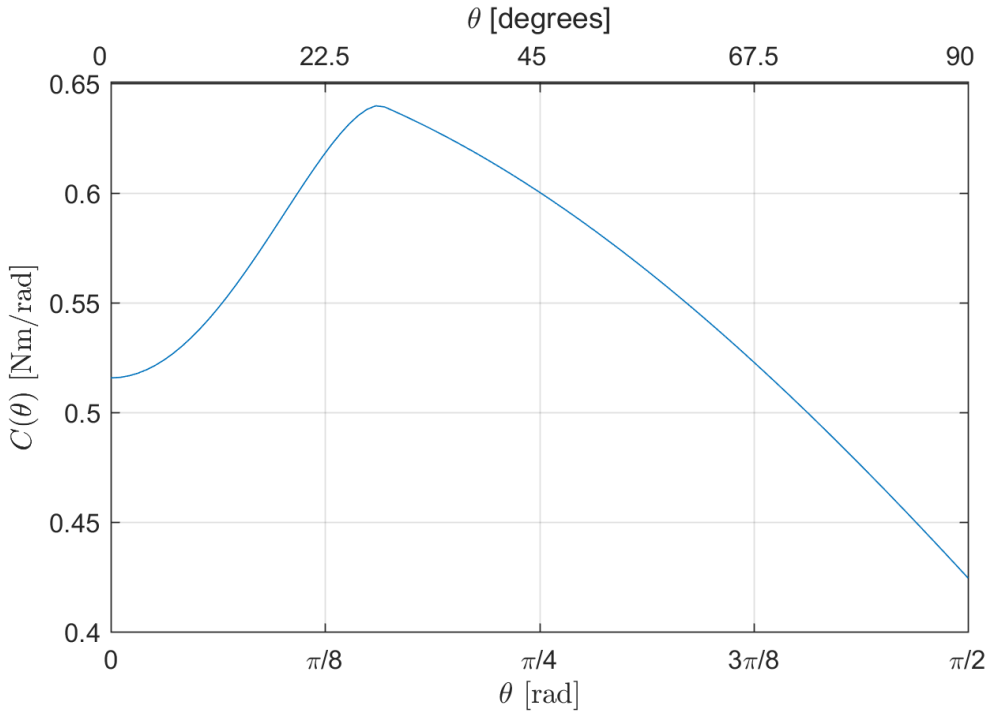

Figure 3-1: Stiffness coefficient function

3.3 Surface Integration of Fluid Pressure

The method in the previous section for extending the buoyant moment can be improved upon by integrating the total fluid pressure over the instantaneous wetted surface of the body, as opposed to only the hydrostatic portion of the fluid pressure below the mean waterline. The numerical integration begins with an approximation of the OWSC surface geometry with a mesh. The mesh is like that used by BEM for deriving the linear hydrodynamic coefficients, however the number of panels is reduced to minimize the number of required computations. Each panel is a quadrilateral; if a panel happens to be triangular, one of its corners is duplicated. Figure 3-2 shows a sample mesh. Different mesh resolutions can be obtained from this mesh by increasing (or

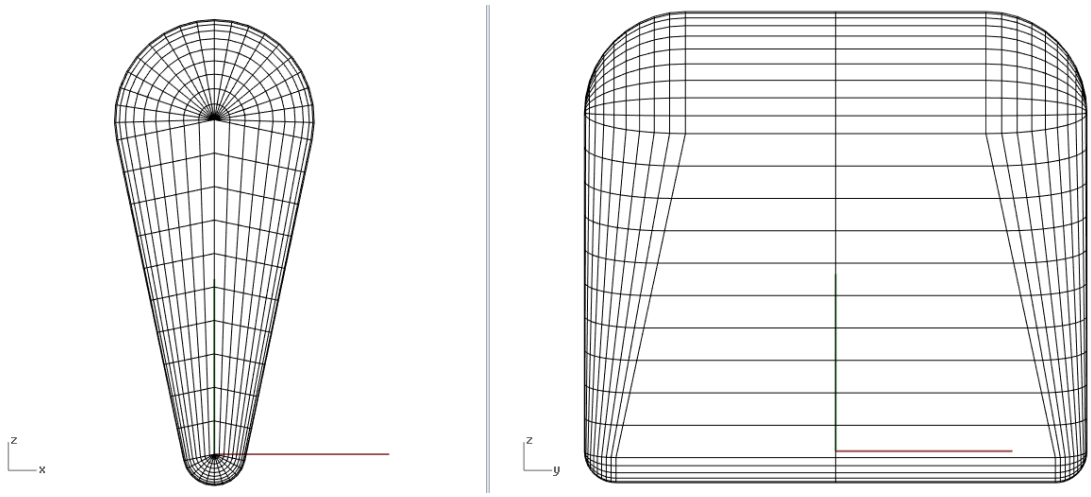

Figure 3-2: OWSC mesh used for numerical surface integrations. Panels that are parallel to the y-axis are not subdivided since wave segments in this thesis only propagate parallel to the x-axis, and therefore there is no variation in the fluid pressure in the y direction. The integration is only performed over one half of the mesh to utilize symmetry about the x-z plane.

decreasing) the number of divisions on each face of the body. Note that panels parallel to the y-axis are not subdivided since there is no variation in the hydrostatic or Froude-Krylov loads in this direction for unidirectional sea states.

With the approximated body surface, the nonlinear buoyancy and Froude-Krylov moments are calculated using:

$$M_b + M_{FK} = \sum_{n=1}^{N_p} M^{(n)} \tag{3.9}$$

where

$$M^{(n)} = \iint_{S^{(n)}} p(\vec{r}^{(n)})(\vec{r}^{(n)} \times \vec{n}^{(n)}) \cdot \vec{j} dS^{(n)} \tag{3.10}$$

and $p(\vec{r}^{(n)}) = p_{dyn}(\vec{r}^{(n)}) - \rho g z^{(n)}$ is the total undisturbed fluid pressure at panel *n*. The dynamic component p_0 is obtained from Eq. (1.28)

Gaussian quadrature can be employed to numerically integrate Eq. (3.10). This technique is commonly used in finite element methods [40]. In effect, this method approximates the integral of a 2D function $y(s,t)$ on the interval $s,t \in [-1,1]$ by a weighted sum of one or more sampling points:

$$\int_{-1}^{1}\int_{-1}^{1} y(s,t)dsdt \cong \sum_{i=1}^{N_q}\sum_{j=1}^{N_q} Wy(s_i,t_j) \tag{3.11}$$

The sampling point locations and weights are optimized to provide the exact integral of a polynomial surface of order $2N_q - 1$ [40]. For general functions, accuracy increases as more sampling points are used. For this work, we compare only first order ($N_q = 1$) and second order ($N_q = 2$) approximations, whose sampling point locations and weights are summarized in Table 3-2 [40].

Table 3-2: Gaussian quadrature point locations and weights

Order (N_q)	**Locations**	**Weight**
1	$s_1 = t_1 = 0$	$W = 4$
2	$s_1 = t_1 = -0.5773$ $s_2 = t_2 = 0.5773$	$W = 1$

Prior to implementing Gaussian quadrature, each panel must be transformed to the *s*-*t* space shown in Figure 3-3 using the isoparametric formulation for quadrilaterals [40]. First the coordinates of the panel corners $\vec{p}_k$ are transformed to a panel fixed coordinate system x', y', z', defined so that y' is normal to the panel and the $x'-z'$ plane is parallel to the panel surface:

$$\begin{bmatrix} x_k' \\ y_k' \\ z_k' \end{bmatrix} = \mathbf{R}\vec{p}_k^{(n)}, \qquad k = 1,2,\ldots,4 \tag{3.12}$$

After the change of coordinates y_k' for each panel corner is equal. The x' and z' coordinates can then be related to *s* and *t* by the transform

$$\begin{bmatrix} x'(s,t) \\ z'(s,t) \end{bmatrix} = \mathbf{N}(s_i, t_j)\mathbf{X} \tag{3.13}$$

where $\mathbf{X} = \begin{bmatrix} x_1' & z_1' & x_2' & z_2' & x_3' & z_3' & x_4' & z_4' \end{bmatrix}^T$ and

$$\mathbf{N}(s,t) = \begin{bmatrix} N_1 & 0 & N_2 & 0 & N_3 & 0 & N_4 & 0 \\ 0 & N_1 & 0 & N_2 & 0 & N_3 & 0 & N_4 \end{bmatrix}$$

$$N_1 = \frac{(1-s)(1-t)}{4} \quad N_2 = \frac{(1+s)(1-t)}{4}$$

$$N_3 = \frac{(1+s)(1+t)}{4} \quad N_4 = \frac{(1-s)(1+t)}{4}$$

Gaussian quadrature can then be implemented so that

$$M^{(n)} = \sum_{i=1}^{N_q}\sum_{j=1}^{N_q} p(\vec{q}_{ij}^{(n)})(\vec{q}_{ij}^{(n)} \times \vec{n}^{(n)}) \cdot \vec{j} \left|\mathbf{J}_{ij}\right| W \tag{3.14}$$

where

$$\vec{q}_{ij}^{(n)} = \mathbf{R}^T \begin{bmatrix} x'(s_i, t_j) \\ y' \\ z'(s_i, t_j) \end{bmatrix} \tag{3.15}$$

$$\left|\mathbf{J}_{ij}\right| = \frac{1}{8}\begin{bmatrix} x_1' & x_2' & x_3' & x_4' \end{bmatrix} \begin{bmatrix} 0 & 1-t_j & t_j - s_i & s_i - 1 \\ t_j - 1 & 0 & s_i + 1 & -s_i - t_j \\ s_i - t & -s_i - 1 & 0 & t_j + 1 \\ 1 - s_i & s_i + t_j & -t_j - 1 & 0 \end{bmatrix} \begin{bmatrix} z_1' \\ z_2' \\ z_3' \\ z_4' \end{bmatrix} \tag{3.16}$$

To reduce computation time, the sampling point locations $\vec{q}_{ij}^{(n)}$ and the Jacobian determinants $\left|\mathbf{J}_{ij}\right|$ are computed prior to simulation. The sampling point locations are initially computed with the OWSC oriented vertically, then at each time step of the simulation these points are rotated about the y-axis by the pitch angle at that time instant.

Increasing the number of sampling points for the Gaussian quadrature is effectively the same as increasing the resolution of the original mesh; a 2nd order integration would have the same number of quadrature points as a 1st order integration with 4 times as many panels. Where 2nd order integration becomes potentially useful is when implementing panel trimming, which is discussed

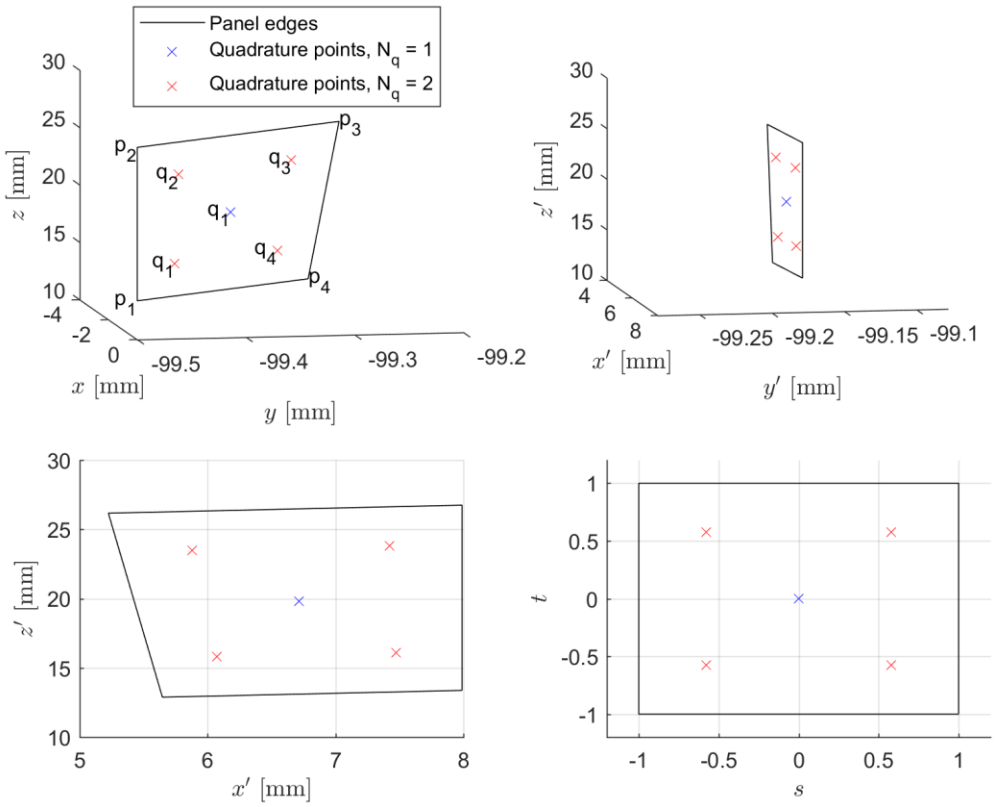

Figure 3-3: Mapping procedure for the quadrature points of each mesh panel. Plot A shows the panel in the global reference frame, while plots B and C shows the panel after the change of coordinates to the panel fixed reference frame. Plot D shows the transformation of the rotated panel to the s-t space. Each plot shows the location of the quadrature points for first and second order approximations.

in the following section. This is because it reduces the number of required panel trimming operations, since a 2nd order integration should require 4 times fewer panels than a 1st order integration with the same number of quadrature points.

3.3.1 Panel Trimming Algorithm

A flaw with the numerical integration described previously is that it assumes that panels are either fully submerged or fully emerged from the fluid. However, since the OWSC is designed to be surface piercing when oriented vertically, often panels are only partially submerged, resulting

in a discontinuous pressure field over the face of the panel. This can result in significant numerical error, since the Gaussian quadrature methods used in this thesis are only accurate for low-order polynomial pressure fields. One option to resolve this issue is to increase the resolution of the mesh. Alternatively, panels can be trimmed at the waterline to ensure that all panels are fully submerged.

Panel trimming is performed using an algorithm developed in [41]. Each panel is first checked to determine whether it intersects the free surface. A linear approximation of the waterline across the panel is then used to trim the panel. The resulting trimmed panel can either have 3, 4 or 5 vertices. Since the numerical integration method is only compatible with quadrilaterals, panels with 3 vertices have one vertex duplicated to form a quadrilateral, while panels with 5 vertices are divided into two quadrilaterals.

The algorithm steps are summarized here:

1. Calculate the linear approximation of the free surface at the panel

$$\eta = \eta_c + \left.\frac{\partial \eta}{\partial x}\right|_{x=x_c} (x - x_c) \tag{3.17}$$

2. Identify the fully and partially submerged panels.
3. For each partially submerged panel
    a. Compute the intersection points with the free surface
    b. Remove non-submerged points and invalid intersection points
    c. Check the number of panel corners
        i. If 3, duplicate the first point to form quadrilateral
        ii. If 4, the panel is already a quadrilateral
        iii. If 5, split the panel into one quadrilateral and one triangle. Duplicate the first point of the triangle to form a quadrilateral
    d. Recalculate the quadrature point locations for each trimmed quadrilateral

4. Merge the trimmed panels with fully submerged panels to obtain trimmed mesh

3.3.2 Convergence and Computation Time

The accuracy of the numerical integration is governed by the resolution of the flap mesh. However, increasing mesh resolution also significantly increases simulation computation time. Therefore, the mesh resolution should be limited to the required number of panels to achieve an accurate solution for the moments acting upon the flap body.

This section compares the convergence rates and computation times of the numerical pressure integration with and without panel trimming implemented. In addition, when panel trimming is implemented, 1st and 2nd order Gaussian quadrature methods are also compared. For convenience, these three integration methods are labelled as follows:

Method 1: Single sample point, panels are not trimmed

Method 2: Single sample point, panels are trimmed

Method 3: Four sample points, panels are trimmed

The required mesh resolution for each method is determined by performing convergence tests on the Froude-Krylov and hydrostatic moments. Convergence of the Froude-Krylov moment is evaluated using the moment time series for a fixed flap in regular waves for different mesh resolutions. Two different regular wave profiles were tested to observe the influence of wave height and frequency on convergence. The wave parameters were selected so that one wave would have a low steepness ($A = 0.01m$ and $T = 2.5s$) and the other a high steepness ($A = 0.03m$ and $T = 1s$). Convergence was determined by plotting the root-mean-square (RMS) error between the moment time series for each mesh resolution and a base line case. The base line was computed using the panel trim method with a very high resolution mesh.

A

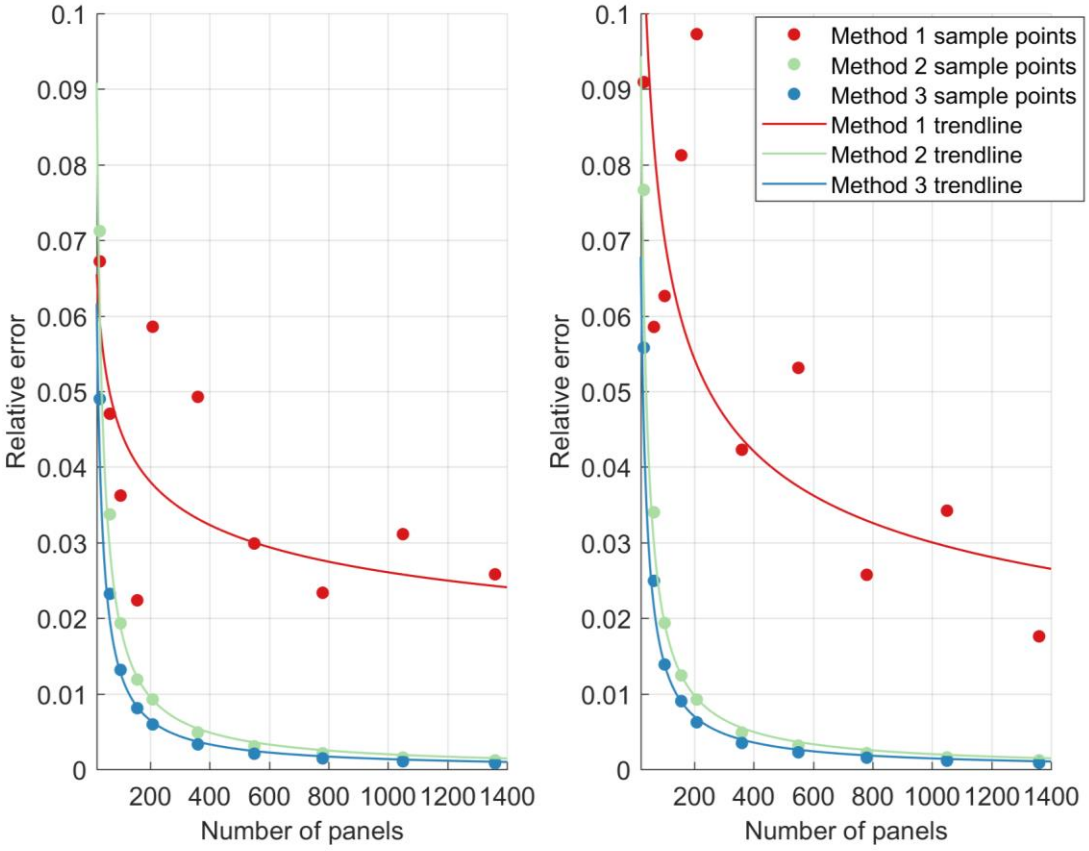

Figure 3-4: Convergence of the Froude-Krylov moment on a fixed flap in regular waves for numerical integration methods 1, 2 and 3. Wave parameters are (left) A=0.01m and T=2.5s, and (right) A=0.03m and T=1s

similar method was used to check convergence of the hydrostatic moment. Since the hydrostatic moment is dominated by pitch angle rather than free surface profile, the moment was computed without an incident wave but with sinusoidal pitch motion. Two amplitudes of pitch motion (0.5 and 1.5 rad) were tested to ensure convergence for different ranges of motion.

Overall method 3 converges the fastest, although the convergence rates of the other methods are close. The one exception is the convergence of the Froude-Krylov moment for method 1, which fails to converge over the range of mesh resolutions shown in Figure 3-4. A resolution of 4800

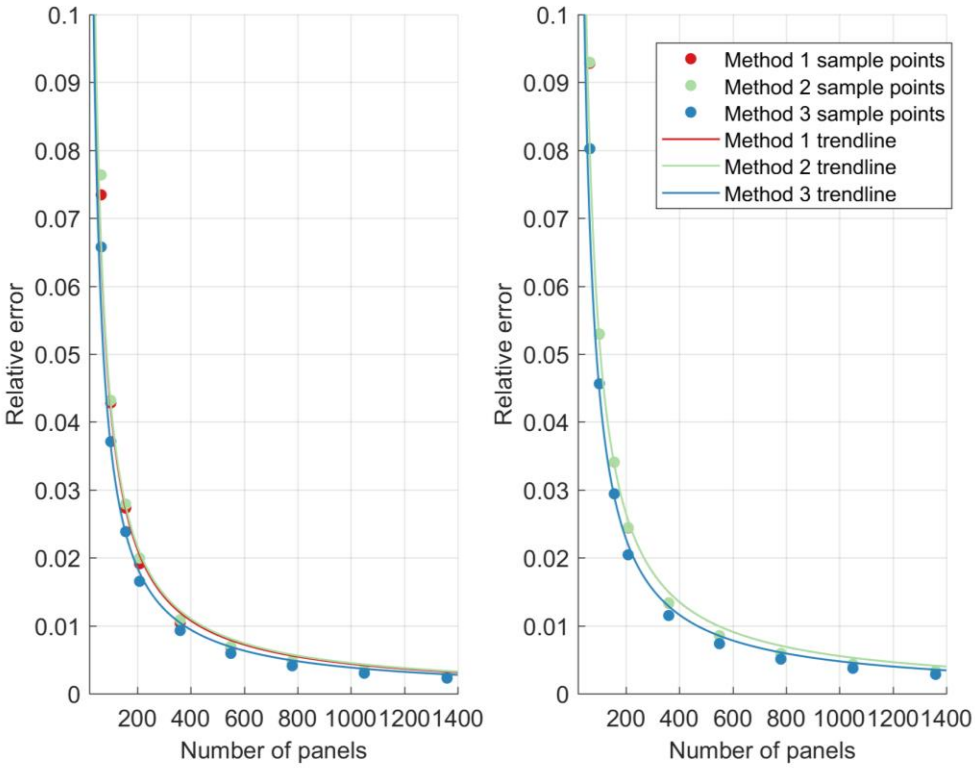

Figure 3-5: Convergence of the hydrostatic moment acting on an oscillating flap for numerical integration methods 1, 2 and 3. Pitch amplitudes are (left) 0.5 rad and (right) 1.5 rad.

panels was determined to be required to achieve convergence of the Froude-Krylov moment for method 1.

These convergence results were used to select a mesh for each method so that the resulting accuracy of each method were approximately equal. The number of panels selected for each method are listed in Table 3-3.

Table 3-3: Mesh resolution for each numerical integration method

Method 1	4800 panels
Method 2	550 panels
Method 3	360 panels

Computation time is governed primarily by the number of quadrature points and the number of panel trim operations. In general, computation time due to quadrature points increases with the number of spectral components defining the wave system. If the sea state consists of a small number of spectral components, then a large number of quadrature points has little consequence on computation time and therefore panel trimming is not required. However, for irregular sea states or waves with a high number of spectral components, then implementing panel trimming can reduce computational expense by reducing the required number of quadrature points while maintaining the same level of accuracy in the approximation. Of course, this is only an improvement if the computational savings overcomes (is more significant than) the computational expense of the panel trimming algorithm itself.

The computation times required to evaluate each method 500 times are illustrated in Figure 3-6, which shows that panel trimming becomes more computationally efficient for sea states with 6 or more segments. Note that the computation time of method 3 is greater than method 2, even though method 3 requires a mesh with fewer panels. Therefore, method 2 is overall a better method than method 3. In general, method 1 should be used when modelling in regular waves, and method 2 should be used when modelling irregular waves.

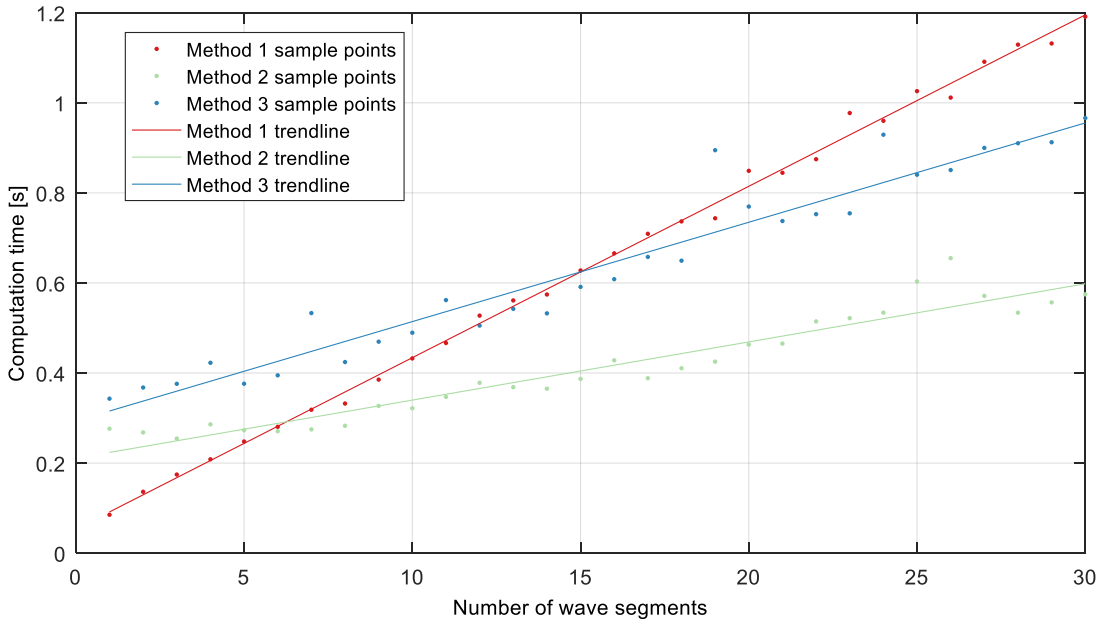

Figure 3-6: Numerical integration computation times required to perform 500 iterations of methods 1, 2 and 3 with different numbers of wave segments. A linear fit is applied to each series to estimate the trade-off points between each method.

3.4 Viscous Drag

In Section 3.1, two methods of computing the drag moment, the panel and strip methods, were introduced. This section presents the algorithms for both options.

3.4.1 Panel Method

The panel method involves numerically integrating the drag force over the surface of the body using the mesh shown in Figure 3-2. The advantage of this method in comparison to the strip method is that it can be applied to more general body shapes which are not necessarily slender. In this work, it is also more convenient since the body is already discretized for the nonlinear Froude-Krylov and hydrostatic moments.

Consider the surface element dS located at the quadrature point $\vec{q} = \begin{bmatrix} q_x & q_y & q_z \end{bmatrix}^T$. The relative velocity between the fluid and body is given by:

$$\vec{u}_r = \vec{u} - \dot{\theta}\left(\vec{j} \times \vec{q}\right) = \begin{bmatrix} u - \dot{\theta} q_z \\ 0 \\ w + \dot{\theta} q_x \end{bmatrix} \tag{3.18}$$

where the fluid velocity components *u* and *w* are given in Eq. (1.29) and Eq. (1.30) respectively. The drag force acting upon the surface element *dS* can then be expressed in terms of its *x* and *z* components as

$$\begin{aligned} dF_{dx} &= \frac{1}{2}\rho C_d (u - \omega q_z)\left|u - \omega q_z\right|\left|n_x\right| dS \\ dF_{dz} &= \frac{1}{2}\rho C_d (w + \omega q_x)\left|w + \omega q_x\right|\left|n_z\right| dS \end{aligned} \tag{3.19}$$

where n_x and n_z are the *x* and *z* components of the surface normal vector in the global reference frame. The drag moment can then be expressed as

$$M_d = \sum_{n=1}^{N_p} M_d^{(n)} \tag{3.20}$$

Where:

$$M_d^{(n)} = \iint_{S^{(n)}} q_z^{(n)} dF_{dx}^{(n)} - \iint_{S^{(n)}} q_x^{(n)} dF_{dz}^{(n)} \tag{3.21}$$

Using Gaussian quadrature to numerically integrate (3.21) over the panel then gives

$$M_d^{(n)} = \frac{1}{2}\rho C_d \sum_{i=1}^{N_q}\sum_{j=1}^{N_q}\left(q_z^{(n)} u_{ij}^{(n)}\left|u_{ij}^{(n)}\right|\left|n_x^{(n)}\right| - q_x^{(n)} w_{ij}^{(n)}\left|w_{ij}^{(n)}\right|\left|n_z^{(n)}\right|\right)\left|\mathbf{J}\right|_{ij}^{(n)} W \tag{3.22}$$

where

$$\begin{aligned} u_{ij}^{(n)} &= u(\vec{q}_{ij}^{(n)}) - \omega q_z^{(n)} \\ w_{ij}^{(n)} &= w(\vec{q}_{ij}^{(n)}) + \omega q_x^{(n)} \end{aligned} \tag{3.23}$$

Note that $q_x^{(n)}$ and $q_z^{(n)}$ are the *x* and *z* components of $\vec{q}_{ij}^{(n)}$ which is given by Eq. (3.15), and $\left|\mathbf{J}\right|_{ij}^{(n)}$ is given by Eq. (3.16).

Note that in the original Morisons' equation in Eq. (1.15), the drag force is applied over the cross-sectional area of the body. However, because the panel method integrates over the whole

surface area of the flap, drag forces will be applied to both leading and trailing surfaces of the OWSC as it rotates, resulting in the overall drag moment being double-counted [31]. This can be resolved using the method in [31], by dividing the overall drag moment given in Eq. (3.22) by two:

$$M_d^{(n)} = \frac{1}{4}\rho C_d \sum_{i=1}^{N_q}\sum_{j=1}^{N_q}\left(q_z^{(n)}u_{ij}^{(n)}\left|u_{ij}^{(n)}\right|\left|n_x^{(n)}\right| - q_x^{(n)}w_{ij}^{(n)}\left|w_{ij}^{(n)}\right|\left|n_z^{(n)}\right|\right)\left|\mathbf{J}\right|_{ij}^{(n)} W \tag{3.24}$$

With this correction, the magnitude of the drag coefficients for this method and the strip method discussed in the following section should be approximately equal.

3.4.2 Strip Method

For the strip method, a discrete approximation of the integral given in Eq. (3.6) is implemented using the discretization of the flap cross section shown in Figure 3-7. The area is discretized in smaller intervals near the top edge to account for variations in the free surface profile due to the

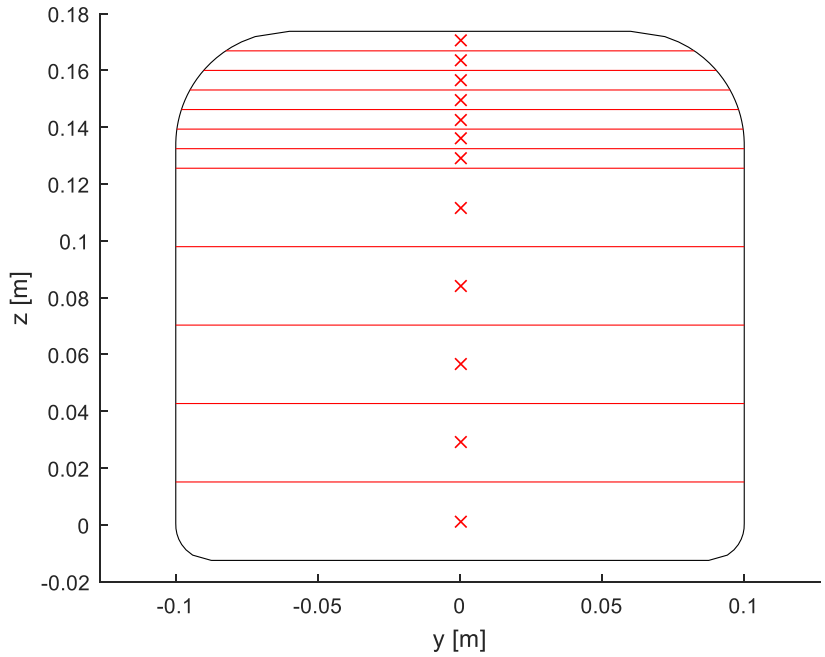

Figure 3-7: Discretization of the model cross-section for the strip method of computing drag. Fluid properties for each panel are computed at $\boldsymbol{r}^{(k)}$, whose locations are marked by 'x'.

incident waves. The fluid velocity is evaluated at the centers of each panel, then the drag moment is computed using Eq. (3.25):

$$M_d(t) = \frac{1}{2} C_d \rho \sum_{k=1}^{N} (u_n^{(k)} - r^{(k)}\dot{\theta}) \, | u_n^{(k)} - r^{(k)}\dot{\theta} \, | r^{(k)} dA^{(k)} \tag{3.25}$$

where $dA^{(k)}$ represents the area of the cross-section defined at $r^{(k)}$, and

$$u_n = u\cos\theta - w\sin\theta \tag{3.26}$$

is the fluid velocity normal to the flap at $r^{(k)}$.

3.5 Model Comparison

This section compares the candidate model predictions for the OWSC response amplitude in regular waves. This is purely a numerical exercise to observe the ranges of regular wave heights and periods where divergence between the candidate models will occur. Computation times for each model are also presented in this section – the computational requirements of the candidate models may be considered when selecting a recommended model if the candidate model predictions are nearly equivalent over the range of realistic wave heights and periods.

OWSC Response Amplitudes

The response amplitudes of the candidate models are obtained by simulating each model in regular waves of different heights and periods. The resulting RAOs are presented in Figure 3-8 for $C_d = 1$ and Figure 3-9 for $C_d = 2$, along with the corresponding RAO for the baseline model given by Eq. (2.14). The C_d values of 1 and 2 are simply initial guesses for the magnitude of the drag coefficient based on the work of [11]. The linear model RAOs are scaled by the amplitude of the incident wave before comparing with the candidate model results. For these comparisons, the maximum wave height is limited to 5cm, corresponding to 2m at full scale, while the maximum significant wave height at the target deployment site is 6m (see Chapter 4). This limitation on wave height is to prevent the OWSC model from colliding with the sea floor during a simulation, which occurs for wave heights larger than 5cm when $C_d = 1$. The inclusion of PTO and braking moments

in the model would prevent these collisions, however since the focus of this section is upon observing differences in model dynamics due to different approaches for evaluating the layers of the FSI problem, these moments are left out until Chapter 6, where full scale power production estimates are obtained.

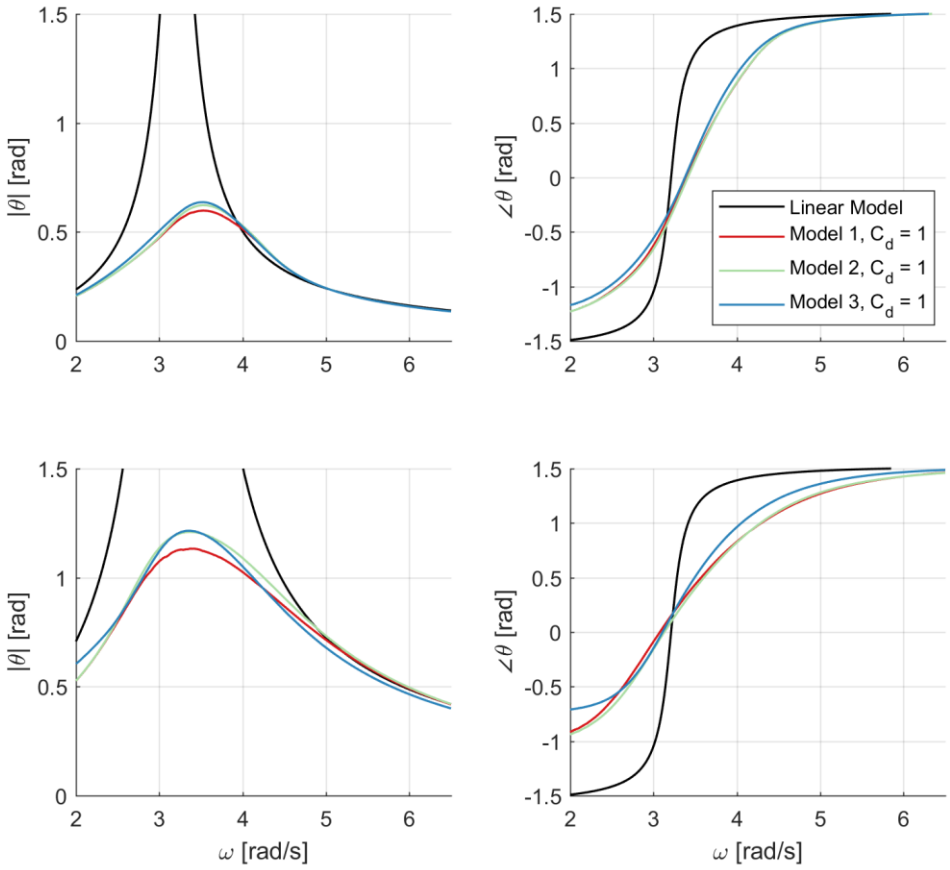

Figure 3-8: Candidate model pitch responses with drag coefficient equal to 1. Rows from top to bottom correspond to wave heights of 2 and 5cm, and columns from left to right correspond to the modulus $|\theta|$ and argument $\angle\theta$ of the resulting pitch motion amplitude.

Figure 3-8 and Figure 3-9 demonstrate that there is little difference in the model predictions for low wave amplitudes, but as wave height increases more notable differences can be observed in both the amplitude and phase of the resulting pitch motions. The magnitude of these differences also varies with the incident wave frequency. The curves for Models 1 and 2 can be compared to observe differences due to the different approaches for approximating viscous drag, and Models 2 and 3 can be compared to observe differences due to the surface integration of total fluid pressure for computing buoyant and Froude-Krylov moments. Note that these comparisons are a purely

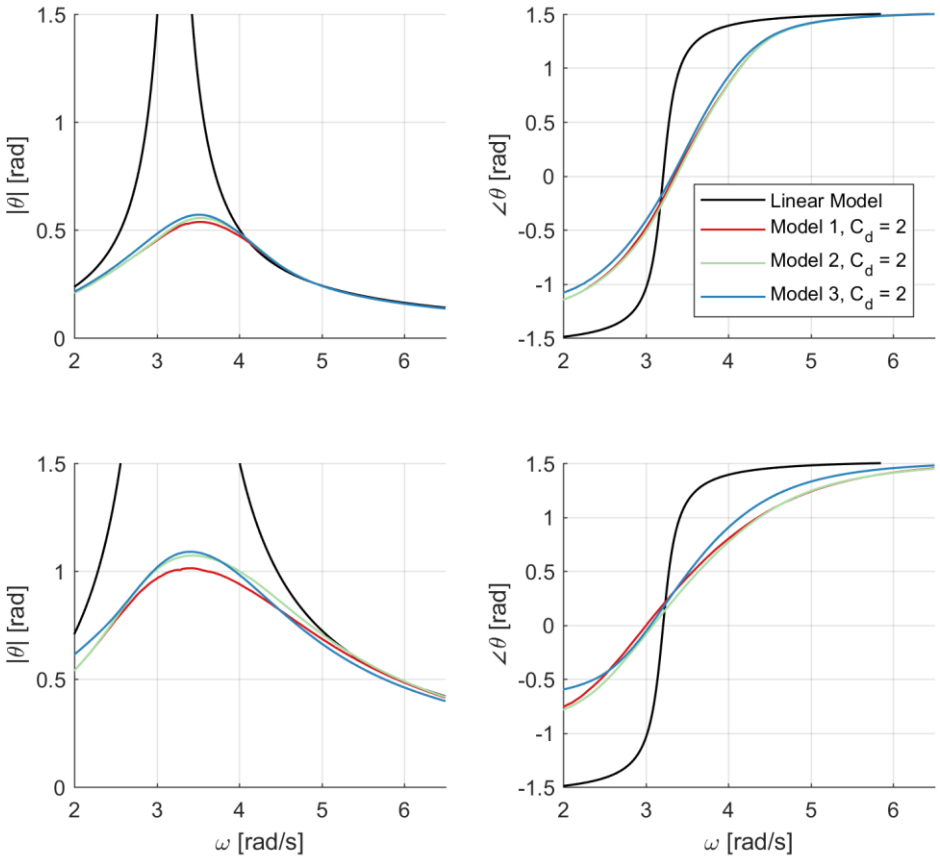

Figure 3-9: Candidate model pitch responses with drag coefficient equal to 2. Rows from top to bottom correspond to wave heights of 2 and 5cm, and columns from left to right correspond to the modulus $|\theta|$ and argument $\angle\theta$ of the resulting pitch motion amplitude.

numerical exercise, and there is no truth signal for comparison at this stage. An assessment of model accuracy is left for Chapter 5, which compares these candidate model predictions to experimental data.

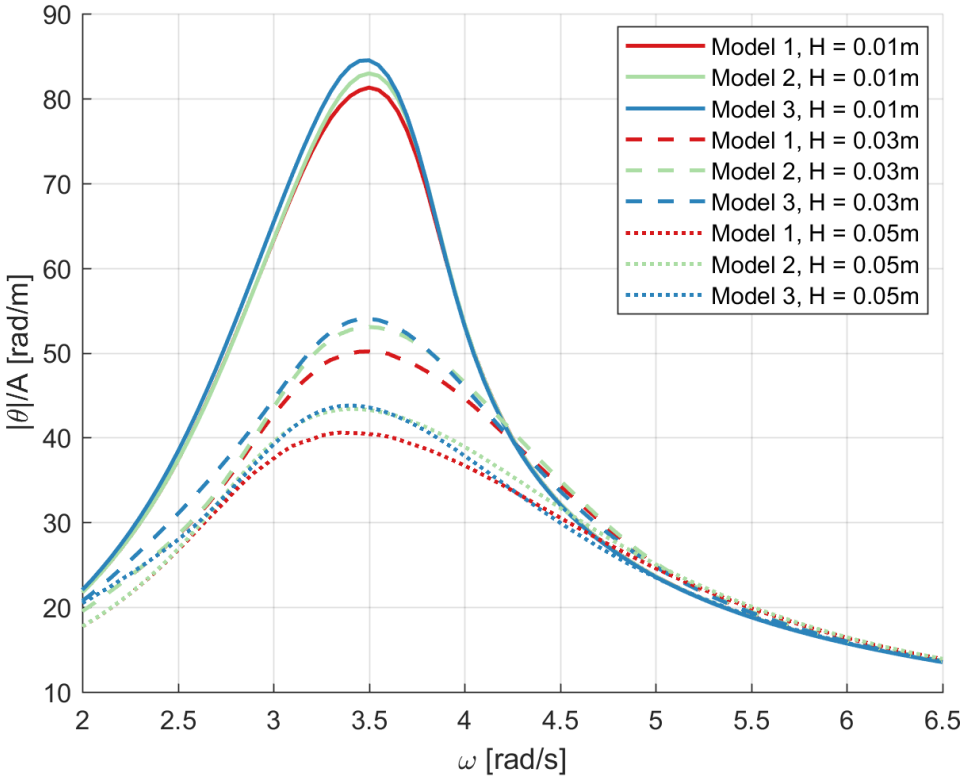

Figure 3-10: Candidate model response amplitudes normalized by wave amplitude. These results were obtained with $C_d = 1.5$

Divergence in the candidate models can be more readily observed in Figure 3-10, which compares the response amplitudes of Models 1 to 3 normalized by wave amplitude for three different wave heights. From this figure it is observed that, unlike the baseline model from Eq. (2.14), there is no longer a linear relationship between the amplitude of pitch motion and the incident wave amplitude. Furthermore, Figure 3-11 directly plots the divergence between the candidate model predictions for response amplitude. Divergence is plotted in terms of the difference in response amplitude predictions, given by:

$$\Delta|\theta|_{ij} = |\theta|_j - |\theta|_i \tag{3.27}$$

where $|\theta|_i$ and $|\theta|_j$ are the response amplitudes predicted by Models i and j respectively. The resulting plots confirm that model divergence is low for small wave heights but increases as wave height increases. The largest divergence is between Models 1 and 3 and occurs near the resonant frequency of the device (around 3.5 rad/s). The magnitude of this divergence is 0.08 rad, which is roughly 8% of the total response amplitude.

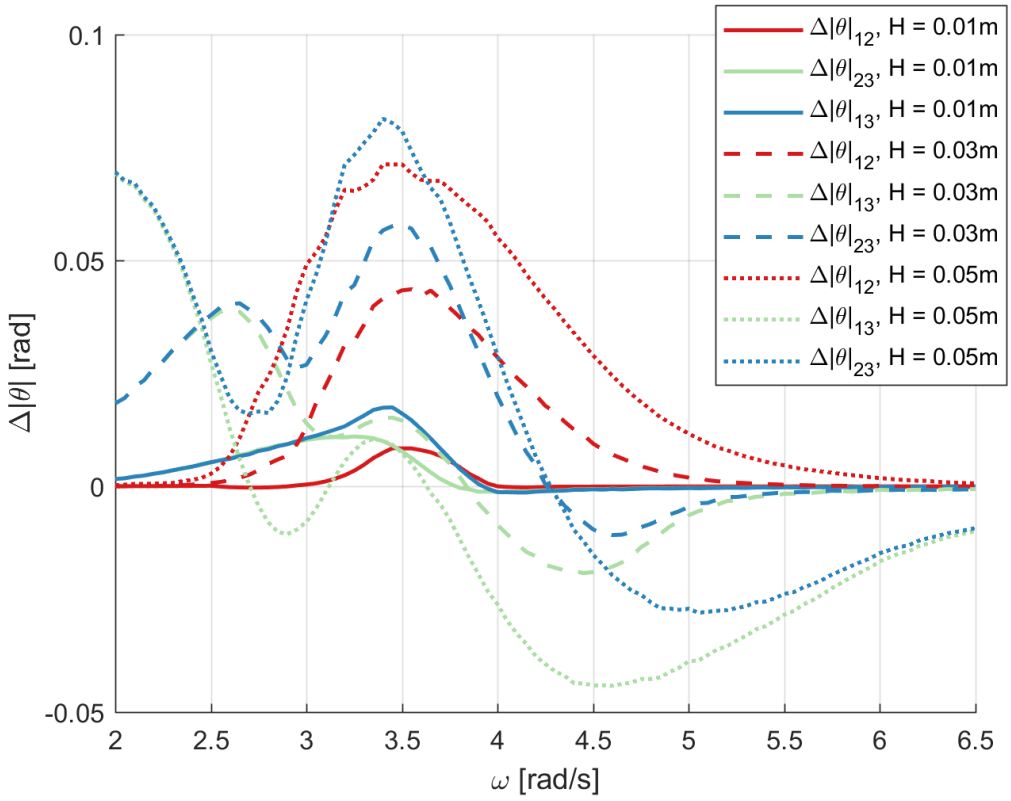

Figure 3-11: Candidate model response amplitudes normalized by wave amplitude. These results were obtained with $C_d = 1.5$

Computation Times

The computation times for each candidate model are presented in **Figure** 3-12 and are normalized by the duration of the simulation. The simulations were run in MATLAB/Simulink on a Lenovo Ideapad Y700 with an Intel Core i7-6700HQ CPU at 2.60GHz. Computation times were obtained for different numbers of wave segments ranging from 1 to 100. For each number of wave segments, 60 simulations were performed with different wave heights and periods. If the number of wave

segments was greater than 1 (irregular waves) then the wave profile was generated using the Pierson-Moskowitz spectral shape from Eq. (1.10), and significant wave height and peak period were varied. The average run times for the 60 simulations are presented in Figure x. The results indicate that Model 1 requires approximately an order of magnitude less computation time than the other candidate models, as it does not require panel operations. The computation times of Models 2 and 3 are nearly equivalent. The number of wave segments significantly affects run time; for example, the computation times for Models 2 and 3 for 100 wave segments is roughly 10 times greater than when simulating only 1 wave segment.

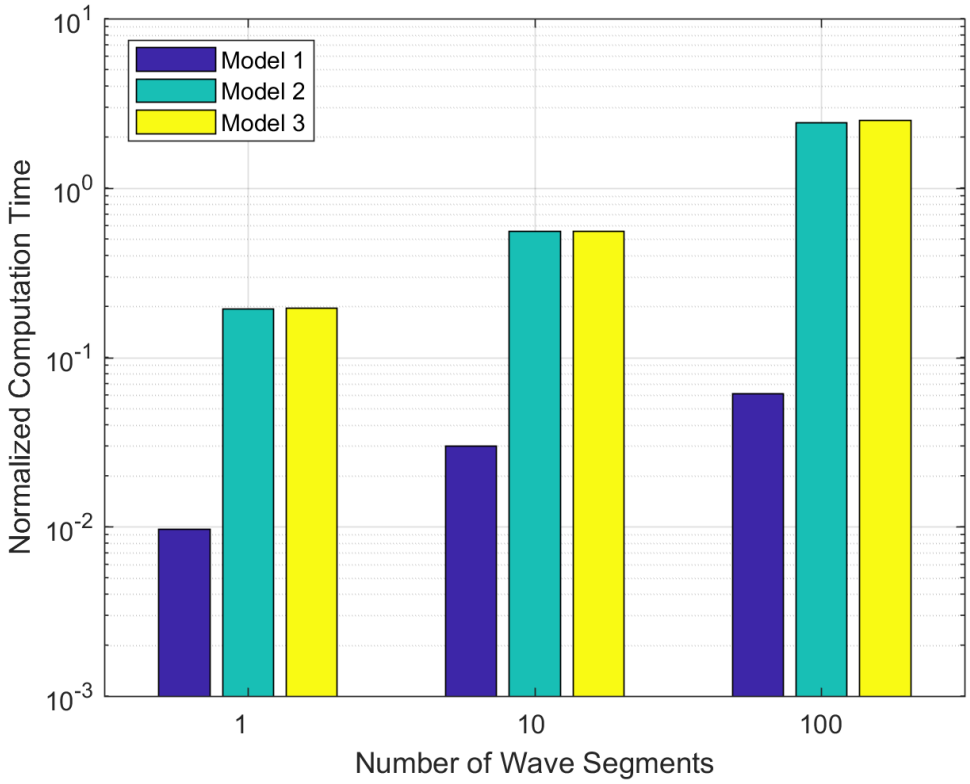

Figure 3-12: Normalized computation times for the candidate models.

3.6 Chapter Summary

In this chapter, algorithms were developed for computing nonlinear buoyancy, Froude-Krylov and drag moments. Three models incorporating different combinations of algorithms were then compared to observe their influence upon the dynamics of the OWSC. In addition, different approaches for computing the numerical surface integration were considered, including the number of quadrature points per panel and whether panel trimming at the waterline should be performed. In summary, it was determined that a single quadrature point per panel and trimming the panels at the waterline minimizes computational expense while maintaining a sufficiently close approximation of the original moment. One exception is when the incident sea state is monochromatic, in which case it is faster to not perform panel trimming and compensate by increasing the number of mesh panels.

In general, incorporating nonlinear buoyancy and viscous drag in an OWSC model has a considerable influence upon the dynamics in comparison to the linear baseline model from Chapter 2, and should therefore be included in all the nonlinear models considered. Differences between the strip and panel methods for drag arise as the amplitude of pitch motion increases. It is unclear at this stage which method for computing drag is more accurate, and this will be addressed by comparing the numerical models to experimental results. Finally, implementing the surface integration of fluid pressure to compute buoyancy and Froude-Krylov moments has a minor influence upon the OWSC dynamics in low amplitude waves, however the effect on model dynamics increases for larger wave heights. Overall the largest divergence between candidate model predictions was observed between Models 1 and 3 near the resonant frequency of the OWSC for wave heights of 0.05m, the largest wave height considered in the numerical analysis. The magnitude of this divergence was around 8% of the total pitch response amplitude at the resonant frequency.

Computation times for the candidate models were also compared, as computational requirements may be considered as a secondary criterion when selecting a recommended model in the following chapters. Computation times for all models was increased based on the number of wave segments defining the input wave profile. However, Model 1 had significantly lower computation times than he other candidate models as it does not require panel operations. It is therefore more practical for

long term power production simulations, especially when simulating irregular wave conditions with many wave segments. However, the divergence observed between the candidate models for large wave heights indicates that although Model 1 is more convenient for long term simulations, it may be less accurate than the other candidate models in large wave height conditions.

Chapter 4: Environmental Test Conditions

In Chapter 3, the divergence between candidate model predictions was observed for a range of incident wave heights and frequencies. This chapter aims to identify ranges of wave heights and frequencies which can be produced experimentally, so that measurements of the OWSC motion can be collected in wave conditions where significant divergence occurs in the candidate model predictions. Initial ranges of wave parameters are selected at full scale based on the common ranges of ocean wave heights and frequencies off the coast of Vancouver Island. These ranges, at the 1:40 model scale, are then adjusted to fall within the feasible range of wave conditions which can be generated in the small-scale wave tank used in this work. Experiments conducted over these ranges of parameters are then used to identify which candidate model best predicts the OWSC motion across all wave conditions; these experiments and their results are further discussed in Chapter 5.

In this chapter, a location off the west coast of Vancouver Island is selected as a suitable deployment site. This site is also used in Chapter 6 for estimating annual power production (APP). The wave climate at this location is characterized by a wave histogram representing the hours of occurrence of specific wave conditions as defined by significant wave height and energy period. The data underlying the histogram comes from a numerical SWAN model developed in [19] that has a temporal resolution of 3 hours and a duration of 10 years from January 2004 to January 2014. The SWAN model was previously validated against real world wave measurements in [19].

Although the real-world sea states are irregular, tank testing is primarily performed in regular waves due to difficulty in generated irregular sea states that are not limited by the stroke length of the wavemaker. An equivalent histogram of regular wave heights and periods is therefore created from the original histogram using the joint probability distribution model developed by Longuet-

Higgins in [42]. This histogram is then used to determine a representative range of regular wave heights and periods for tank testing.

Due to the likelihood of wave reflections in the small-scale wave tank used in this work, a new method of comparing numerical and experimental predictions of OWSC motion is developed to account for the presence of reflected waves. With this method, the experimental wave profile is treated as a partially standing wave system to account for the non-negligible end wall reflections. The primary challenge with the experimental analysis is that, due to the short length of the tank, waves that are scattered or radiated from the OWSC model are quickly re-reflected from the wavemaker paddle and distort the incident wave profile. This eliminates the possibility of estimating the wave profile at the model by measuring the free surface at the model position without its presence [30]. To resolve this problem, a modified reflection analysis is developed to account for the radiated and scattered waves which are produced by the OWSC model, allowing the wave profile at the model position to be estimated while the model is present in the tank.

4.1 Deployment Site

The selected deployment site is at the mouth of Florencia Bay, near Amphitrite Bank which has been cited as a promising location for WEC deployment [16]. Although the OWSC is designed to operate in 8m of water, SWAN results are obtained from a previous study at a location near the target site where the water depth is 10m. These results are then transformed to the 8m depth location as described in Section 4.1.2. Prior to this, a unidirectional approximation of the wave climate at the 10m depth location is obtained in Section 4.1.1, since ultimately this chapter is interested in identifying suitable ranges of wave heights and frequencies for the unidirectional wave profiles to be generated in the wave tank.

Figure 4-1: Location of the selected deployment site. The right image shows the location along the west coast of Vancouver Island, and the right image shows the location at the mouth of Florencia Bay.

4.1.1 Unidirectional Approximation of the Wave Climate

While the SWAN model resolves the directional wave spectrum, since the small scale UVic wave tank only produces unidirectional wave system it is logical to fold the directional wave spectra produced by SWAN into unidirectional ones. To check how the unidirectional approximation impacts the performance assessment that will be completed in Chapter 6, the direction of maximum directionally resolved wave power (θ_J) and directionality coefficient (d), as defined in [19], [43], are plotted over the course of one year at the 10m deep SWAN sample point. Figure 4-2 shows that the directionality coefficient d is always near unity, indicating that directional spread in the sea state is low. Note however that the propagation direction θ_J varies by roughly $\pm 20°$ over the course of a year. Therefore, treating the incident waves as always perpendicular to the OWSC, as in Chapter 6, could lead to an overestimation in power production.

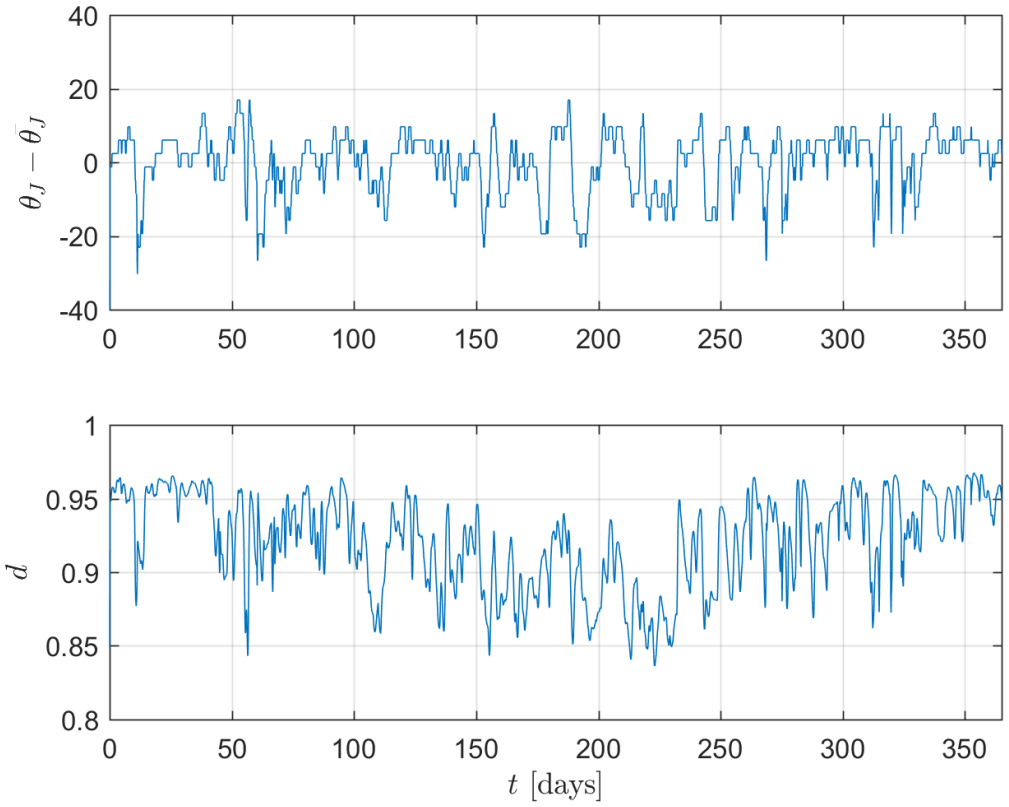

Figure 4-2: Directional properties of the wave climate at the target deployment site over one year. Top: Variability of the direction of maximum directionally resolved wave power. Bottom: directionality coefficient.

4.1.2 Wave Histogram at the Target Location

As mentioned previously, an initial estimate of the wave histogram at the deployment site is obtained at a nearby 10m depth location. Based on the findings in [44], a Pierson-Moskowitz spectrum approximates well the spectral shape of irregular waves on the west coast of Vancouver Island. To account for shoaling between the 10m and 8m depth locations, the shape of the Pierson-Moskowitz spectrum corresponding to each bin of the wave histogram from the 10m depth location is adjusted using [21]:

$$S_2(\omega) = S_1(\omega)\frac{C_{g1}(\omega)}{C_{g2}(\omega)} \tag{4.1}$$

where S_1 and S_2 are the wave spectra at the 10m deep SWAN sample point and the 8m deep deployment location, while C_{g1} and C_{g2} are the group velocities for regular waves of frequency ω at the two locations. The variance density S_1 is calculated using the Pierson-Moskowitz spectral shape defined in (1.10). The resulting shape of S_2 is then used to obtain the new significant wave height and energy period for that wave profile using Eq. (1.7) and (1.8).

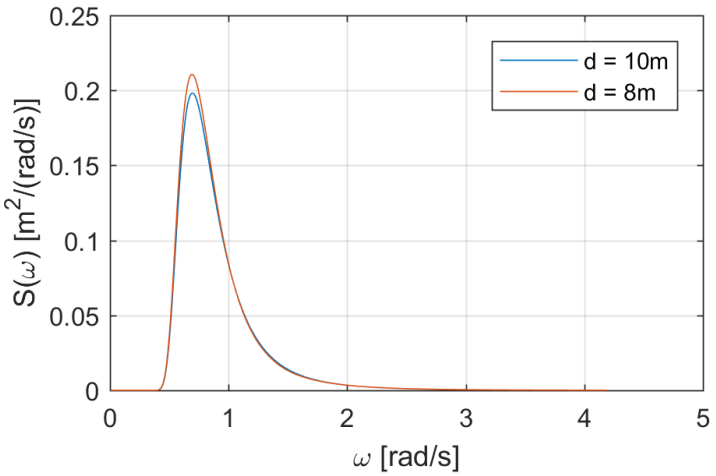

Figure 4-3: Original (10m depth) and transformed (8m depth) Pierson-Moskowitz spectrum For the original spectrum, $H_s = 1.25m$ and $T_e = 7.75s$

After transforming the SWAN results to the 8m water depth, the resulting significant wave heights and energy periods are re-binned to create a wave histogram for the deployment site. The resulting histogram is shown in Table 4-1. Once again, the spectral shape within each cell is modelled using the Pierson-Moskowitz function; although the transformation from 10m to 8m water depths changes the shape of the original spectrum, these changes are minor and a Pierson-Moskowitz spectrum still provides a good approximation.

Table 4-1: Wave histogram for the deployment location. Each bin represents the average number of hours the sea state occurs per year. The cells with the thick outside border are generated experimentally

Wave Energy Period [s] \ Significant Wave height [m]	0.25	0.75	1.25	1.75	2.25	2.75	3.25	3.75	4.25	4.75	5.25	5.75	6.25
5.25	0	0	0	0	0	0	0	0	0	0	0	0	0
5.75	0	0	0	0	0	0	0	0	0	0	0	0	0
6.25	0	1	2	0	0	0	0	0	0	0	0	0	0
6.75	0	8	21	4	0	0	0	0	0	0	0	0	0
7.25	0	38	73	10	0	0	0	0	0	0	0	0	0
7.75	0	62	213	57	7	1	0	0	0	0	0	0	0
8.25	0	79	333	119	22	4	0	0	0	0	0	0	0
8.75	0	91	394	199	42	11	4	0	0	0	0	0	0
9.25	0	85	404	282	112	34	11	1	0	0	0	0	0
9.75	0	60	332	331	195	80	23	7	3	0	0	0	0
10.25	0	42	259	317	263	144	52	17	2	1	0	0	0
10.75	0	27	194	237	243	213	108	36	8	2	0	0	0
11.25	0	16	102	134	187	192	129	61	16	7	2	0	0
11.75	0	14	72	76	133	157	125	62	26	13	4	1	0
12.25	0	8	25	72	72	101	88	81	31	12	4	0	0
12.75	0	6	20	39	44	58	60	59	33	12	6	1	0
13.25	0	2	14	15	37	31	31	31	32	19	6	1	0
13.75	0	1	3	8	18	10	23	15	19	11	5	2	0
14.25	0	1	3	5	12	4	10	6	9	7	9	4	0
14.75	0	0	1	1	8	5	1	3	5	1	4	3	0
15.25	0	0	0	2	2	2	3	1	4	1	0	1	0
15.75	0	0	0	2	1	1	2	0	0	0	0	0	0
16.25	0	0	0	1	2	0	0	0	0	0	0	0	0
16.75	0	0	0	1	0	0	0	0	0	0	0	0	0
17.25	0	0	0	0	0	1	0	0	0	0	0	0	0
17.75	0	0	0	0	0	0	0	0	0	0	0	0	0

4.2 Wave Tank Facility

Experimental OWSC tests are conducted in a water tunnel at the University of Victoria. Typically, the tunnel is used for conducting continuous flow tests. The test section of the tank consists of transparent acrylic walls to visualize the flow, and is 45cm wide and 2.5m long. The maximum water depth in the test section is 45cm. When operating as a water tunnel, flow enters the test section through a converging nozzle, which contains honeycomb screens to straighten the flow and remove large eddies. Flow then exits through a diffuser before being recirculated back to the start of the tunnel.

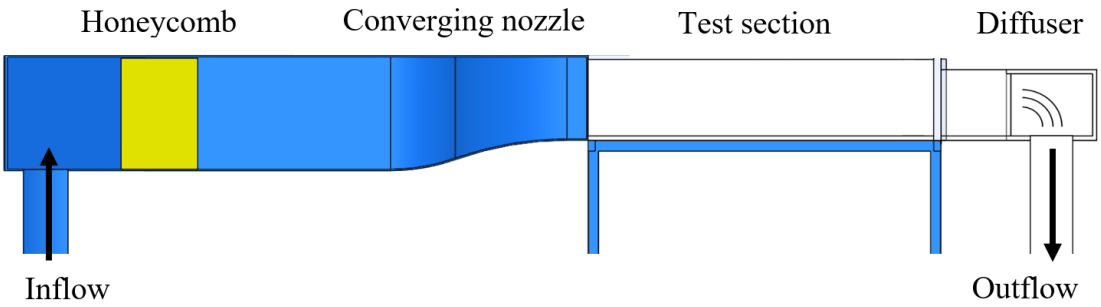

Figure 4-4: Schematic of the wave tank facility when operating as a water tunnel

When operating as a wave tank, a wavemaker is installed adjacent to the diffuser, which generates waves propagating towards the converging nozzle. The wavemaker has a piston-style paddle, which is ideal for shallow water testing as the velocity of the piston closely approximates fluid particle velocity beneath shallow water wave [21]. The piston is driven by a belt-driven linear actuator (Parker). The actuator is mounted vertically, and a system of linear bearings is used to convert the vertical motion of the actuator into horizontal motion of the piston.

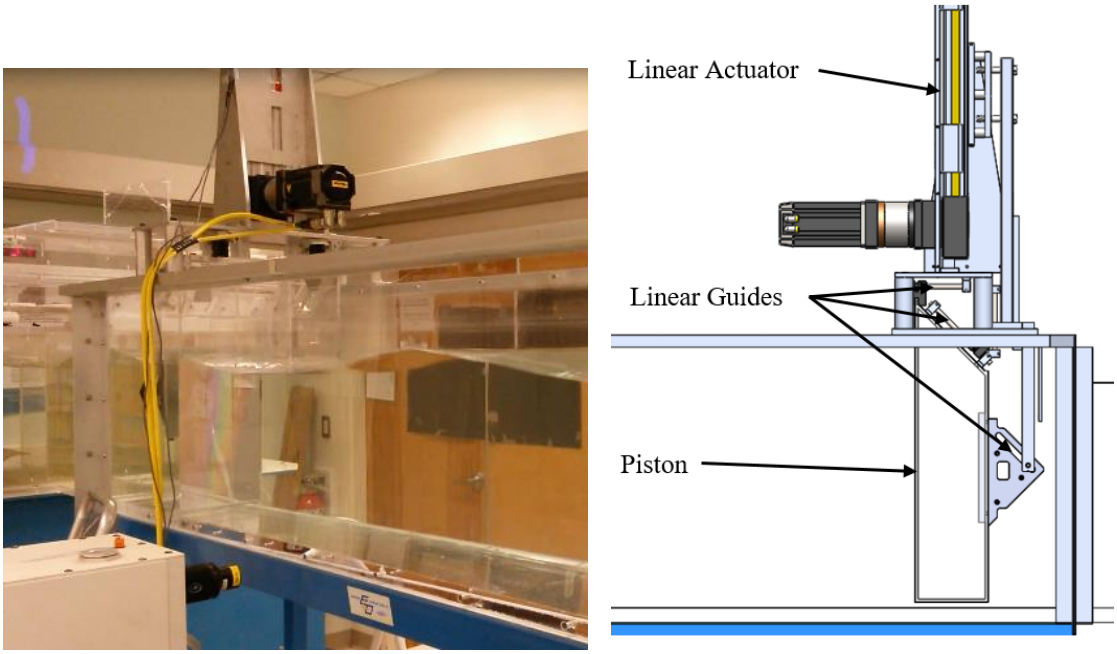

Figure 4-5: The piston-style wavemaker in the wave flume. Left: image of the wavemaker in operation. Right: schematic of the wavemaker with labels

The motion profile of the linear actuator is defined using a "cam profile", a series of target points which define the position of the actuator in time. For example, for regular wave tests the cam profile is a discrete sine wave. The user can then modify the amplitude and period of the motion profile using two parameters, one which scales the magnitude of the target points, and the other which defines the cycle period of the cam profile.

Model Scaling

Experimental modelling of WECs and other offshore structures use Froude scaling to ensure similarity of the ratio between inertial and gravitational loads upon offshore structures. Unfortunately, Froude scaling does not provide similarity of the viscous loads, which scale with Reynolds number. In general, viscous forces at model scale are larger than their full-scale equivalent [8]. Froude scaling ratios for distances and time are presented in Table 4-2.

In

Table 4-2: Froude scaling ratios

	Scaling
Distance	S
Time	$S^{0.5}$

Chapter 2, a scale of 1:40 for the experimental OWSC model was introduced. This scale is selected based upon the dimensions of the wave tank test section, which are shown in Figure 4-6. The width of the tank, not shown in Figure 4-6, is 0.45m. At 1:40 scale, the water depth is 20cm and the model width is 20cm.

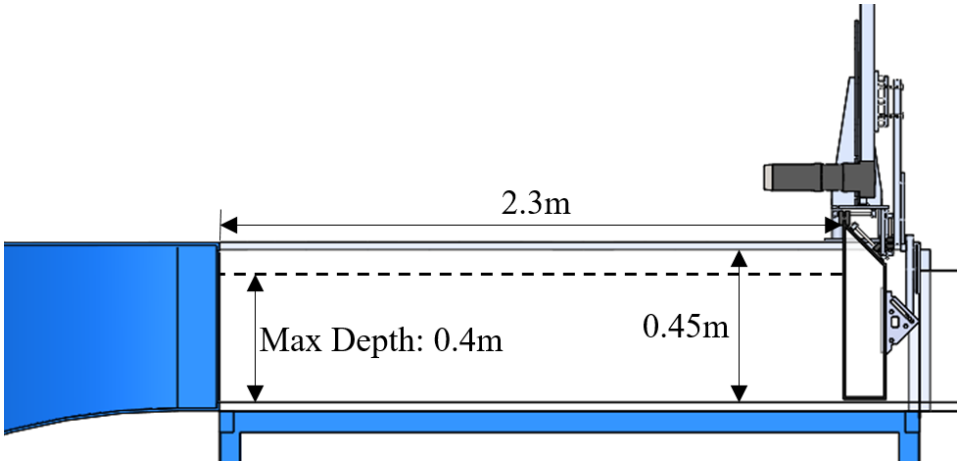

Figure 4-6: Dimensions of the wave tank test section. The maximum depth is a suggested value to prevent wave crests from striking the roof of the converging nozzle at the end of the test section. The width of the test section (not shown) is 0.45m.

The selection of the 1:40 OWSC model scale was based upon the following considerations:

- At larger scales, the maximum wave heights that the wavemaker can produce would be severely limited by the piston stroke length. Channel effects upon the OWSC dynamics would also become more significant due to proximity between the model edges and the channel walls.

- Smaller scales would experience more error in the hydrodynamics due to viscous effects, which are not properly scaled by Froude number. Bearing friction at the OWSC hinge axis would also become more significant.

Wave Probes

The free surface profile is measured using four capacitance wave probes (Akamina). Two probe placement configurations are used in this thesis. Configuration A places all probes in the same line, so that the reflection algorithm in Eq. (1.15) can utilize all probes. Configuration B places two probes side by side to observe the presence of cross wave reflections in the tank. The probe spacing for each configuration follows the recommendations of Mansard and Funke [23]. In addition, the probes are placed 0.6 meters away from the piston according to [21], which suggests that probes are placed 2 to 3 water depths away from the piston to avoid measuring evanescent waves.

The probe positions in Table 4-3 are defined relative to the location where the scale model OWSC is to be deployed. The *y* coordinate is defined relative to the middle of the tank. A plan view of the probe positions for both configurations is shown in Figure 4-7.

Table 4-3: Wave probe locations

Probe #	Configuration A		Configuration B	
	x [mm]	y [mm]	x [mm]	y [mm]
1	-0.709	0	-0.944	0
2	-0.578	0	-0.734	0
3	-0.365	0	-0.399	0
4	0.257	0	-0.734	0.154

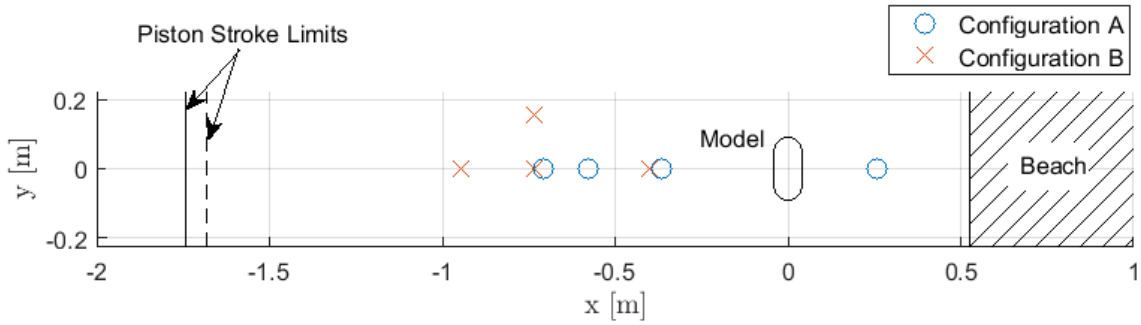

Figure 4-7: Plan view of the test section with wave probe locations, OWSC model location, piston stroke limits and the wave absorbing beach position

Wave absorbing beach

While the geometry of the nozzle and the honeycomb panels is reasonably effective at reducing wave reflections from the end of the tank, a gently sloping beach was added after the test section within the converging nozzle to further reduce reflections. The beach has a slope of 1:10 and is constructed from perforated stainless steel sheets to achieve a porosity roughly matching the recommendations in [45]. The performance of the beach in dissipating regular wave reflections is further discussed in Section 4.2.1.

4.2.1 Regular Wave Generation

As mentioned in Section 4.2, regular waves are produced by programming the controller with a sinusoidal cam profile along with two scaling parameters to adjust the amplitude and period of the profile. The stroke of the wavemaker S is related to the desired wave height H^* by the following relationship for piston-style wavemakers [21]:

$$\frac{H^*}{S} = 2\frac{\cosh(2kd)-1}{\sinh(2kd)+2kd} \tag{4.2}$$

The maximum stroke of the wavemaker is 6cm. This limits the range of wave heights that can be generated in the tank.

Regular wave parameters

To determine a suitable range of regular wave heights and periods that represent the wave conditions at the target location, a *regular wave histogram* is created from the original irregular wave histogram for the deployment location presented in Table 4-1. The regular wave histogram is created using the joint probability distribution model for irregular waves developed in [46]. Let the joint probability distribution corresponding to bin i in the irregular wave histogram be denoted $P_i(H,T)$, and let N_i be the hours of occurrence corresponding to the same bin. The hours of occurrence of regular waves with wave heights between H_1 and H_2 and wave periods between T_1 and T_2 is then given by

$$M_i = \int_{T_1}^{T_2}\int_{H_1}^{H_2} P_i(H,T)N_i dHdT \tag{4.3}$$

The total regular wave hours of occurrence per year can then be obtained by summing the contributions from each irregular wave histogram bin:

$$M_{tot} = \sum_i M_i \tag{4.4}$$

The regular wave histogram is obtained by evaluating Eq. (4.3) and (4.4) for every bin, and the resulting histogram is shown in Figure 4-8. Superposed on this figure are

- The regular wave breaking wave limit from [20] ($H_b = \frac{2\pi}{7k}\tanh(kd)$)
- the maximum wave height limit of the wavemaker, obtained from Eq. (4.2) with $S = 40\times(0.06m) = 2.4m$ (the maximum stroke length converted to full scale).

.

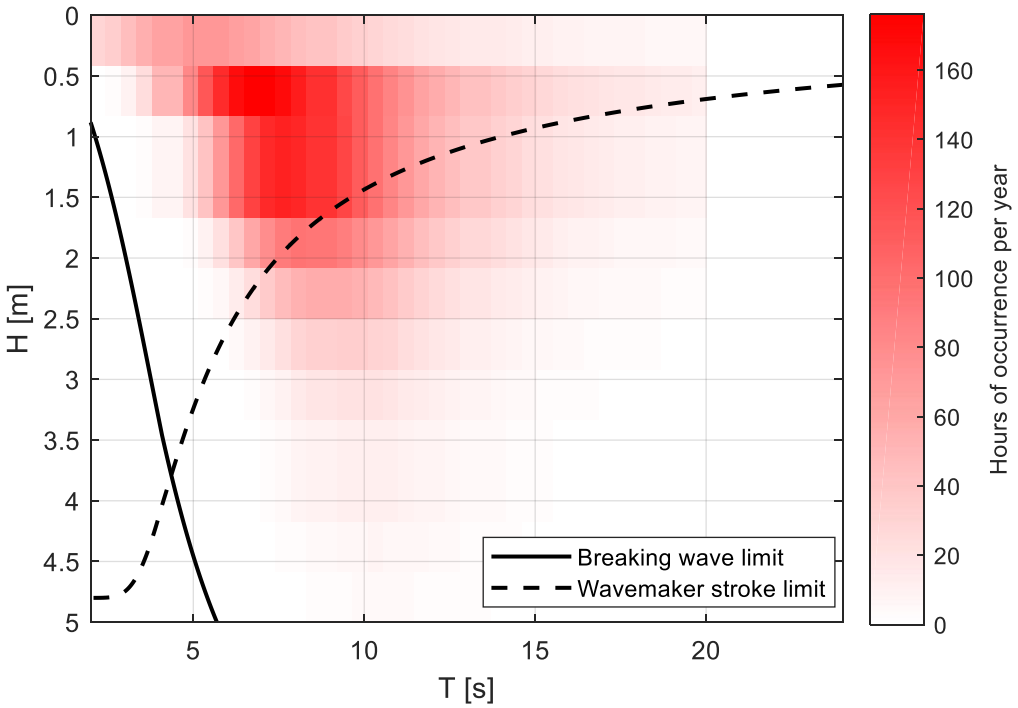

Figure 4-8: Regular wave histogram presented with breaking wave and wavemaker limits. Only histogram bins above the black curves can be generated in the wave tank.

Based on Figure 4-8, most regular wave occurrences lie on the intervals $T \in [4,16]s$ and $H \in [0,2]m$. The corresponding ranges for commanded wave height H^*, wave frequency ω^* and wave period T^* at 1:40 model scale (using Froude scaling laws) are

$$H^* \in [0, 0.05]m \tag{4.5}$$

$$\omega^* \in [2.5, 9.9]rad/s \tag{4.6}$$

$$T^* \in [0.6, 2.5]s \tag{4.7}$$

Note that not all wave heights can be tested at each frequency ω^* due to the wavemaker stroke limit.

Sample Results

Regular waves were generated without the OWSC model present to observe the quality of the resulting wave profiles. Four wave probes were positioned at the locations specified by Configuration A in Table 4-3. Sample results are presented in Figure 4-9. The variation in the measured wave amplitude at each probe indicates that the wave field is partially standing, and therefore the reflected wave amplitude from the end of the tank is significant. This is confirmed in Figure 4-10, which shows wave reflection coefficients for various wave frequencies before and after the wave absorbing beach was installed in the tank. While the beach overall reduces the reflection coefficients, they are still above 10% for all frequencies.

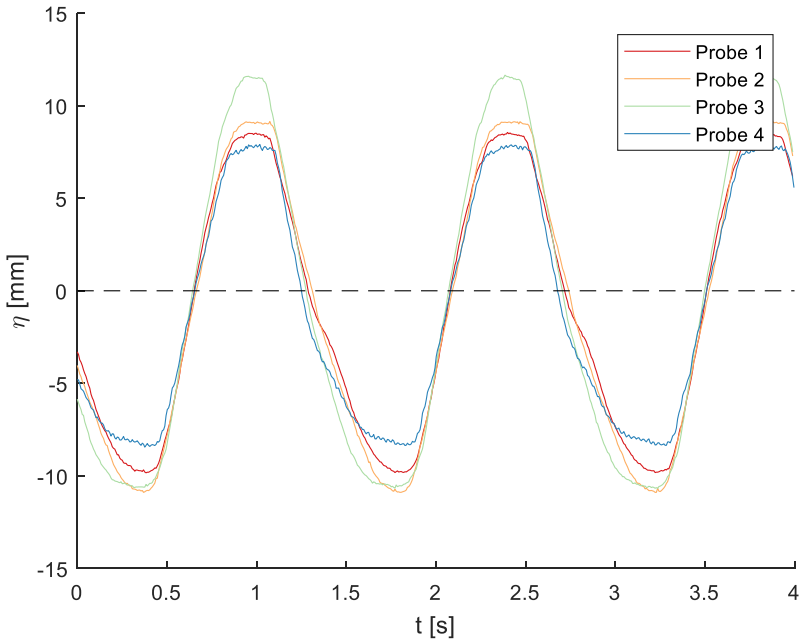

Figure 4-9: Sample wave probe measurements for a regular wave ($\omega^* = 4.40$ rad/s and $H^* = 0.02$ m). The phase of each measurement is shifted based upon the probe locations (given by configuration A) so that the shape of each measured wave can be directly compared.

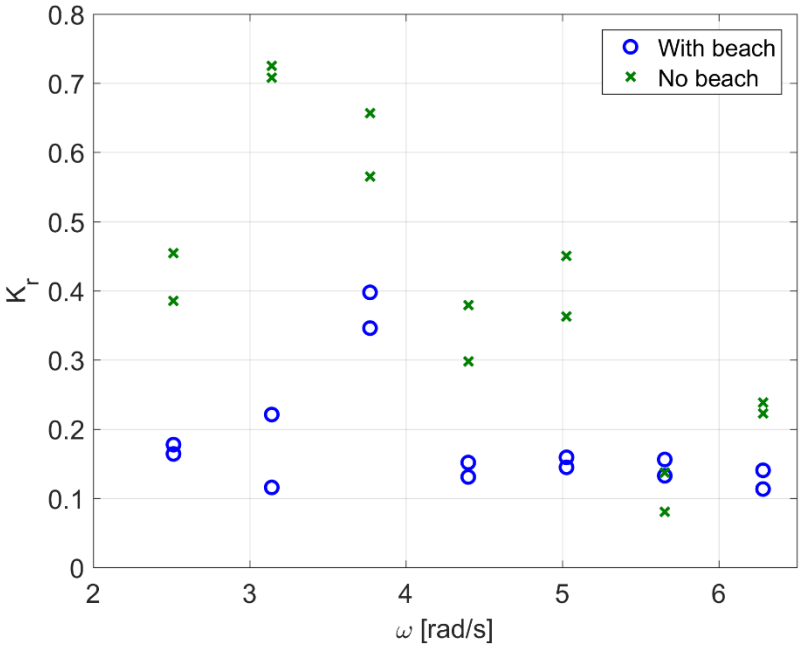

Figure 4-10: Wave reflection coefficients with and without the wave absorbing beach. For each wave frequency, reflection coefficients were obtained from two tests with different incident wave heights.

Note that the shape of the waves in Figure 4-9 are not strictly monochromatic due to errors in the wave generation process. This error can be better observed in the frequency domain. Figure 4-11 is obtained by calculating the amplitude spectrum of each probe measurement and applying the Mansard and Funke reflection algorithm to each spectral component to obtain incident and reflected wave amplitude spectra. Note that the peaks of the spectra occur at harmonics of the commanded wave frequency ω^*.

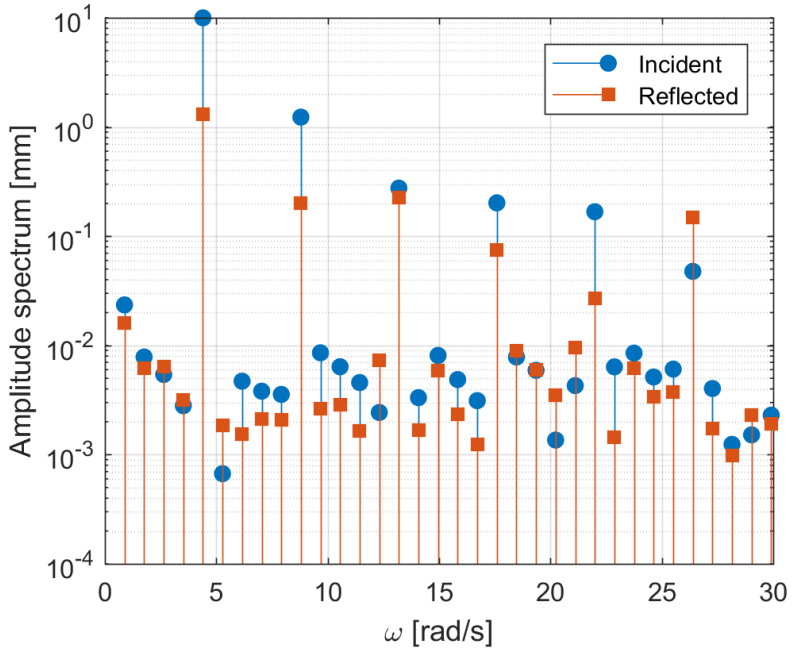

Figure 4-11: Sample incident and reflected wave amplitude spectra for regular waves ($\omega^* = 4.40$ rad/s and $H^* = 0.02$ m).

In summary, these sample results demonstrate that the experimental regular waves cannot simply be modelled by a single monochromatic wave. Instead, the wave system should be modelled using Eq. (1.17), which is equivalent to:

$$\eta(x,t) = \sum_{n=1}^{N} \mathrm{Re}\{A_I(\omega_n)\, e^{i(k_n x - \omega_n t)} + A_R(\omega_n)\, e^{i(-k_n x - \omega_n t)}\}$$

where A_I and A_R are the complex amplitude spectra for the incident and reflected wave systems. Since the amplitude spectra are negligible between harmonics of the commanded frequency, Eq. (1.12) is only evaluated at these harmonics ($\omega_n = n\omega^*$). This significantly reduces computation time when performing experimental/numerical model comparisons (as explained earlier in Section 3.3.2). Furthermore, the deviations in the wave system from the desired monochromatic profile can be quantified by the following three parameters:

- the relative error between the commanded and incident wave heights:

$$E_A = \frac{2\left|A_I\left(\omega^*\right)\right| - H^*}{H^*} \tag{4.8}$$

- the reflection coefficient at the commanded wave frequency:

$$K_R = \frac{\left|A_R(\omega^*)\right|}{\left|A_I(\omega^*)\right|} \tag{4.9}$$

- the total harmonic distortion (THD) of the incident wave profile:

$$\mathrm{THD} = \frac{\sqrt{\sum_{n=2}^{\infty}\left|A_I(n\omega^*)\right|^2}}{\left|A_I(\omega^*)\right|} \tag{4.10}$$

These three parameters are tabulated for each test conducted with the OWSC model in Chapter 5.

4.2.2 Irregular Wave Generation

The cam profile for irregular waves is generated using:

$$x = \sum_i X(\omega_i)\cos(\omega_i t + \varphi_i) \tag{4.11}$$

$X(\omega)$ is obtained from the Pierson-Moskowitz model $S_{PM}(\omega)$ given in Eq. (1.10) by scaling the amplitude of each spectral component by the wave height to wavemaker stroke ratio from Eq. (4.2) :

$$X(\omega) = \sqrt{2S_{PM}(\omega)\Delta\omega}\,\frac{1}{2}\frac{\sinh(2kd)+2kd}{\cosh(2kd)-1} \tag{4.12}$$

The phases φ_i are randomly generated on the interval $[0, 2\pi]$.

A problem with this approach is that the linear actuator controller has limited memory for allocation of cam profile target points. Only about two minutes of time series data for Eq. (4.11) can be uploaded to the controller while ensuring that there is enough resolution in the discrete cam profile to properly represent the original time series. Therefore, to test for longer time periods, the irregular cam profile must be repeated, which is not truly representative of the Pierson-Moskowitz spectrum describing real ocean sea states.

An additional complication with generating irregular waves is due to the wavemaker stroke limit. Section 4.2.1 demonstrated that the range of regular wave heights that can be experimentally produced is limited by wavemaker stroke. This limit is even more constraining for irregular waves because any irregular time series will occasionally have large amplitude crests (rogue waves) which will require large motions of the wavemaker to correctly reproduce.

Due to these complications only two irregular wave profiles are considered in this thesis. The first is a PM spectrum with a significant wave height of 0.015m and a peak period of 1.5s, corresponding to 0.6m and 9.5s at full scale. The second irregular wave profile is produced simply by scaling the resulting cam profile of the first irregular wave profile by 1.4 to utilize the full stroke range of the wavemaker. The bins for both spectra within the deployment site wave histogram are shown in Table 4-1. Sample results obtained for the first spectrum using the Mansard and Funke reflection algorithm are shown in Figure 4-12.

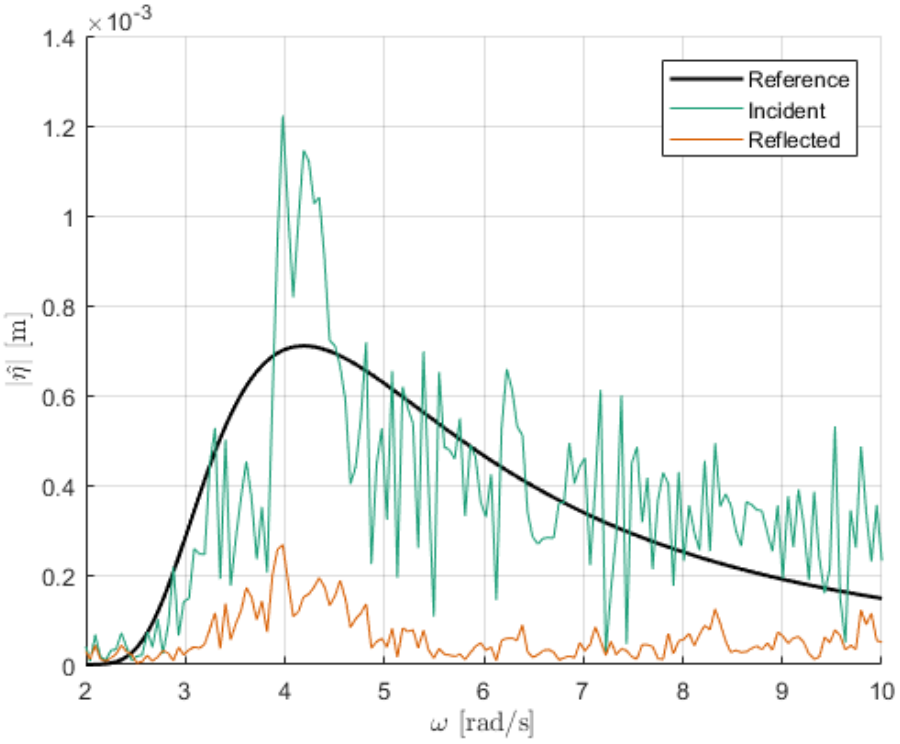

Figure 4-12: Sample incident and reflected wave spectra for irregular waves. The reference spectrum is a Pierson-Moskowitz with $H_s = 0.015$m and $T_p = 1.5$s

4.3 Wave Reflections with Experimental Models

When deploying experimental models in wave tanks, there are two wave reflection problems that arise. The first problem is due to waves reflecting off the end of the wave tank – a significant problem for the small scale UVic wave tank discussed earlier in Section 4.2. The second problem arises from radiated and scattered waves produced by the physical model being re-reflected from the wavemaker and sent back towards the model. Both problems create uncertainty regarding the actual wave profile experienced by the OWSC model. Some wave tanks minimize these uncertainties by implementing active wave absorption techniques. Otherwise, in the absence of active wave absorption, the effects of these reflected waves on measured data must be identified.

The first problem is conventionally resolved by measuring the wave profile at the model location without the model present. This allows the total wave amplitude, including both incident and reflected components, to be determined at the model location without interference from radiated and scattered waves produced by the model, provided that the wave tank is calibrated and repeatable. The second problem is conventionally resolved by rejecting data after the re-reflected waves begin to impact the dynamics of the model [47], [48]. Normally wave tanks are long so that a significant amount of data can be obtained before the re-reflections reach the model.

Unfortunately, none of these techniques can be applied to the experimental work in this dissertation due to the short length of the tank. Wave reflections from the end of the tank are significant and cannot be neglected, and wave measurements taken without the model present are an ill representation of the wave field with the model deployed due to re-reflections of the radiated and scattered wave fields. These re-reflections reach the model within seconds after the test begins due to the short length of the tank, and therefore rejecting data is not an option. Ultimately this means that the wave system must be treated as a partially standing wave, and a reflection algorithm that identifies the incident and reflected wave components *with* the model present must be developed.

The following sections discuss the development of a modified reflection algorithm which accounts for the radiated and scattered wave fields produced by the OWSC model. Section 4.3.1 derives numerical estimates of the radiated and scattered wave elevations produced by the OWSC model, which are then used in Section 4.3.2 to develop the reflection algorithm.

4.3.1 Numerical Modelling of the Free Surface

The amplitudes of the radiated waves and diffracted waves (sum of both incident and scattered waves) can be obtained in the domain around the OWSC model using WAMIT coefficients with wall effects. Sample free surface results for the diffracted and radiated wave fields are shown in Figure 4-13 and Figure 4-14. The accuracy of these WAMIT predictions has been previously investigated by McNatt *et.al.* [49] for a flap in regular waves, with frequencies between 0.8 and 1.25 Hz and wave heights up to 6cm. The WAMIT results agreed well with the experimental observations by McNatt *et.al.*, although WAMIT was observed to over predict the radiated wave amplitudes [49].

The modified wave reflection algorithm requires the following complex values at each wave probe location in Table 4-3, as a function of regular wave frequency:

- $\hat{\eta}_{D+}$: the diffracted wave field for waves propagating in the positive *x* direction, normalized by incident wave amplitude
- $\hat{\eta}_{D-}$: the diffracted wave field for waves propagating in the negative *x* direction, normalized by reflected wave amplitude
- $\hat{\eta}_{R}$: the radiated wave field amplitude, normalized by the OWSC pitch motion amplitude

Sample results for probe 3 in Configuration A are presented in Figure 4-15. Note that there is asymmetry between $\hat{\eta}_{D+}$ and $\hat{\eta}_{D-}$ due to the change in the diffracted wave amplitude before and after the wave propagates around the OWSC model, as shown in Figure 4-14.

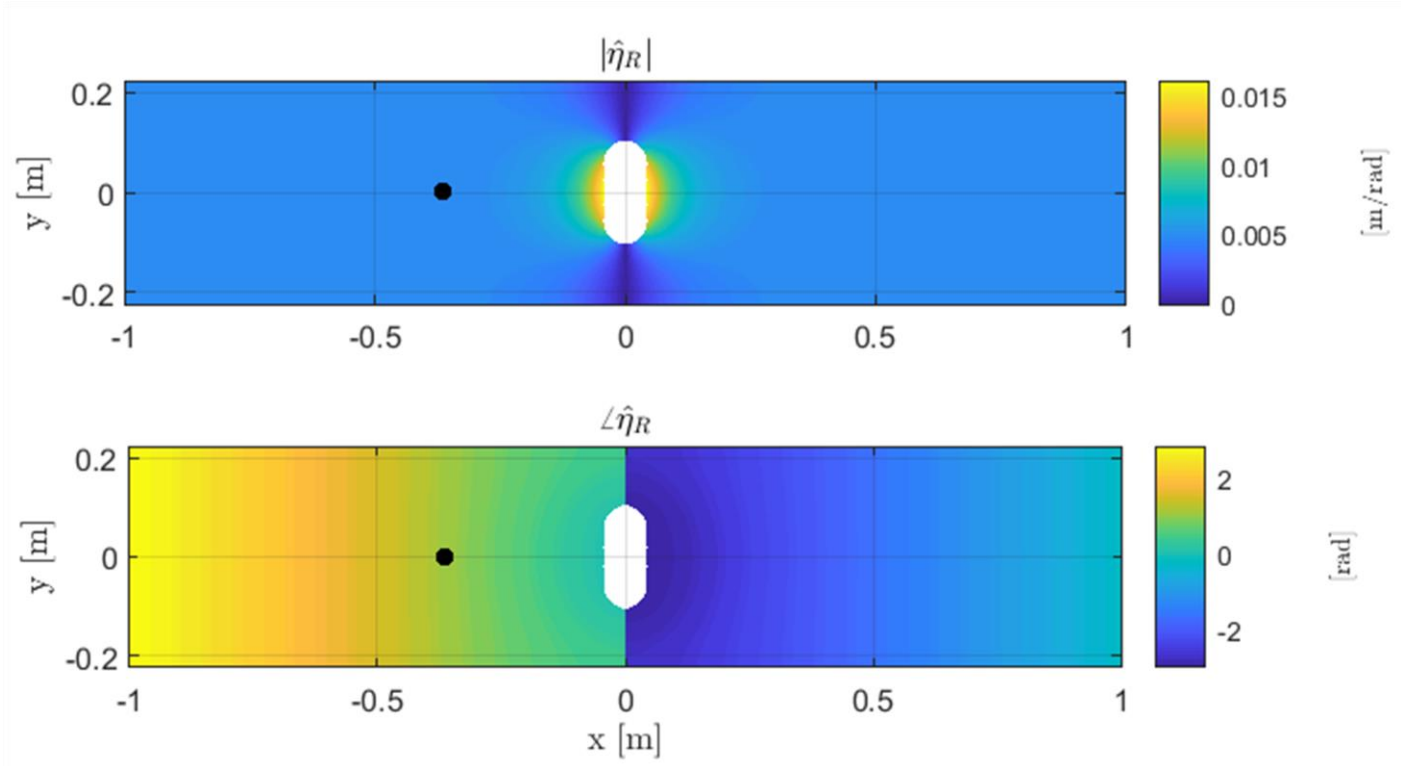

Figure 4-13: Complex amplitude of the free surface for the radiation problem with $\omega = 3.77$ rad/s, normalized by the OWSC pitch amplitude. The top figure shows the modulus and the bottom figure plots the argument. The location of probe 3 from Configuration A is marked by the black circle.

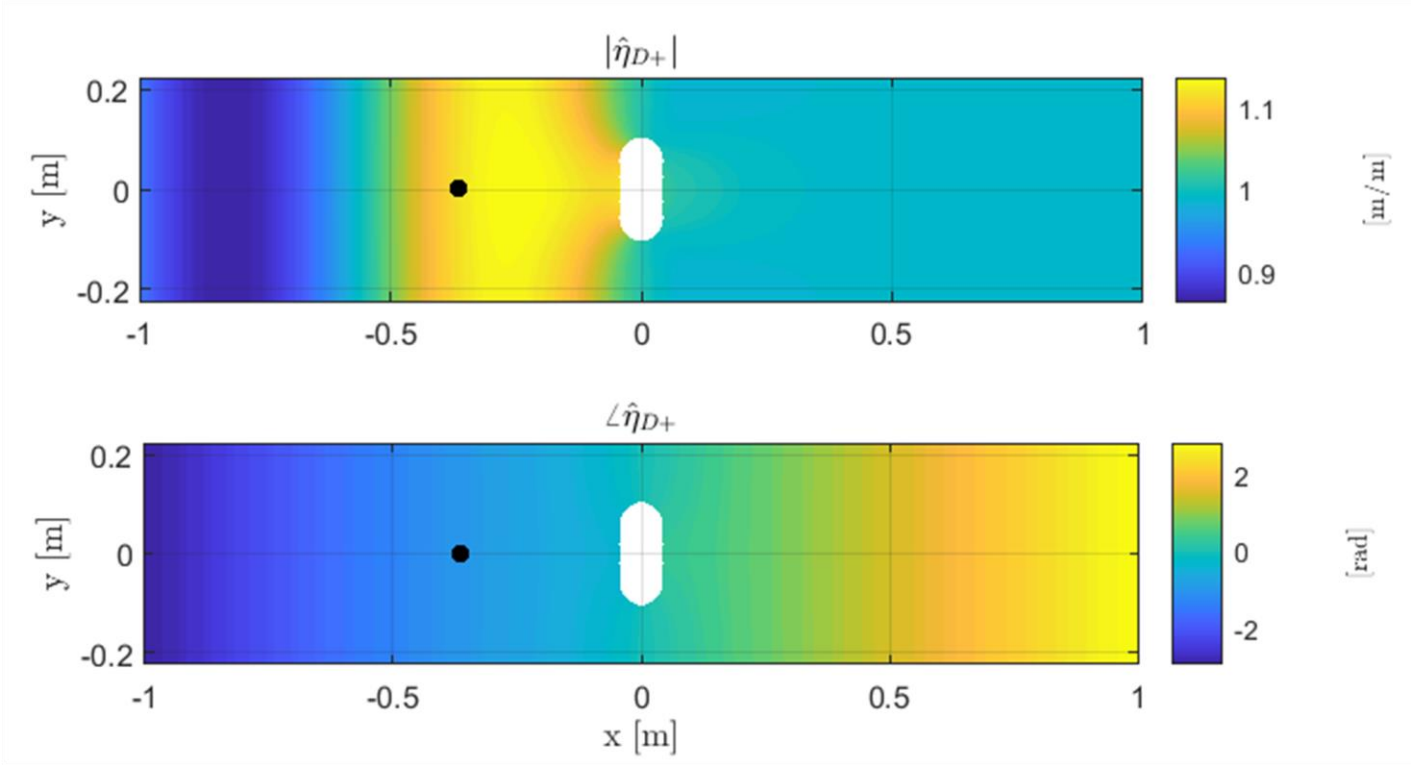

Figure 4-14: Complex amplitude of the free surface for the diffraction problem with $\omega = 3.77$ rad/s, normalized by the incident wave amplitude. The top figure shows the modulus and the bottom figure plots the argument. These results are for waves propagating in the positive *x* direction; results for waves propagating in the negative direction are symmetrical about *x*=0. The location of probe 3 from Configuration A is marked by the black circle.

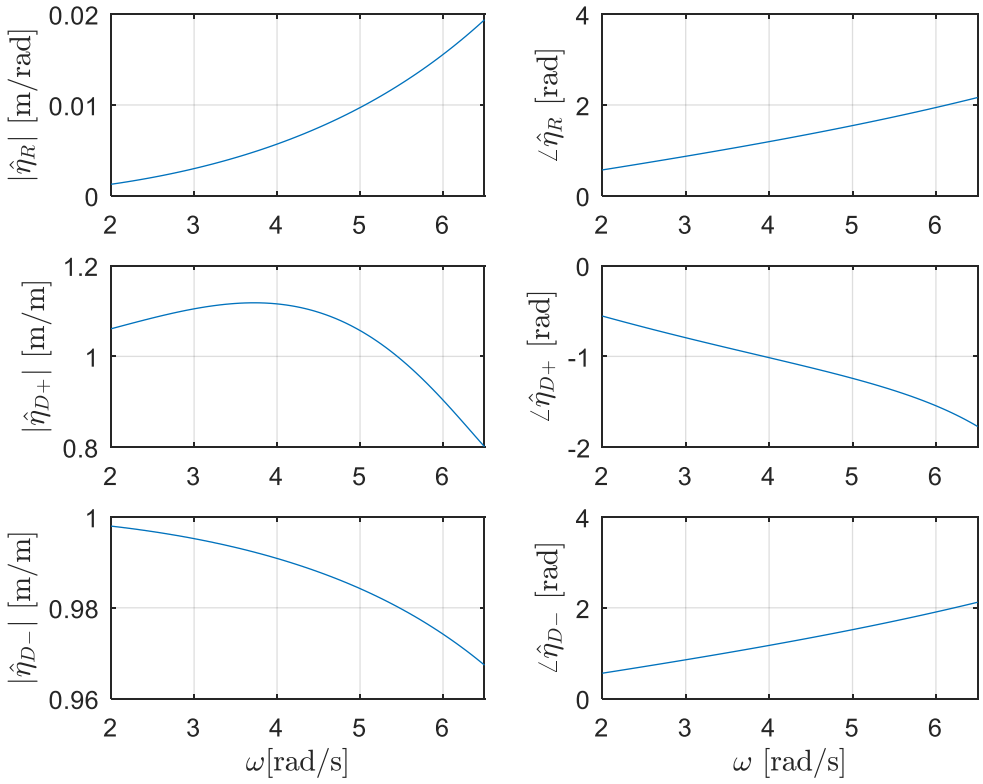

Figure 4-15: Sample normalized amplitude spectra for the radiated and diffracted waves at probe 3 for Configuration A.

With the normalized complex amplitudes of the diffracted and radiated wave fields at each probe, the numerical free surface estimate at a given probe *p* then becomes

$$\hat{\eta}_n^{(p)} = \hat{\eta}_{D+,n}^{(p)} A_{I,n} + \hat{\eta}_{D-,n}^{(p)} A_{R,n} + \hat{\eta}_{R,n}^{(p)} \hat{\theta}_n + \varepsilon_n^{(p)} \tag{4.13}$$

Here, $\hat{\theta}_n$ is the n^{th} component of the Fourier transform of flap pitch motion, measured using a rotary position sensor (see Chapter 5), and $\hat{\eta}_n^{(p)}$ is the n^{th} component of the Fourier transform of the free surface measured by probe *p*. The wave amplitudes $\hat{\eta}_{R,n}^{(p)}$, $\hat{\eta}_{D+,n}^{(p)}$ and $\hat{\eta}_{D-,n}^{(p)}$ are obtained from WAMIT for frequency ω_n; $\hat{\eta}_R^{(p)}$ is the radiated wave amplitude spectrum at probe *p* due to unit amplitude pitch motion, while $\hat{\eta}_{D+}^{(p)}$ and $\hat{\eta}_{D-}^{(p)}$ are the diffracted wave amplitude spectra at probe *p* resulting from unit amplitude incident waves propagating in the positive and negative *x*

directions, respectively. The residual $\varepsilon_n^{(p)}$ accounts for error between the numerical estimates from WAMIT and the experimental free surface profile.

4.3.2 Modified Reflection Analysis

Using the same approach as Mansard and Funke, the incident and reflected wave spectra can be estimated from the measurements of N_p wave probes by minimizing the sum of the squares of the error terms $\varepsilon^{(p)}$:

$$E = \sum_{p=1}^{N_p} \left(\varepsilon_n^{(p)} \right)^2 = \sum_{p=1}^{N_p} \left(\hat{\eta}_{D+,n}^{(p)} A_{I,n} + \hat{\eta}_{D-,n}^{(p)} A_{R,n} + \hat{\eta}_{R,n}^{(p)} \hat{\theta}_n - \hat{\eta}_n^{(p)} \right)^2 \tag{4.14}$$

The minimum is located where the first derivatives of (4.14) equal zero, so that

$$\frac{\partial E}{\partial A_{I,n}} = 2 \sum_{p=1}^{N_p} \hat{\eta}_{D+,n}^{(p)} \left(\hat{\eta}_{D+,n}^{(p)} A_{I,n} + \hat{\eta}_{D-,n}^{(p)} A_{R,n} + \hat{\eta}_{R,n}^{(p)} \hat{\theta}_n - \hat{\eta}_n^{(p)} \right) = 0 \tag{4.15}$$

$$\frac{\partial E}{\partial A_{R,n}} = 2 \sum_{p=1}^{N_p} \hat{\eta}_{D-,n}^{(p)} \left(\hat{\eta}_{D+,n}^{(p)} A_{I,n} + \hat{\eta}_{D-,n}^{(p)} A_{R,n} + \hat{\eta}_{R,n}^{(p)} \hat{\theta}_n - \hat{\eta}_n^{(p)} \right) = 0 \tag{4.16}$$

The amplitude spectra A_I and A_R can then be obtained by solving

$$\begin{bmatrix} \sum_{p=1}^{N_p} \left(\hat{\eta}_{D+,n}^{(p)} \right)^2 & \sum_{p=1}^{N_p} \hat{\eta}_{D+,n}^{(p)} \hat{\eta}_{D-,n}^{(p)} \\ \sum_{p=1}^{N_p} \hat{\eta}_{D+,n}^{(p)} \hat{\eta}_{D-,n}^{(p)} & \sum_{p=1}^{N_p} \left(\hat{\eta}_{D-,n}^{(p)} \right)^2 \end{bmatrix} \begin{bmatrix} A_{I,n} \\ A_{R,n} \end{bmatrix} = \begin{bmatrix} \sum_{p=1}^{N_p} \hat{\eta}_{D+,n}^{(p)} \left(\hat{\eta}_n^{(p)} - \hat{\eta}_{R,n}^{(p)} \hat{\theta}_n \right) \\ \sum_{p=1}^{N_p} \hat{\eta}_{D-,n}^{(p)} \left(\hat{\eta}_n^{(p)} - \hat{\eta}_{R,n}^{(p)} \hat{\theta}_n \right) \end{bmatrix} \tag{4.17}$$

for each frequency component *n* of the amplitude spectra. The incident and reflected amplitude spectra are then used to evaluate the free surface elevation given by Eq. (1.17) and the associated fluid properties given by Eq. (1.28) to (1.30). The candidate models summarized in Table 3-1 can then be evaluated using the same wave system that occurred in the tank.

Error in the wave reflection algorithm is quantified by the root-mean-square of the residuals $\varepsilon_n^{(p)}$ for each wave probe *p* and for each frequency component *n* of the amplitude spectra. The resulting error is normalized by the amplitude of the incident wave at the commanded wave frequency:

$$E_{res} = \frac{\sqrt{\sum_{p=1}^{4}\sum_{n=1}^{\infty}\left|\varepsilon_n^{(p)}\right|^2}}{\left|A_I(\omega^*)\right|} \tag{4.18}$$

This error is used in Chapter 5 to identify test cases where large differences between experimental/numerical model predictions may be attributed to inaccuracies in the wave reflection algorithm.

4.4 Chapter Summary

This chapter introduced a location of interest for future deployment of OWSCs, and presented irregular and regular wave histograms for that location. These histograms were then used to determine a suitable range of parameters for regular and irregular wave tests performed in the small-scale wave tank at UVic. It was found that the short stroke length of the wavemaker limits the range of regular wave heights which can be generated in the wave tank. Irregular wave tests are further constrained by the limited stroke length, and are also difficult to correctly reproduce due to limitations of the wavemaker's linear actuator controller, therefore most of the experimental work from hereon is performed with regular waves.

Sample regular and irregular wave measurements showed that wave reflections from the end of the tank are significant, despite the addition of a passive wave absorbing beach. Because of the short length of the tank, these reflections cannot be accounted for using common techniques in literature. Therefore, a modified reflection algorithm was developed to identify the incident and reflected wave components while accounting for radiated and scattered waves produced by the presence of the experimental model. When comparing experimental/numerical results in Chapter 5, the experimental wave system will be modelled as a partially standing wave, using the incident and reflected wave amplitudes obtained from the modified reflection algorithm.

Chapter 5: Scale Model OWSC Experiments

In this chapter, outputs from the candidate numerical models developed in Chapters 2 and 3, and described in Section 3.1, are compared with experimental observations collected in the small-scale wave tank for a series of different scenarios. Each scenario aims to isolate a hydrodynamic moment to afford direct evaluation of the various layers (e.g. nonlinear model extensions) used in the candidate numerical models. First, OWSC pitch decay tests are performed; their sole purpose is to estimate the drag coefficients to be used in the numerical models. Fixed tests are then performed, where the OWSC is fixed in the vertical position ($\theta = 0$) and the hydrodynamic moment acting on the model is measured, allowing the wave excitation moments to be measured without radiation effects present. Unconstrained pitch motion tests in regular waves are then performed to consider the full FSI problem, including excitation, free surface and radiation effects. Lastly, irregular wave tests are performed to compare experimental observations with numerical predictions in a typical ocean sea state.

Initial ranges for wave height and frequency for the regular wave tests are selected based upon the ranges defined in Chapter 4 (Eq. (4.5) to (4.7)), which were established based upon the environmental conditions at the target deployment site. By observing the numerical predictions from Section 3.5, there is little difference between the candidate model predictions for wave frequencies greater than 6.5 rad/s, therefore the range of experimental wave frequencies can be limited to

$$\omega^* \in [2.5, 6.5] rad/s \tag{5.1}$$

$$T^* \in [1.0, 2.5] s \tag{5.2}$$

Furthermore, the stroke size of the wavemaker limits the maximum wave height that can be generated, as shown in Figure 4-8. Based on this figure, the wavemaker can generate wave heights up to 0.03m for the majority of the range of frequencies given by Eq. (5.1):

$$H^* \in [0, 0.03] m \tag{5.3}$$

Note that the maximum wave height from Eq. (5.3), is much lower than the largest wave height simulated in Section 3.5 (0.05m), where the largest deviations between candidate model predictions were observed. Therefore, for the range of regular wave conditions producible by the wave tank, the divergence between candidate model predictions may be insignificant.

A summary of each test is provided here:

- Decay tests: in still water, the flap is held at a fixed angle then released to isolate the radiation and viscous drag loads. The pitch motion of the flap is measured and used to obtain a drag coefficient for the OWSC model.
- Fixed tests: the flap is fixed at zero pitch angle in regular waves to isolate the wave excitation loads (Froude-Krylov, scattering and viscous drag) from the radiation loads. The total wave excitation moment about the flap hinge is measured using a load cell. These measurements are then compared to candidate model predictions obtained using the drag coefficient from the decay tests.
- Regular wave tests: the flap is unconstrained and subjected to regular waves, allowing the full FSI problem to be modelled. The pitch motion of the flap is measured and compared to candidate model predictions obtained using the drag coefficient from the decay tests.
- Irregular wave tests: the flap is unconstrained and subjected to irregular waves to observe the OWSC dynamics in an approximately realistic ocean sea state. The pitch motion of the flap is measured and compared to candidate model predictions obtained using the drag coefficient from the decay tests.

A schematic of the experimental setup is shown in Figure 5-1. The figure shows the experimental arrangement for fixed flap tests. The moment about the hinge axis of the OWSC is measured using

a load cell, which measures the horizontal force acting on a rod mounted vertically from the top edge of the OWSC model. A clevis joint between the load cell and rod ensures that no bending moments are applied to the load cell. For the other three test scenarios, the load cell, rod and clevis joint are removed so that the model is unconstrained. A non-contact rotary position sensor (Novotechnik RFC4800) then measures the pitch angle of the model.

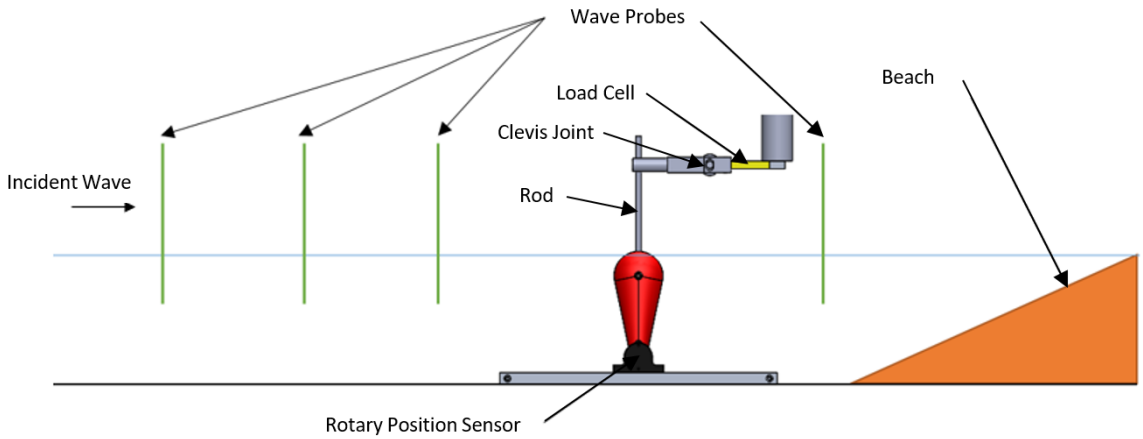

Figure 5-1: Experimental arrangement for the fixed flap tests.

5.1 Decay Tests

Decay tests are performed by displacing the flap, in still water, to an initial pitch angle and releasing the flap. The resulting decay in pitch motion is then measured using the rotary position sensor and compared to the numerical model to estimate the drag coefficient of the device. Only models 1 and 2 are compared to the experimental results; since there are no incident waves, models 2 and 3 are equivalent. To clarify, the differences between models 2 and 3 are:

- Model 2 computes the Froude-Krylov moment by integrating the undisturbed hydrodynamic fluid pressure beneath the still waterline and about the vertical position (mean position) of the OWSC. In contrast, Model 3 integrates the same fluid pressure about the actual wetted surface, accounting for the incident wave profile and OWSC position.

- Model 2 computes the buoyancy moment by integrating hydrostatic fluid pressure below the still waterline. In contrast, Model 3 computes the buoyancy moment by integrating over the actual wetted surface, accounting for the incident wave profile. Model 3 also utilizes the Wheeler stretching algorithms given by Eq. (1.28) to (1.30).

In the case where there are no incident waves, i.e. for decay tests, then there is no Froude-Krylov moment and the buoyancy moments for Models 2 and 3 become equivalent. There is therefore no difference between Models 2 and 3 for decay tests. Furthermore, the only differences between Models 1 and 2 are the methods for computing the drag moment: Model 1 uses the strip approach (Eq. (3.25)) while Model 2 uses the panel approach (Eq. (3.24)).

An optimization procedure is used to find the drag coefficient that best matches Models 1 and 2 to the experimental results. The optimization is formulated as a least-squares minimization between the experimental and numerical pitch motion time series:

$$\min_{C_d} \quad \sum_{n=1}^{N} \left[\theta_m(nt_s) - \theta_{num}(nt_s) \right]^2 \tag{5.4}$$

where θ_m is the measured pitch motion and θ_{num} is the numerical model prediction using a drag coefficient of C_d. The left column of Figure 5-2 shows the comparison between experimental and numerical results after the optimization procedure, which resulted in a drag coefficient of 1.4 for both models. Note however that the decay frequencies of the experimental and numerical results are different, therefore a correction to the OWSC added inertia A^* was added to the WAMIT based prediction A_∞ to adjust the decay frequency of the numerical results and obtain a better match with the experimental data, for which $\omega_{decay} = 3.04$ rad/s. The modified equation of motion for Models 1 and 2 is:

$$(I + A_\infty + A^*)\ddot{\theta} + \int_0^t k(t-\tau)\dot{\theta}(\tau)d\tau + C(\theta)\theta = M_e(t) + M_d(t) \tag{5.5}$$

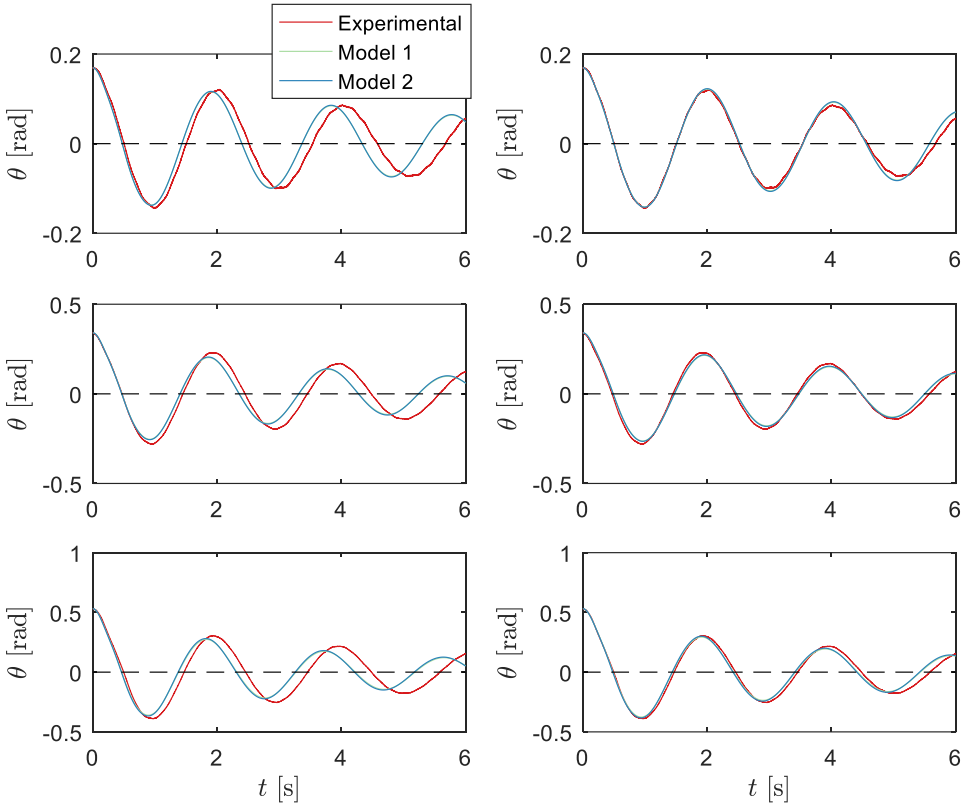

Figure 5-2: Decay tests results used for estimating drag coefficients. Experimental results collected with three different initial pitch angles are compared with models 1 and 2 with $C_d = 1.4$. The numerical results in the right column were obtained with a correction to infinite added inertia to match the damped frequency of the experimental results, while the results in the left column were obtained without the correction.

Table 5-1 lists the original added inertia obtained from WAMIT in Chapter 2, along with the corrected added inertia used to match the decay frequencies of the experimental and numerical pitch motions. The corrected added inertia coefficient is obtained by manually adjusting it until the numerical model prediction (using $C_d = 1.4$) matches the experimental results.

Table 5-1: Infinite and corrected added inertia coefficients for the decay tests.

A_∞	A^*
$0.0155\,kgm^2$	$0.0055\,kgm^2$

The difference in decay frequency possibly indicates that the added inertia upon the model deviates from potential flow theory due to viscous effects. In this case, the correction to added inertia may be frequency dependent, and regular wave tests are better suited for investigating this correction, since decay tests only provide results at the damped natural frequency of the OWSC. Therefore, this correction to added inertia is further investigated in Section 5.3.1 when analyzing regular wave test results.

5.2 Fixed Flap Tests

Fixed flap tests are used for two purposes: to demonstrate the utility of the modified wave reflection algorithm, and to evaluate the different algorithms for the wave excitation moments (including viscous drag) used in Models 1, 2 and 3. The governing equations for each numerical model are given in Table 3-1. For these tests, the model is fixed in the vertical orientation, and the total moment about the hinge axis is measured using the load cell, as shown in Figure 5-1. The total excitation moment for each numerical model is summarized in Table 5-2. Note that Eq. (3.9) also evaluates the buoyancy moment, however since the OWSC is fixed vertically the net buoyancy moment is zero.

For each test, the wavemaker is commanded to produce a regular wave at frequencies in the range defined by Eq. (5.1) and with a nominal wave height of 1 or 2 cm. The resulting experimental waves are modelled as partially standing wave profile, allowing the free surface at the model location to be estimated using Eq. (1.17). Amplitude spectra for the incident and reflected waves are calculated using the modified reflection algorithm described in Section 4.3. The wave probes for each test are arranged using Configuration A given in Table 4-3.

Table 5-2: Summary of candidate model wave excitation moments for fixed tests

Model 1	Total moment: $\sum M = M_e(t) + M_d(t)$ $M_e(t)$ is linear, given by Eq. (2.11) $M_d(t)$ is given by Eq. (3.25)
Model 2	Total moment: $\sum M = M_e(t) + M_d(t)$ $M_e(t)$ is linear, given by Eq. (2.11) $M_d(t)$ is given by Eq. (3.24)
Model 3	Total moment: $\sum M = M_{FK}(t) + M_S(t) + M_d(t)$ $M_{FK}(t)$ is nonlinear, given by Eq. (3.9) $M_S(t)$ is linear, given by Eq. (3.5) $M_d(t)$ given by Eq. (3.24)

The repeatability of the experimental wave profiles are checked by evaluating the error metrics given in Eq. (4.8) to (4.10) for 10 windows over the length of the measured time series. The length of each window is equal to the period of the commanded wave, and the initial window is 60s after wave generation begins to avoid transient effects. The mean and standard deviation of the windowed results for Eq. (4.8) to (4.10) are summarized in Table 5-3. Note that the standard deviations for each parameter are very low, indicating that the experimental wave profiles are very repeatable. Therefore, the incident and reflected wave amplitude spectra for each test are recalculated using a larger window containing 10 wave periods, to obtain a more accurate description of the experimental wave systems.

The analysis of fixed flap test results is divided into two sections. The first section demonstrates the utility of the modified reflection algorithm by comparing numerical results obtained using

Table 5-3: Repeatability of the experimental wave profiles for fixed flap tests. Cells representing error are shaded based on their magnitude. Signed cells are shaded blue-orange, and unsigned cells are shaded red.

Test ID	Desired Wave		Mean			Standard Deviation x 10^3		
	ω^*	H^*	E_A	K_R	THD	E_A	K_R	THD
	rad/s	m	-	-	-	-	-	-
F01	2.513	0.010	-0.163	0.094	0.076	0.939	1.154	0.724
F02	3.142	0.010	-0.199	0.195	0.077	0.917	1.279	3.338
F03	3.770	0.010	0.185	0.382	0.161	1.147	0.680	0.718
F04	4.398	0.010	-0.091	0.159	0.096	0.509	0.468	0.692
F05	5.027	0.010	-0.085	0.189	0.076	0.480	0.522	0.711
F06	5.655	0.010	0.041	0.169	0.121	0.657	0.319	0.753
F07	6.283	0.010	0.080	0.086	0.118	0.734	0.383	0.837
F08	2.513	0.020	-0.192	0.113	0.113	0.926	0.944	1.191
F09	3.142	0.020	-0.151	0.169	0.124	0.809	2.406	1.070
F10	3.770	0.020	0.083	0.325	0.250	0.482	0.597	0.772
F11	4.398	0.020	-0.120	0.143	0.152	0.551	0.790	0.814
F12	5.027	0.020	-0.118	0.199	0.096	0.273	0.660	1.345
F13	5.655	0.020	0.024	0.182	0.200	0.503	0.654	1.062
F14	6.283	0.020	0.030	0.085	0.171	0.446	0.566	1.412

Model 1 for three different wave reflection algorithms of increasing complexity that culminate in the modified reflection algorithm introduced in Section 4.3. The second section compares numerical predictions for Models 1 to 3 obtained using the measured partially standing wave fields obtained from the modified reflection algorithm.

5.2.1 Demonstration of the modified reflection algorithm

The modified reflection algorithm was previously used to calculate the reflection coefficient when assessing the repeatability of the generated waves when the OWSC is fixed vertically in the tank (see Table 5-3). This section now assesses the performance of the modified reflection algorithm by comparing it with two conventional approaches for identifying wave reflections. Since the model is present, the metric for comparing each approach is the overall excitation moment on the OWSC – the assumption being that any method that performs well will correctly

identify the incident and reflected waves and the subsequent moment calculations will better approximate the measured excitation moment.

For this analysis, Model 1 is simulated using the estimated wave profile at the model location for three different cases:

- Case 1: the OWSC model is removed from the tank and the free surface at the model location is measured. The resulting measurement is treated as the incident wave profile, and wave reflections are neglected.
- Case 2: the Mansard and Funke wave reflection algorithm is applied using wave probe measurements obtained while the OWSC model is not deployed in the tank. The free surface at the model location is obtained using Eq. (1.17)
- Case 3: the modified wave reflection algorithm is applied using wave probe measurements obtained while the OWSC model is deployed in the tank. The free surface at the model location is obtained using Eq. (1.17)

The resulting Model 1 based numerical prediction for the total wave excitation moment is compared with the measured excitation moment upon the model using the load cell in Figure 5-1. Error between the experimental and numerical model results for excitation moment is evaluated using the root-mean-square (RMS) of the difference between the experimental and numerical time series. The RMS error is normalized by the amplitude of the fundamental harmonic of the experimental measurement:

$$E_{rel} = \frac{\sqrt{\sum_{n=0}^{N-1}\left(M_m(nt_s) - M_{num}(nt_s)\right)^2}}{N\,|\hat{M}_m(\omega^*)|} \tag{5.6}$$

The resulting relative errors for each case are presented in Table 5-4. The large relative errors for test F02 are attributed to noise in the measurement from the load cell. This measurement noise is most significant when the commanded wavemaker motion frequency is around 3.14 rad/s. The source of the noise is believed to be the wavemaker, as there appears to be cyclical variations in the magnitude of the noise which appear to correspond with the wavemaker piston motion. This is

illustrated in Figure 5-3, which compares a highpass filtered sample measurement from the load cell with the position of the wavemaker piston.

Table 5-4: Error in the numerical wave excitation moment for three cases, where each case uses a different method for estimating the wave profile at the model location. Results are obtained using Model 1, with and without lowpass filtering of the measured moment signal. Cells are shaded red based on their magnitude.

Test ID	E_{rel} (unfiltered)			E_{rel} (filtered)		
	Case 1	Case 2	Case 3	Case 1	Case 2	Case 3
F01	0.368	0.250	0.213	0.329	0.190	0.138
F02	0.455	0.457	0.447	0.257	0.260	0.243
F03	0.519	0.291	0.138	0.517	0.287	0.131
F04	0.307	0.180	0.171	0.299	0.166	0.156
F05	0.384	0.320	0.157	0.373	0.306	0.127
F06	0.287	0.242	0.176	0.28	0.233	0.163
F07	0.254	0.175	0.137	0.248	0.167	0.127
F08	0.258	0.126	0.193	0.247	0.101	0.177
F09	0.455	0.384	0.353	0.365	0.270	0.225
F10	0.503	0.331	0.202	0.501	0.329	0.198
F11	0.340	0.184	0.187	0.337	0.178	0.181
F12	0.402	0.239	0.252	0.398	0.232	0.246
F13	0.343	0.284	0.306	0.341	0.281	0.304
F14	0.260	0.199	0.216	0.258	0.197	0.213

To better compare experimental and numerical results, noise in the load cell measurements due to the wavemaker is removed by lowpass filtering each measurement with a cut-off frequency equal to 6 times the commanded wave frequency ($\omega_{cutoff} = 6\omega^*$). A sample comparison between raw and lowpass filtered moment measurements from the load cell is also presented in Figure 5-3.

The filtered measurements for the total wave excitation moment are then compared once again with numerical results for cases 1 to 3. These results are presented in Table 5-4. Ultimately case 3, using the modified reflection algorithm, provides the best agreement between numerical and experimental results, however the amount of improvement varies between tests. Sample results are

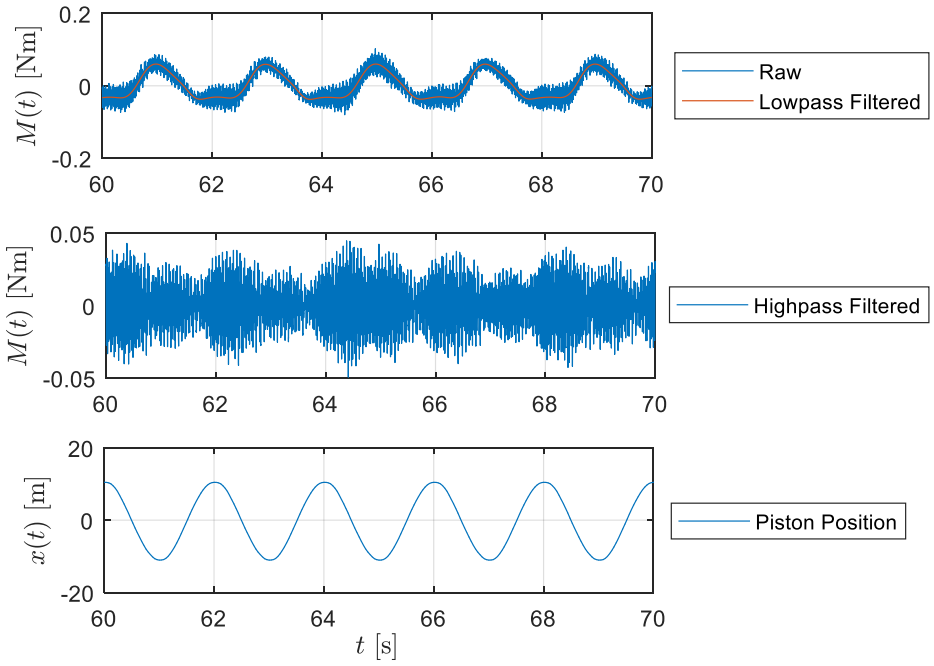

Figure 5-3: Relation of noise in the moment measurements with the wavemaker motion. These results correspond to test F02, corresponding to a wave frequency of 3.142 rad/s.

presented in Figure 5-4 to illustrate the variation of improvement in the numerical predictions resulting from each case.

The numerical results obtained from case 1 in general provide a poor prediction, especially for test IDs F03 and F10. These correspond to the tests where the reflection coefficient K_R is greatest, as shown in Table 5-3. This demonstrates the need to treat the experimental wave system as partially standing, with both incident and reflected wave components. Accounting for the diffracted wave profile using the modified wave reflection analysis appears to be less important, as in most instances case 2, where the Mansard and Funke reflection analysis applied without the model deployed in the tank, results in good numerical predictions of the wave excitation moment.

Nonetheless in a few cases, such as tests F03 and F05, using the modified reflection analysis results in noticeably better numerical predictions of the total wave excitation moment.

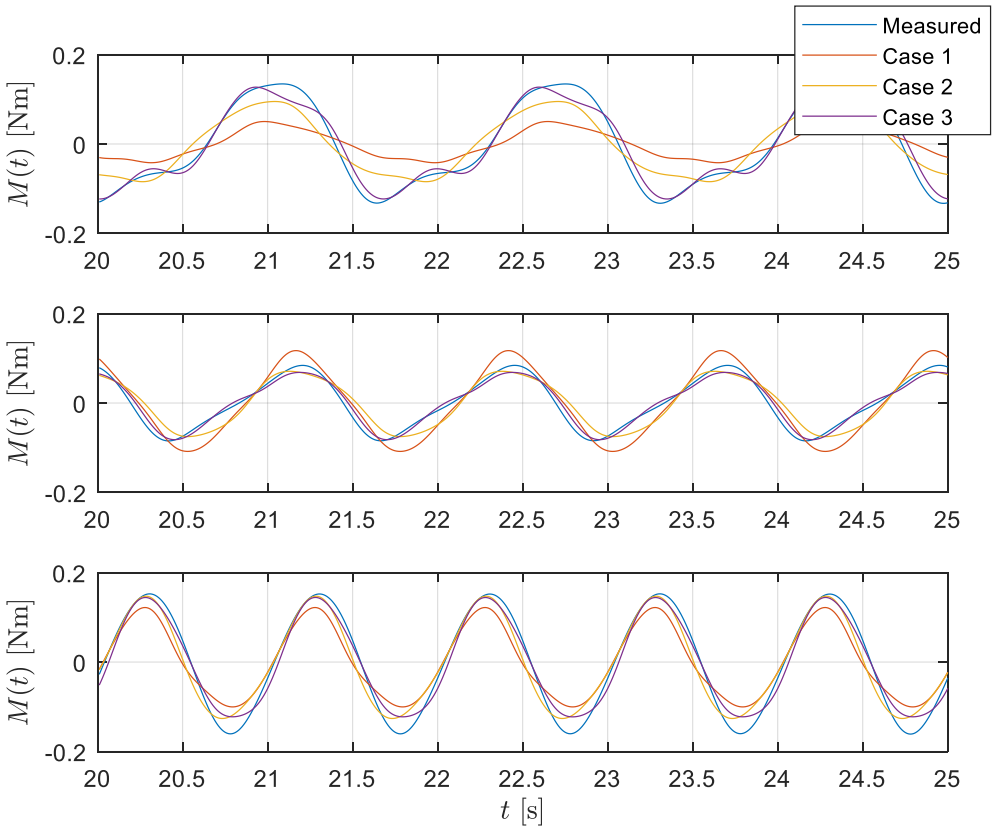

Figure 5-4: Sample numerical wave moment results for three cases, where each case uses a different method for estimating the wave profile at the model location, for test IDs F03, F05 and F07.. The numerical results are compared with lowpass filtered measurements of the wave excitation moment.

5.2.2 Numerical model predictions of wave excitation moment

Numerical predictions for Models 1 to 3 are obtained by simulating each model using the partially standing wave fields resulting from the modified reflection algorithm. The resulting wave excitation moments are then compared to the measured moments from the load cell. Error between the experimental and numerical model results is once again evaluated using Eq. (5.6). Also

computed are the THD for the experimental and numerical excitation moments arising due to harmonic distortion in the regular wave profiles.

Table 5-5 lists the resulting properties for the comparison between numerical and experimental pitch motions. The table also includes the error in the modified reflection algorithm using Eq. (4.18), to observe any correlation between error in the numerical model predictions with error in the reflection algorithm. Overall the numerical results for Models 1, 2 and 3 are very similar, indicating that implementing panel methods for evaluating viscous drag or nonlinear Froude-Krylov has negligible impact on model predictions of the overall wave excitation moment, at least for the range of wave conditions that are considered. Figure 5-5 shows some sample comparisons between experimental and numerical results, with varying levels of relative error, to provide the reader with a visual representation of the parameters in Table 5-3 and Table 5-5. Test F13 was shown in Table 5-5 to be a case where the modified reflection algorithm suffered in establishing the reflected wave amplitudes and frequencies, as evidenced by the poorer excitation moment predictions that resulted when using the reflection algorithm's outputs in Model 1.

Table 5-5: Error in the numerical wave excitation moments for each model. Cells are shaded red based on their magnitude.

Test ID	E_{res}	E_{rel}			THD			
		Model 1	Model 2	Model 3	Measured	Model 1	Model 2	Model 3
F01	0.160	0.138	0.138	0.137	0.091	0.223	0.223	0.223
F02	0.206	0.243	0.243	0.242	0.098	0.086	0.086	0.087
F03	0.154	0.131	0.131	0.128	0.099	0.092	0.092	0.094
F04	0.276	0.156	0.156	0.153	0.045	0.071	0.070	0.071
F05	0.206	0.127	0.127	0.123	0.067	0.056	0.056	0.059
F06	0.361	0.163	0.163	0.159	0.023	0.091	0.091	0.085
F07	0.340	0.127	0.127	0.125	0.002	0.008	0.008	0.008
F08	0.079	0.177	0.178	0.173	0.07	0.185	0.185	0.185
F09	0.190	0.225	0.225	0.225	0.108	0.110	0.110	0.111
F10	0.205	0.198	0.195	0.192	0.228	0.296	0.293	0.303
F11	0.269	0.181	0.181	0.175	0.153	0.084	0.084	0.092
F12	0.165	0.246	0.245	0.238	0.142	0.086	0.085	0.087
F13	0.604	0.304	0.303	0.289	0.071	0.252	0.253	0.222
F14	0.498	0.213	0.212	0.21	0.01	0.037	0.036	0.035

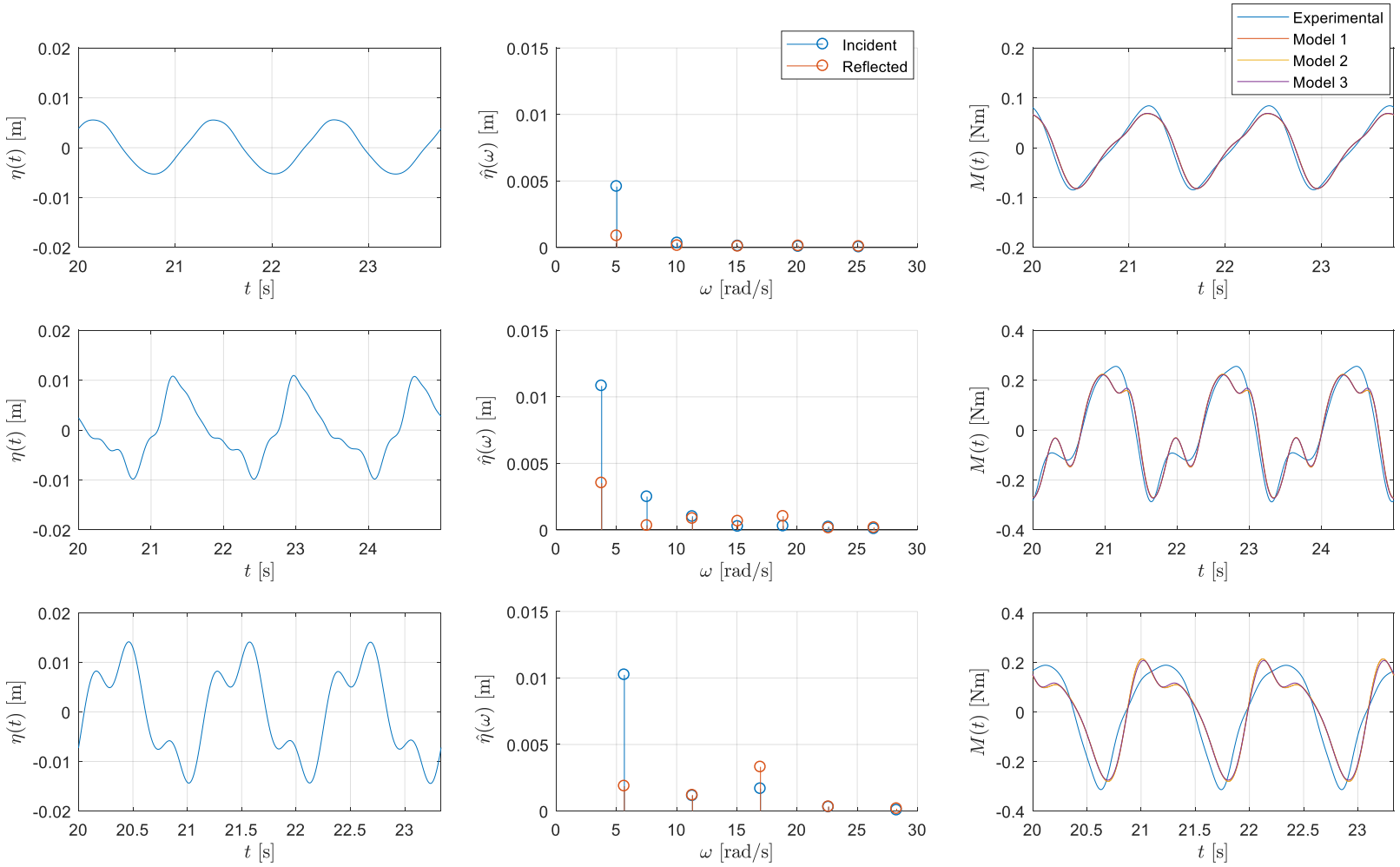

Figure 5-5: Sample experimental and numerical results for excitation moment for test IDs F05, F10, F13. Left column contains the free surface elevation at $x = 0$. Middle column contains the amplitude spectra of the incident and reflected waves. Right column contains the time series of the experimental and numerical results from models 1 to 3.

5.3 Regular Wave Tests

This section considers the full FSI problem in regular waves. The OWSC model is unconstrained and the resulting pitch motion in regular waves is measured and compared to numerical model predictions for Models 1 to 3 developed in Chapter 3. Once again, as with the fixed flap tests, the wave maker is commanded to produce regular waves within the range of frequencies given by Eq. (5.1), however this time waves are generated with nominal wave heights of 1, 2, and 3 cm. Note that not all wave heights can be tested at each frequency due to the limited stroke length of the wavemaker, as shown in Figure 4-8.

Incident and reflected wave amplitudes are again obtained using the modified reflection algorithm discussed in Section , and the wave system is again described by Eq. (1.17). Error and repeatability in the experimental wave profiles is evaluated once again using Eq. (4.8) to (4.10), and the same procedure used in Section 5.2. The resulting experimental wave properties are summarized in Table 5-6. The prefix A and B on the test IDs in Table 5-6 indicate the wave probe configuration for each test, as indicated in Table 4-3. Once again, the experimental wave profiles are very repeatable, therefore like in Section 5.2 the incident and reflected wave amplitude spectra are recalculated over a window of length equal to 10 wave periods to obtain a better estimate of the experimental wave system. The resulting error in the reflection algorithm is again computed using Eq. (4.18).

For this analysis, numerical Models 1 to 3 are simulated without the vertical orientation constraint and with the measured partially standing wave fields. The resulting pitch motions are then compared to the measurement from the rotary position sensor. Relative error between the experimental and numerical models is evaluated once again using Eq. (5.6), this time with the pitch time series:

$$E_{rel} = \frac{\sqrt{\sum_{n=0}^{N-1}\left(\theta_m(nt_s) - \theta_{num}(nt_s)\right)^2}}{N\,|\hat{\theta}_m(\omega^*)|} \tag{5.7}$$

Also computed are the relative error in the pitch amplitudes and the error in the phases of the experimental and numerical results:

$$E_{amp} = \frac{\left|\hat{\theta}_{num}(\omega^*)\right| - \left|\hat{\theta}_{m}(\omega^*)\right|}{\left|\hat{\theta}_{m}(\omega^*)\right|} \tag{5.8}$$

$$E_{phase} = \angle\hat{\theta}_{num}(\omega^*) - \angle\hat{\theta}_{m}(\omega^*) \tag{5.9}$$

Table 5-7 lists the results of the comparison between numerical Models 1 to 3 and the experimental pitch motions. Figure 5-6 and Figure 5-7 present samples of the experimental and numerical results. Figure 5-6 provides results where the relative error between the numerical and experimental models is low, while in contrast Figure 5-7 contains results where the relative error is high. Despite the large error in these results, by observation the numerical and experimental results in Figure 5-7 still appear to agree reasonably well. In addition, the numerical predictions provided by Models 1 to 3 are very similar, indicating that implementing nonlinear Froude-Krylov in Model 1 does not provide a significant benefit towards improving model accuracy.

The largest relative errors appear to coincide with the wave frequencies between 3 and 4 rad/s. Referring to the pitch RAOs in Figure 3-8 and Figure 3-9, these wave frequencies also correspond with the largest pitch motions in regular waves. The largest errors also appear to be related to error in the phase of the pitch motions rather than amplitude. This error could be resulting from the wave reflection analysis, or due to the linear approximation of the wave scattering and radiation moments using potential flow theory provided in Chapter 2. Alternatively, the phase error between the experimentally observed pitch motion and the numerical predictions may indicate that a correction to added inertia due to viscous effects may be required, bearing in mind that a similar correction was required in Section 5.1 to match the experimentally observed and numerically predicted pitch angle decay curves in the OWSC decay tests. Implementing a correction to added inertia to resolve the error in phase is further investigated in Section 5.3.1.

Unlike Table 5-5 for the fixed OWSC tests, Table 5-7 does not include the THD for the experimental and numerical pitch motions because these results were low for all tests. This indicates that the motion of the OWSC model is insensitive to the additional harmonics

observed in the free surface profiles. This observation is used in Section 5.3.2 to estimate the RAO of the model from the experimental results.

Table 5-6: Repeatability of the experimental wave profiles for regular wave tests. Cells representing error are shaded based on their magnitude. Signed cells are shaded blue-orange, and unsigned cells are shaded red. A and B in the test ID refer to the probe configuration.

Test ID	Desired Wave		Mean			Standard Deviation x 10^3		
	ω^*	H^*	E_A	K_R	THD	E_A	K_R	THD
	rad/s	m	-	-	-	-	-	-
A01	2.513	0.010	-0.252	0.061	0.100	0.455	0.392	0.704
B01	2.765		-0.340	0.118	0.131	1.428	1.875	2.537
B02	3.016		-0.033	0.169	0.089	2.861	1.729	5.341
A02	3.142		-0.021	0.164	0.149	1.529	1.689	4.235
B03	3.267		-0.212	0.246	0.160	2.938	1.857	5.325
B04	3.519		-0.305	0.331	0.124	1.226	1.383	3.751
A03	3.770		-0.249	0.399	0.114	0.448	0.593	0.818
B05	3.770		-0.229	0.355	0.106	0.604	1.277	1.307
B06	4.021		0.087	0.191	0.119	0.851	0.575	2.045
A04	4.398		0.104	0.177	0.088	0.692	0.413	1.008
B07	4.398		0.122	0.199	0.090	1.702	0.982	3.229
A05	5.027		-0.024	0.178	0.056	0.635	0.312	0.633
A06	5.655		-0.113	0.177	0.066	0.485	0.871	3.730
A07	6.283		0.042	0.127	0.103	0.615	0.857	3.581
A08	2.513	0.020	-0.218	0.105	0.104	0.817	0.904	1.215
B08	2.765		-0.288	0.082	0.150	1.306	1.484	2.038
B09	3.016		-0.110	0.105	0.084	3.169	2.757	7.956
A09	3.142		-0.067	0.110	0.269	2.904	2.902	16.555
B10	3.267		-0.129	0.221	0.213	2.214	2.176	10.400
B11	3.519		-0.258	0.329	0.112	1.287	1.998	7.895
A10	3.770		-0.165	0.327	0.180	1.914	2.983	4.291
B12	3.770		-0.159	0.341	0.105	1.067	1.441	1.154
B13	4.021		0.024	0.206	0.252	1.305	1.070	3.010
A11	4.398		0.045	0.157	0.174	0.947	0.768	1.325
B14	4.398		0.090	0.170	0.145	0.714	0.477	1.847
A12	5.027		-0.026	0.180	0.069	0.718	0.339	0.707
A13	5.655		-0.112	0.183	0.097	0.508	0.395	1.739
A14	6.283		-0.007	0.137	0.127	1.824	10.456	28.117
B15	3.519	0.030	-0.244	0.328	0.177	1.942	1.467	11.336
B16	3.770		-0.138	0.325	0.110	1.614	2.461	17.581
B17	4.021		-0.018	0.200	0.334	1.483	3.031	5.460
B18	4.021		-0.018	0.199	0.324	1.538	1.924	5.786
B19	4.398		0.026	0.166	0.189	1.233	1.132	4.221
B20	5.027		-0.060	0.115	0.162	1.017	0.835	0.810

Table 5-7: Error between numerical and experimental pitch motions for each model. Cells are shaded based on their magnitude. Signed cells are shaded blue-orange, and unsigned cells are shaded red. A and B in the test ID refer to the probe configuration.

Test ID	E_{res}	E_{amp}			E_{phase} [rad]			E_{rel}		
		Model 1	Model 2	Model 3	Model 1	Model 2	Model 3	Model 1	Model 2	Model 3
A01	0.153	-0.073	-0.073	-0.057	0.150	0.151	0.161	0.118	0.118	0.124
B01	0.200	-0.226	-0.224	-0.196	-0.017	-0.015	0.005	0.161	0.160	0.142
B02	0.460	-0.212	-0.214	-0.185	-0.363	-0.364	-0.310	0.268	0.269	0.238
A02	0.550	-0.094	-0.093	-0.060	-0.386	-0.398	-0.323	0.268	0.276	0.227
B03	0.478	-0.139	-0.136	-0.113	-0.598	-0.608	-0.547	0.398	0.403	0.368
B04	0.302	0.058	0.073	0.069	-0.619	-0.631	-0.568	0.443	0.455	0.412
A03	0.337	0.278	0.305	0.296	-0.365	-0.376	-0.345	0.351	0.371	0.347
B05	0.318	0.166	0.191	0.181	-0.394	-0.405	-0.367	0.321	0.339	0.309
B06	0.408	0.152	0.160	0.152	-0.200	-0.196	-0.180	0.187	0.189	0.177
A04	0.243	0.106	0.105	0.106	0.031	0.028	0.028	0.079	0.078	0.079
B07	0.177	0.051	0.049	0.048	0.001	0.001	0.004	0.037	0.036	0.036
A05	0.221	0.042	0.041	0.034	0.098	0.097	0.099	0.078	0.077	0.077
A06	0.324	0.023	0.023	0.017	0.107	0.106	0.110	0.080	0.079	0.082
A07	0.298	0.021	0.021	0.014	0.090	0.088	0.087	0.072	0.071	0.069
A08	0.117	-0.122	-0.122	-0.099	-0.091	-0.095	-0.068	0.111	0.112	0.106
B08	0.201	-0.185	-0.183	-0.141	-0.313	-0.322	-0.281	0.240	0.245	0.213
B09	0.403	-0.095	-0.095	-0.043	-0.484	-0.494	-0.389	0.330	0.337	0.274
A09	0.823	0.071	0.079	0.156	-0.404	-0.433	-0.285	0.308	0.330	0.252
B10	0.560	-0.014	-0.007	0.021	-0.542	-0.557	-0.389	0.380	0.392	0.281
B11	0.294	0.132	0.159	0.129	-0.462	-0.479	-0.411	0.355	0.377	0.319
A10	0.486	0.308	0.371	0.329	-0.148	-0.151	-0.032	0.251	0.293	0.237
B12	0.470	0.254	0.271	0.209	-0.217	-0.229	-0.201	0.254	0.270	0.222
B13	0.726	0.238	0.271	0.188	-0.174	-0.155	-0.089	0.226	0.236	0.159
A11	0.617	0.249	0.264	0.195	-0.030	-0.026	0.041	0.185	0.195	0.151
B14	0.226	0.183	0.202	0.158	-0.075	-0.065	-0.018	0.147	0.157	0.120
A12	0.190	0.063	0.063	0.051	0.065	0.063	0.073	0.069	0.068	0.067
A13	0.235	0.032	0.031	0.018	0.086	0.084	0.088	0.067	0.066	0.070
A14	0.341	0.028	0.028	0.019	0.079	0.077	0.073	0.108	0.107	0.109
B15	0.428	0.229	0.291	0.220	-0.181	-0.204	-0.087	0.226	0.272	0.186
B16	0.554	0.230	0.333	0.294	0.002	0.010	0.304	0.187	0.249	0.330
B17	0.834	0.221	0.294	0.253	0.032	0.058	0.243	0.172	0.223	0.278
B18	0.882	0.213	0.287	0.237	0.037	0.065	0.247	0.169	0.221	0.277
B19	0.347	0.149	0.195	0.089	0.088	0.103	0.222	0.145	0.174	0.188
B20	0.363	0.043	0.054	0.011	0.038	0.038	0.078	0.066	0.072	0.072

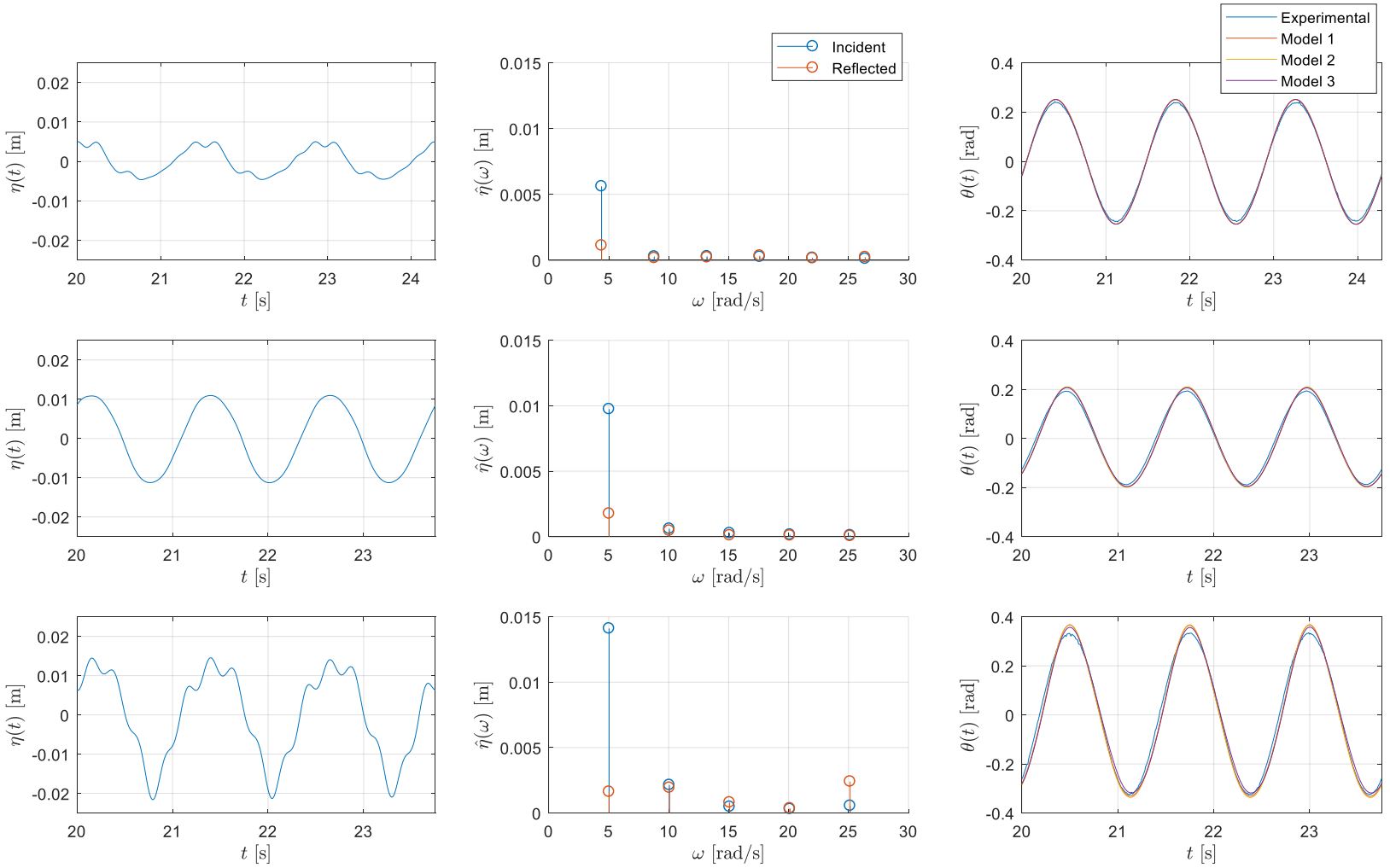

Figure 5-6: Sample regular wave results with low relative error between the numerical and experimental pitch motions. Left column contains the free surface elevation at x = 0. Middle column contains the amplitude spectra of the incident and reflected waves. Right column contains the time series of the experimental and numerical pitch motions for models 1 to 3. Test IDs from top to bottom are: B07, A12, B20.

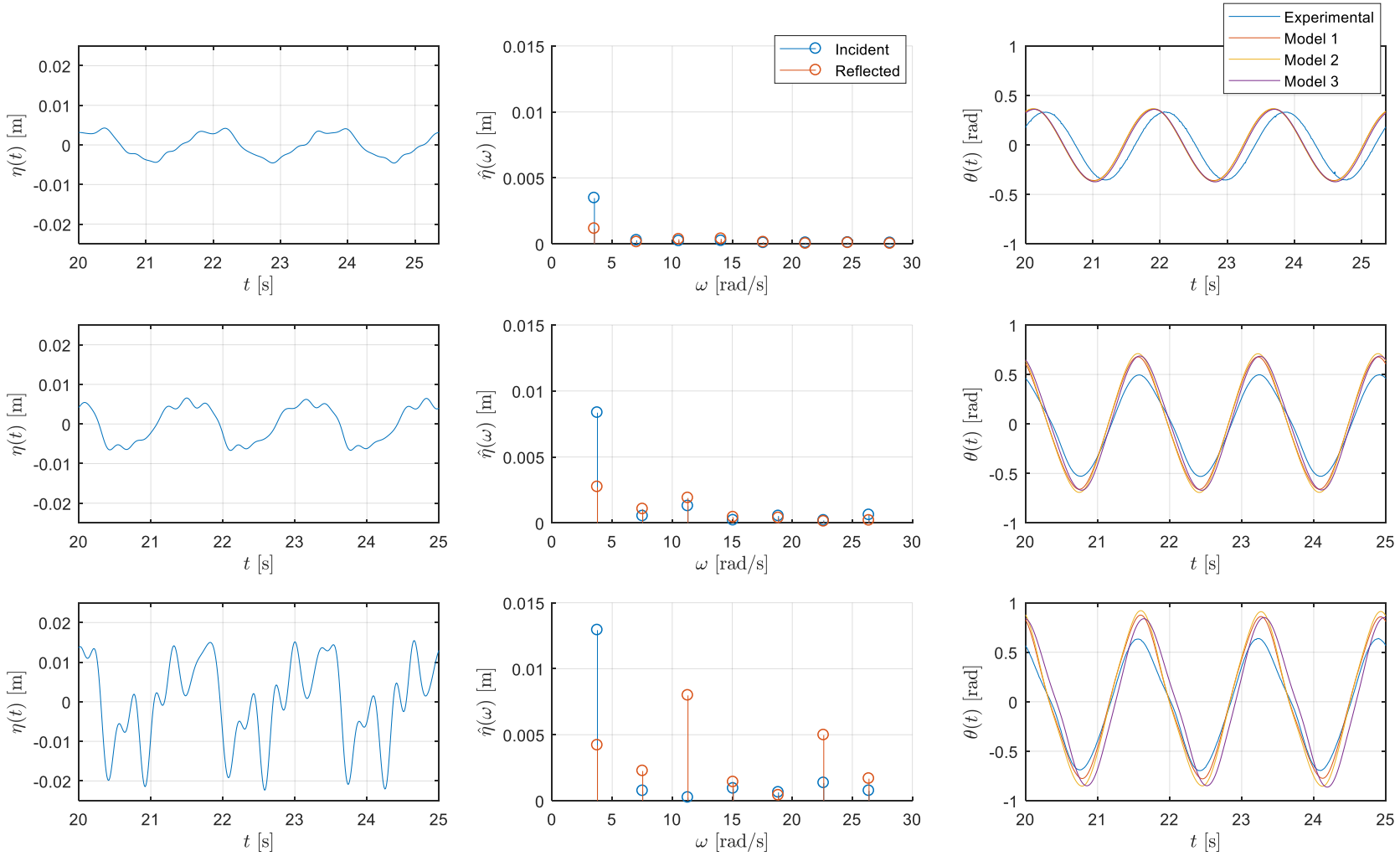

Figure 5-7: Sample regular wave results with high relative error between the numerical and experimental pitch motions. Left column contains the free surface elevation at x = 0. Middle column contains the stacked amplitude spectra of the incident and reflected wave spectra. Right column contains the time series of the experimental and numerical pitch motions for models 1 to 3. Test IDs from top to bottom are: B04, A10, B16.

5.3.1 Correction to added inertia

In Section 1.3.3, which discusses the approximation of viscous loads on OWSCs, it was mentioned that OWSC models typically only use the drag portion of Morison's equation, and the added inertia loads are solved using WAMIT. It was also noted that the validity of this approach is limited to $KC < 10$. While the experimental conditions considered in this thesis meet this requirement (the maximum value for *KC* is under 5) it remains feasible that viscous effects may be significant enough to modify the inertial coefficients obtained from WAMIT such as added inertia.

This section investigates the potential improvements in model predictions for regular wave conditions by incorporating a correction to added inertia for viscous effects. Note however that the accuracy of the presented results should be investigated further, as the error in the regular wave results could also be due to uncertainties in the wave reflection analysis, or due to the linearization of the scattered wave and radiation moments. Therefore, corrections to added inertia should be reinvestigated at a larger model scale, ideally in a tank facility where wave reflections are properly mitigated.

Due to the similarity in numerical predictions provided by Models 1 to 3, corrections to added inertia are only investigated for Model 1, as the corrections are expected to be similar for all models. The correction to added inertia is applied to the infinite added inertia coefficient, and the resulting equation of motion is presented in Eq. (5.5). For each test, the correction to added inertia A^* is obtained by performing a least-squares minimization between the numerical and experimental pitch time series:

$$\min_{A^*} \quad \sum_{n=0}^{N-1} \left(\theta_m(nt_s) - \theta_{num}(nt_s) \right)^2 \tag{5.10}$$

The resulting errors between the experimental and numerical results with and without the correction to added inertia are presented in Table 5-8. Values for A^* from the regular wave tests are listed in Table 5-8 and plotted in Figure 5-8, along with A^* from the decay tests (see Table 5-1). Figure 5-9 presents sample results for tests B04 and B10, where

implementing the correction to added inertia provided the most reduction in relative error E_{rel} .

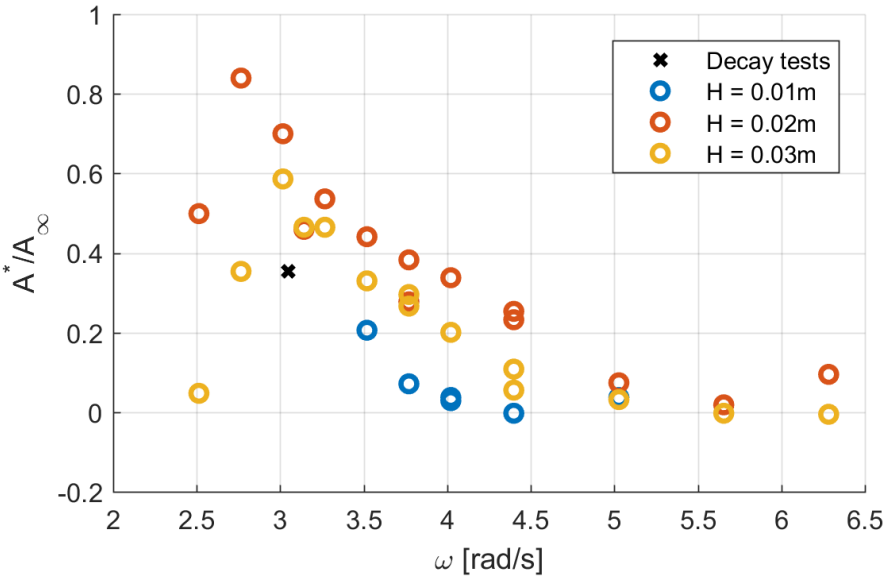

Figure 5-8: Corrected added inertia coefficients from the regular wave and decay tests. Coefficients are normalized by the infinite added inertia coefficient from WAMIT

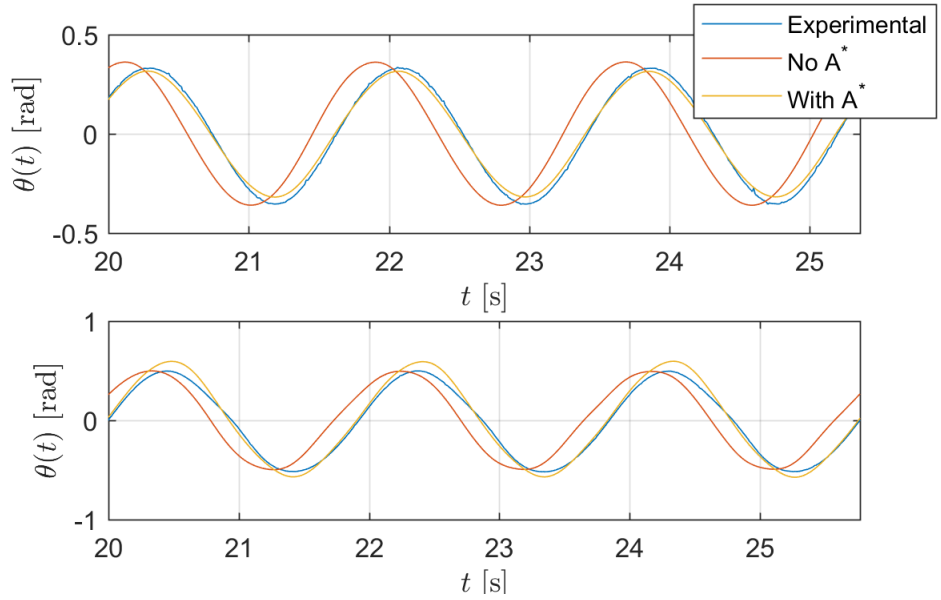

Figure 5-9: Sample regular wave results with and without the correction to added inertia. Test IDs from top to bottom are: B04, B10

Table 5-8: Error in model predictions with and without a correction to added inertia. Results are obtained using Model 1. Cells are shaded based on their magnitude. Signed cells are shaded blue-orange, and unsigned cells are shaded red.

Test ID	E_{res}	$A^* \times 10^3$ [kgm^2]	E_{amp}		E_{phase} [rad/s]		E_{rel}	
			No A^*	With A^*	No A^*	With A^*	No A^*	With A^*
A01	0.153	0.738	-0.073	-0.057	0.150	0.156	0.118	0.117
B01	0.200	5.492	-0.226	-0.070	-0.017	0.100	0.161	0.088
B02	0.460	9.098	-0.212	-0.003	-0.363	0.001	0.268	0.028
A02	0.550	7.213	-0.094	0.072	-0.386	-0.015	0.268	0.061
B03	0.478	7.213	-0.139	-0.051	-0.598	0.002	0.398	0.043
B04	0.302	5.123	0.058	-0.078	-0.619	-0.058	0.443	0.069
A03	0.337	4.590	0.278	0.027	-0.365	0.008	0.351	0.022
B05	0.318	4.139	0.166	-0.049	-0.394	-0.047	0.321	0.051
B06	0.408	3.115	0.152	-0.032	-0.200	-0.024	0.187	0.033
A04	0.243	1.680	0.106	0.033	0.031	0.064	0.079	0.053
B07	0.177	0.861	0.051	0.006	0.001	0.025	0.037	0.020
A05	0.221	0.492	0.042	0.026	0.098	0.102	0.078	0.077
A06	0.324	-0.041	0.023	0.025	0.107	0.106	0.080	0.080
A07	0.298	-0.082	0.021	0.022	0.090	0.089	0.072	0.072
A08	0.117	7.746	-0.122	0.015	-0.091	-0.020	0.111	0.039
B08	0.201	13.033	-0.185	0.068	-0.313	-0.059	0.240	0.077
B09	0.403	10.861	-0.095	0.148	-0.484	-0.044	0.330	0.127
A09	0.823	7.131	0.071	0.227	-0.404	-0.063	0.308	0.185
B10	0.560	8.320	-0.014	0.129	-0.542	-0.018	0.380	0.110
B11	0.294	6.844	0.132	0.117	-0.462	0.014	0.355	0.096
A10	0.486	4.303	0.308	0.248	-0.148	0.085	0.251	0.192
B12	0.470	5.943	0.254	0.131	-0.217	0.076	0.254	0.123
B13	0.726	5.246	0.238	0.096	-0.174	0.066	0.226	0.099
A11	0.617	3.934	0.249	0.080	-0.030	0.104	0.185	0.108
B14	0.226	3.607	0.183	0.053	-0.075	0.048	0.147	0.066
A12	0.190	1.148	0.063	0.028	0.065	0.077	0.069	0.063
A13	0.235	0.287	0.032	0.027	0.086	0.087	0.067	0.067
A14	0.341	1.475	0.028	-0.005	0.079	0.090	0.108	0.105
B15	0.428	3.197	0.229	0.235	-0.181	-0.005	0.226	0.183
B16	0.554	1.107	0.230	0.213	0.002	0.052	0.187	0.181
B17	0.834	0.451	0.221	0.214	0.032	0.055	0.172	0.171
B18	0.882	0.574	0.213	0.203	0.037	0.063	0.169	0.167
B19	0.347	-0.041	0.149	0.151	0.088	0.085	0.145	0.145
B20	0.363	0.574	0.043	0.022	0.038	0.049	0.066	0.065

As expected, implementing a correction to added inertia resolves the error in phase between the experimental and numerical results that were initially observed for wave frequencies between 3 and 4 rad/s, corresponding to the largest pitch motions of the OWSC. In some cases, however, such as test B10 shown in Figure 5-9, implementing the correction to added inertia results in an increase in error in the pitch amplitude predictions.

5.3.2 OWSC response in regular waves

At the end of Chapter 3, in Section 3.5, numerical predictions of the OWSC RAO for each nonlinear model were presented. An equivalent RAO can be derived from the experimental pitch measurements, which can be used to compare experimental and numerical observations of the OWSC motion for all wave heights and frequencies, rather than just the few sample cases shown in Figure 5-6 and Figure 5-7. The pitch RAO is estimated from the experimental measurements by treating the net motion of the model as the superposition of two motions, one due to the incident waves and the other due to the reflected waves. The incident wave RAO is retained for comparing with the numerical RAOs generated in Section 3.5.

Previously it was noted that the measured pitch motions have low THD and are therefore insensitive to the additional harmonics observed in the measured free surface profiles. The additional harmonics in the incident and reflected wave profiles can therefore be ignored so that the incident wave is regular with complex amplitude A_I and the reflected wave is also regular with complex amplitude A_R. The complex pitch amplitude due to the incident waves is then given by:

$$\hat{\theta}_I = A_I\hat{\theta} = (a_I + ib_I)(\alpha + i\beta) \tag{5.11}$$

where $\hat{\theta}$ is the pitch RAO. The complex pitch amplitude due to the reflected waves is related to the complex conjugate of the pitch RAO:

$$\hat{\theta}_R = A_R\,\mathrm{conj}\left\{\hat{\theta}\right\} = (a_R + ib_R)(\alpha - i\beta) \tag{5.12}$$

The summation of these motions is equal to the total measured pitch amplitude $\hat{\theta}_m$:

$$\begin{aligned} \hat{\theta}_m &= A_I\hat{\theta} + A_R\,\mathrm{conj}\left\{\hat{\theta}\right\} \\ \alpha_m + i\beta_m &= (a_I + ib_I)(\alpha + i\beta) + (a_R + ib_R)(\alpha - i\beta) \end{aligned} \tag{5.13}$$

and the real and imaginary components of $\hat{\theta}$ can then be obtained by solving

$$\begin{bmatrix} a_I + a_R & -b_I + b_R \\ b_I + b_R & a_I - a_R \end{bmatrix}\begin{bmatrix} \alpha \\ \beta \end{bmatrix} = \begin{bmatrix} \alpha_m \\ \beta_m \end{bmatrix} \tag{5.14}$$

For a given wave height, Eq. (5.14) is evaluated for all tested frequencies and the resulting RAO is compared to numerical results for Models 1 to 3, without the correction to added inertia discussed in Section 5.3.1. The differences between experimental and numerical RAO curves is primarily attributed to the assumption that pitch amplitude is linearly proportional to wave amplitude, which **Figure** 3-10 illustrates is inaccurate. The nonlinear relation between pitch and wave amplitudes is attributed to the quadratic relation between the viscous drag moment and relative fluid velocity. Because of this relation, deviations between the experimental and numerical RAO curves will increase if the incident wave height deviates from the commanded wave heights of 1, 2 and 3cm. Ultimately, this means if the actual incident wave height is greater than the commanded wave height, then the experimental RAO should lie below the numerical RAO prediction obtained for the commanded wave height, and vice versa.

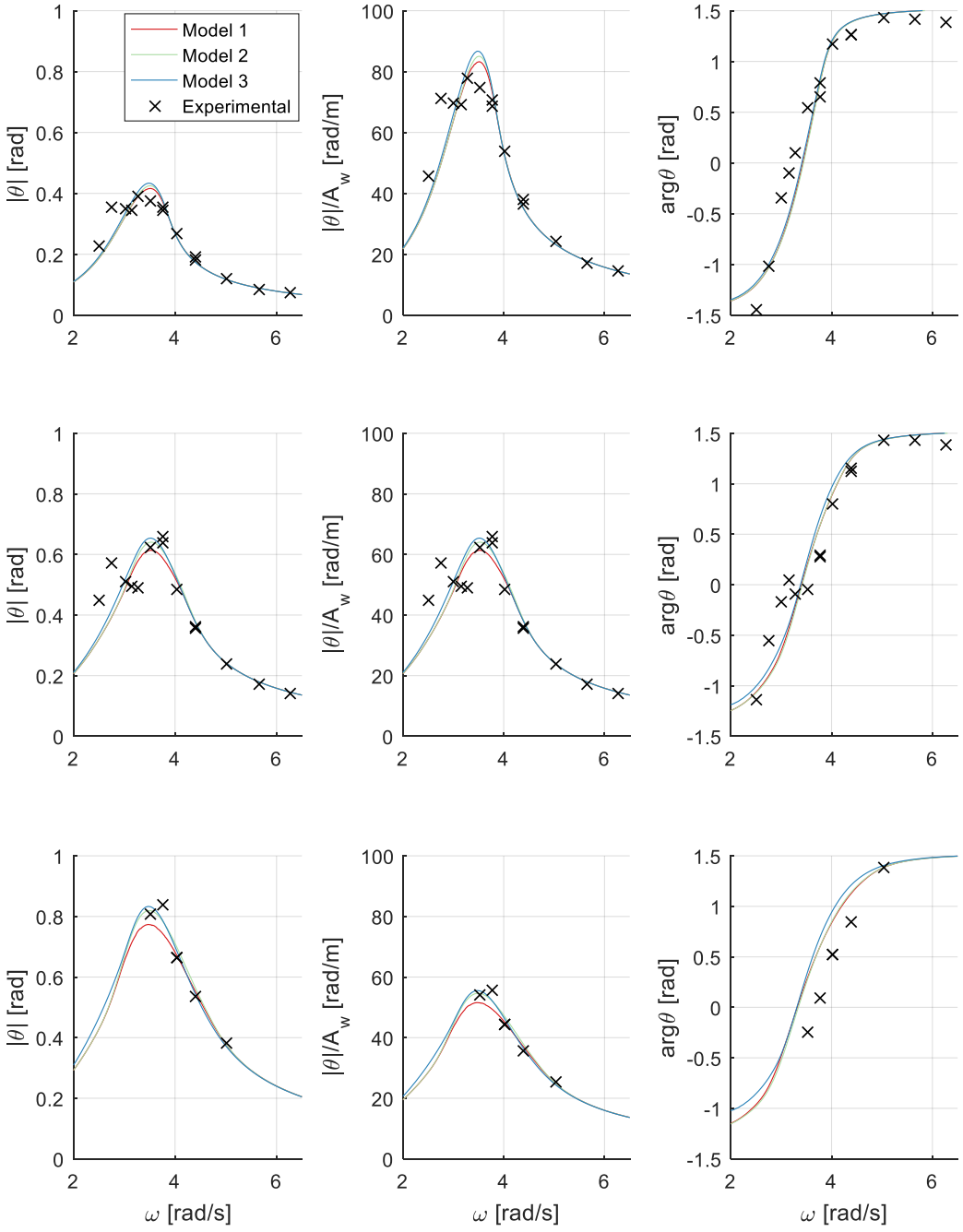

Figure 5-10: Comparison of the experimental results to numerical pitch responses obtained from Models 1 to 3. Model results are obtained with the experimentally derived drag coefficient $C_d = 1.4$. Rows from top to bottom correspond to wave heights of 1, 2 and 3cm. Columns from left to right correspond to the modulus of the pitch motion amplitude, modulus normalized by incident wave amplitude and argument of the pitch motion.

5.4 Irregular Wave Tests

In this section, the full FSI problem is once again considered, this time with the two irregular wave profiles introduced in Section 4.2.2. The results of these tests are used to evaluate the performance of the reflection analysis for irregular wave fields, and to compare each of the numerical models to experimental pitch measurements in irregular conditions. The significant wave height and peak period of the commanded irregular waves are summarized in Table 5-9, and the resulting wave profile is measured using probe configuration B from Table 4-3. The correction to added inertia A^* is not utilized for the numerical simulations.

Table 5-9: Commanded irregular wave properties

Test ID	Significant Wave Height [m]	Peak Period [s]
IRR1	0.015	1.5
IRR2	0.021	1.5

The resulting incident and reflected wave spectra obtained using the modified wave reflection analysis are shown in Figure 5-11. Due to the large peaks in the resulting reflected wave spectra, the spectra were also calculated using the Mansard and Funke algorithm from Eq. (1.15). These spectra are plotted in Figure 5-12 and do not contain the peaks observed in Figure 5-11. Table 5-10 compares the relative error in the two reflection algorithms using a modified definition of Eq. (4.18):

$$E_{res} = \frac{\sqrt{\sum_{p=1}^{4}\sum_{n=1}^{\infty}\left|\varepsilon_n^{(p)}\right|^2}}{H_S} \tag{5.15}$$

Table 5-10: Relative error in the reflection algorithms for the irregular wave tests

Test ID	Mansard and Funke Reflection Algorithm	Modified Reflection Algorithm
IRR1	2.75E-4	1.22E-3
IRR2	4.64E-4	2.68E-3

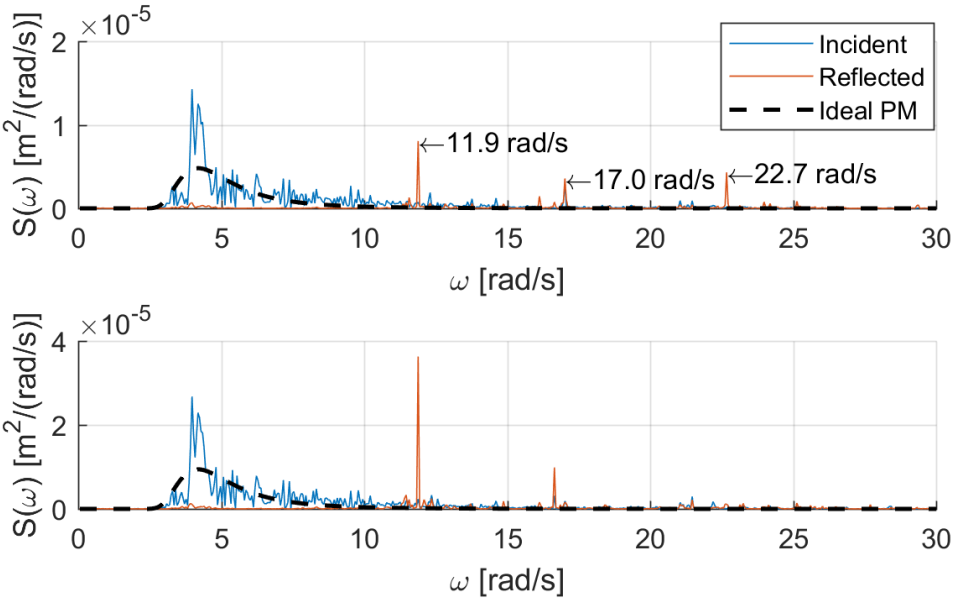

Figure 5-11: Irregular wave spectra using the modified reflection algorithm. Top and bottom figures correspond to IRR1 and IRR2 test IDs. The commanded Pierson-Moskowitz spectral shape is also shown.

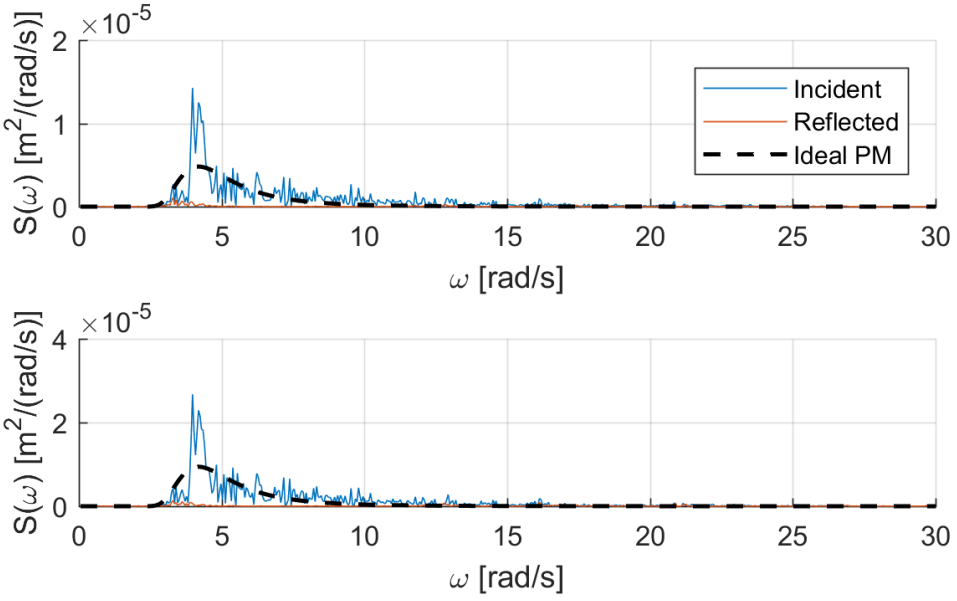

Figure 5-12: Irregular wave spectra using the Mansard and Funke algorithm. Top and bottom figures correspond to IRR1 and IRR2 test IDs. The commanded Pierson-Moskowitz spectral shape is also shown

An investigation into the source of the peaks in Figure 5-11 showed that the wave frequency at each peak corresponds with a local minimum in the magnitude of the determinant of the left-hand matrix of the modified reflection algorithm in Eq. (4.17), denoted here as $\mathbf{A}$:

$$\mathbf{A} = \begin{bmatrix} \sum_{p=1}^{N_p} \left(\hat{\eta}_{D+,n}^{(p)}\right)^2 & \sum_{p=1}^{N_p} \hat{\eta}_{D+,n}^{(p)} \hat{\eta}_{D-,n}^{(p)} \\ \sum_{p=1}^{N_p} \hat{\eta}_{D+,n}^{(p)} \hat{\eta}_{D-,n}^{(p)} & \sum_{p=1}^{N_p} \left(\hat{\eta}_{D-,n}^{(p)}\right)^2 \end{bmatrix} \tag{5.16}$$

The determinant of $\mathbf{A}$ appears as a denominator when solving the reflection algorithms given by Eq. (1.15) and (4.17). Therefore, the peaks in the reflected wave spectrum could be explained by the determinant of $\mathbf{A}$ being close to zero.

Figure 5-13 shows the resulting plot for $|\det(\mathbf{A})|$, along with the equivalent plot for the Mansard and Funke reflection algorithm from Eq. (1.15). The wave frequencies

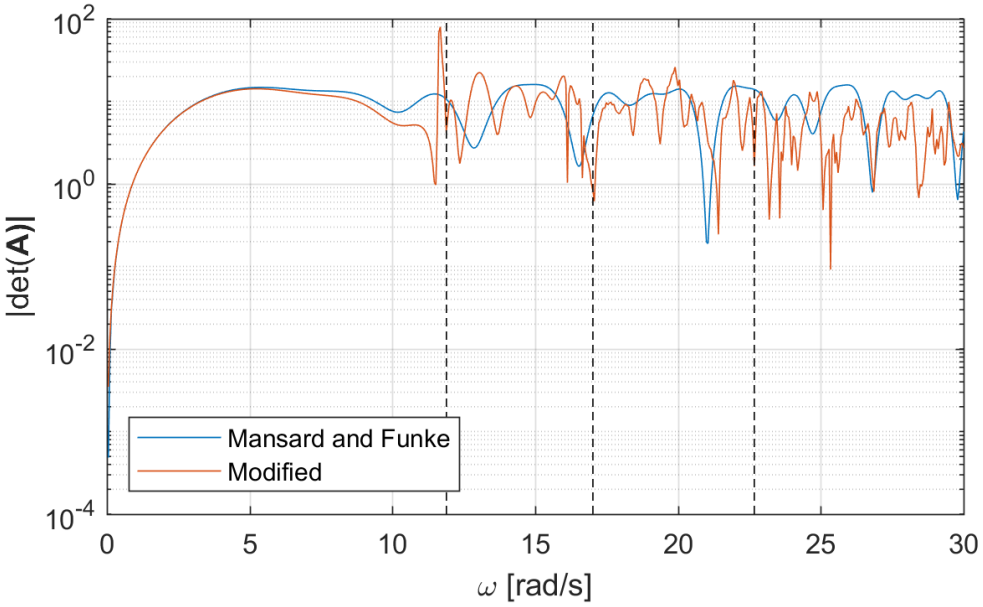

Figure 5-13: Matrix determinants for the modified and Mansard and Funke reflection algorithms. Vertical bars indicate where peaks in the reflected wave spectrum calculated using the modified reflection algorithm were observed.

corresponding to the peaks in Figure 5-11 are also displayed as dashed vertical lines. Note that these frequencies correspond with local minima for the modified reflection algorithm, but not for the Mansard and Funke reflection algorithm. Ultimately this indicates that the modified reflection algorithm is particularly sensitive to wave probe spacing, and a more optimal probe configuration may be required for future irregular wave tests.

Numerical pitch motions for Models 1 to 3 are obtained using the incident and reflected wave spectra from both the Mansard and Funke and the modified reflection algorithms. The error in the resulting pitch responses are evaluated using:

$$E_\theta = \sqrt{\sum_n \left[\hat{\theta}_{num}(\omega_n) - \hat{\theta}_{\exp}(\omega_n) \right]^2} \tag{5.17}$$

and are listed in Table 5-11 for the modified reflection algorithm and Table 5-12 for the Mansard and Funke reflection algorithm. By comparing the error values in each table, it is observed that the Mansard and Funke reflection algorithm results in slightly improved numerical predictions for each candidate model.

Table 5-11: Error in candidate model pitch motions in irregular waves using modified reflection algorithm. Units are in radians.

	MODEL 1	**MODEL 2**	**MODEL 3**
IRR1	0.3265	0.3280	0.3255
IRR2	0.4468	0.4513	0.4500

Table 5-12: Error in candidate model pitch motions in irregular waves using the Mansard and Funke reflection algorithm. Units are in radians.

	MODEL 1	**MODEL 2**	**MODEL 3**
IRR1	0.3182	0.3192	0.3153
IRR2	0.4274	0.4301	0.4285

The experimental and numerical pitch responses for Model 1 are compared in Figure 5-14. Although the pitch response resulting from the Mansard and Funke reflection algorithm has slightly lower error, both pitch responses agree well with experimental observations. This indicates that the peaks observed in the reflected wave spectra produced by the modified reflection algorithm have little impact on the resulting numerical pitch motions.

Table 5-11 and Table 5-12 also indicate that the numerical predictions of the candidate models for the irregular wave tests are very similar. This is further observed in Figure 5-15, which compares the pitch responses obtained from Models 1 to 3 using the wave spectra from the Mansard and Funke reflection algorithm. A sample comparison of the numerical

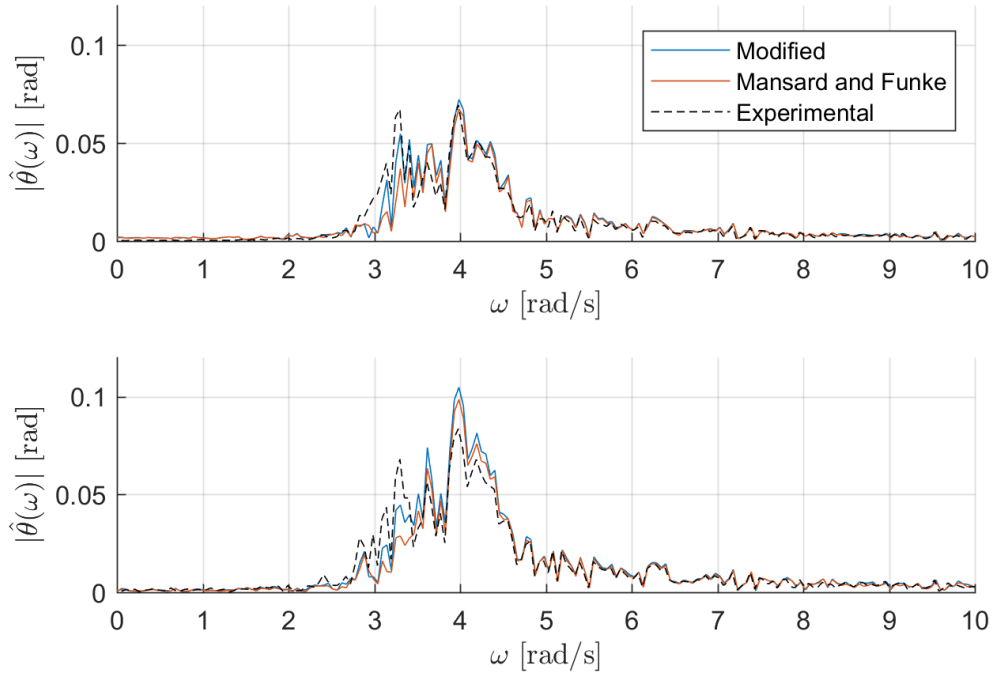

Figure 5-14: Numerical pitch responses for Model 1 using the two reflection algorithms compared with experimental observations. Test IDs from top to bottom are IRR1 and IRR2.

model pitch motions with experimental measurements in the time domain is also provided in Figure 5-16. While some error is observed in the peaks and troughs of the numerical time series, the phases of the time series are generally in good agreement.

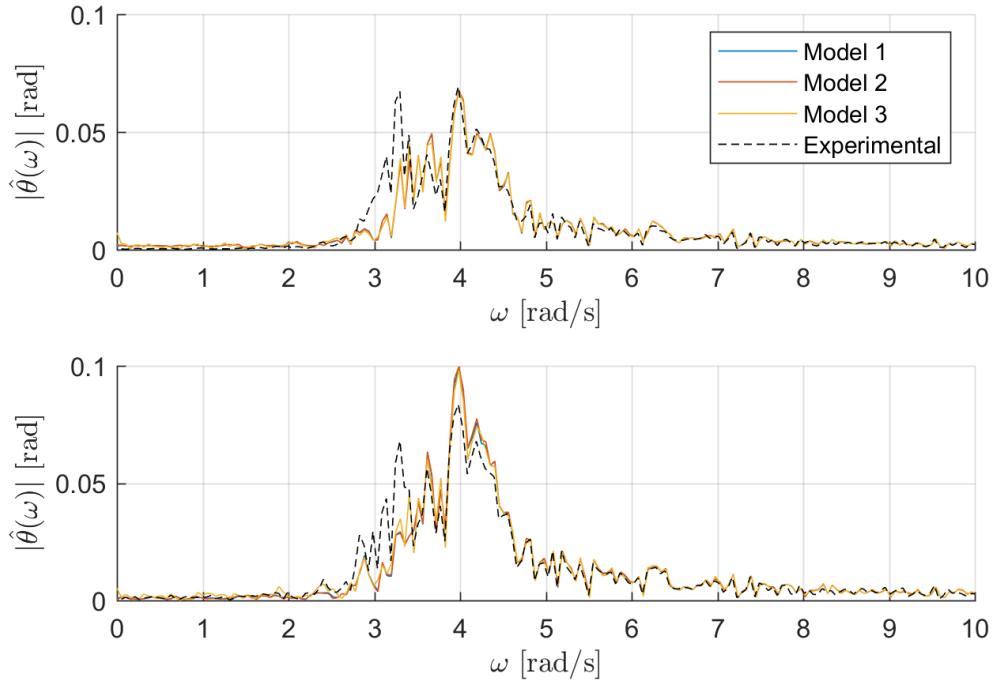

Figure 5-15: Numerical pitch responses for Models 1 to 3 in irregular waves compared with experimental observations. Numerical pitch responses are obtained using wave spectra from the Mansard and Funke reflection algorithm. Test IDs from top to bottom are IRR1 and IRR2.

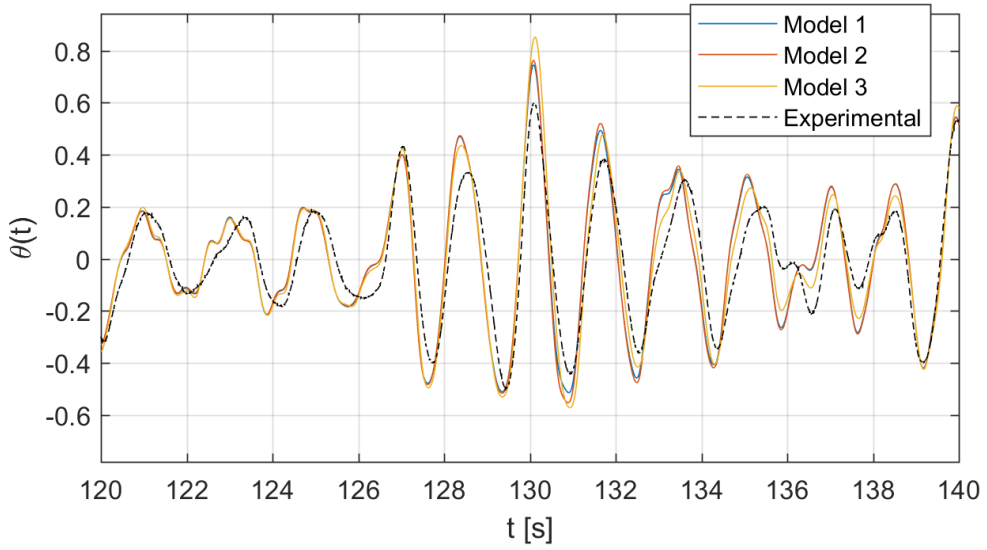

Figure 5-16: Sample comparison of irregular pitch motions from Models 1 to 3 with experimental results for test ID IRR2. Wave spectra input to the numerical models are obtained using the Mansard and Funke reflection algorithm

5.5 Chapter Summary

This chapter presented experimental results obtained with the scale model OWSC in the small-scale flume tank at UVic. Four types of tests were performed, each with different levels of FSI complexity. Decay tests were first performed to estimate the drag coefficient for the candidate numerical models summarized in Table 3-1. For each candidate model, a drag coefficient of 1.4 provided good agreement between numerical and experimental results in terms of the pitch amplitude decay rate. However, a correction to added inertia was required to match the damped decay frequencies of the experimental and numerical pitch motions.

Fixed flap tests were used to demonstrate the utility of the modified reflection algorithm. This was accomplished by comparing numerical predictions for the wave excitation moment from Models 1, 2 and 3 to experimental results for three cases of wave reflection analysis. Cases 1 and 2 utilized conventional techniques for identifying the experimental

wave field from wave probe measurements made without the OWSC model in the tank. Case 3 used the modified reflection algorithm while the model was deployed in the tank. The resulting comparisons demonstrated that the modified reflection analysis provided the best agreement between numerical and experimental results in regular waves, although the amount of improvement varies depending on the significance of wave reflections for a given test.

Numerical predictions from Models 1, 2 and 3 for both fixed and unconstrained tests in regular waves agreed reasonably well with experimental observations. The largest errors in the three candidate model predictions for excitation moment from the fixed OWSC tests corresponded with the largest error in the wave reflection analysis, indicating that the accuracy of the candidate model predictions for wave excitation moment are sensitive to the accuracy of the wave reflection algorithm. The largest errors in the pitch motion predictions for each candidate model in regular waves were observed near the resonant frequency of the device. These errors were associated with a phase offset between the numerical and experimental observations. The magnitude of these phase offsets was similar for all three candidate models. A possible explanation for this error is a perturbation on the prediction of added inertia due to viscous effects (i.e. flow separation and wake formation behind the OWSC). Corrections to the OWSC added inertia were calculated using a least-squares optimization procedure with the regular wave test results. Implementing this correction reduced the average of the relative error E_{rel} between Model 1 and the experimental data (see Table 5-8) from 20% to 9%.

The added inertia corrections are not used for the irregular wave tests and for the remainder of the thesis due to uncertainty as to whether these added inertia corrections are compensating for missing physical phenomena in the numerical models, or compensating error in the experimental data that originates in the wave reflection analysis. In addition, this correction cannot be used in Chapter 6 because the simulations for APP are performed in open ocean conditions, while the added inertia correction is likely influenced by channel effects. The investigation into added inertia corrections is merely intended to indicate there

is possibly a missing hydrodynamic element in the numerical models considered in this work - further investigation is required.

Irregular wave tests were performed to observe the performance of the modified reflection algorithm in irregular wave fields, and to observe the predictions of the three candidate models in realistic ocean sea states. When applying the modified reflection algorithm to the irregular wave data, large spikes in the reflected wave spectra were observed at high frequencies. These spikes are believed to be due to sensitivity of the modified reflection algorithm to the probe spacing used for these tests. The Mansard and Funke reflection algorithm was also applied to the irregular wave data, and did not produce any spikes in the reflected wave data. The incident and reflected wave spectra from both algorithms were used to obtain numerical predictions from Models 1, 2 and 3. All the numerical predictions agreed well with experimental observations, even those obtained using the modified reflection algorithm, indicating that the spikes in the reflected wave spectrum have little influence on the OWSC dynamics.

The numerical predictions from Models 1 to 3 were quite similar for all regular and irregular wave test cases. In Chapter 3, divergence of up to 8% was observed between the candidate model predictions. Similar levels of divergence were observed when simulating the candidate models using the experimental wave fields as inputs. For example, the largest divergence between candidate model predictions of pitch motion amplitude in regular waves was 0.065 rad, observed between Models 1 and 2 for Test ID B16 (incident wave height of 0.03m and frequency of 3.77 rad/s). This divergence is 8% of the pitch motion amplitude predicted by Model 1. The small divergence between the candidate models for the experimental wave conditions makes it difficult to observe which model diverges the least from the experimental data, as the error between the candidate model predictions and the experimental data is generally larger than the divergence between the model predictions. Therefore, a recommended candidate model cannot be selected based solely upon the comparisons of the model predictions with experimental observations.

Chapter 6: Annual Power Production

In this chapter, an idealized passive PTO is incorporated in the candidate OWSC models to estimate the annual power production (APP) of the device at the deployment location introduced in Chapter 4. A braking moment is also added to prevent collisions with the sea floor. The APP is estimated using a matrix of the sea state occurrences for the chosen location given in Table 4-1. The candidate models are used to estimate the mean power production for each sea state by simulating a power production time series for each different sea state within a performance matrix that spans the observed sea state conditions. The annual profile of power production at hourly intervals is then estimated by interpolating the power production estimates with the performance matrix. Optimal values for the PTO damping coefficient for each individual sea state are obtained using the procedure described in Section 6.2.

Obtaining an accurate estimate for mean power in irregular waves requires a 20-minute simulation [50], which is time consuming when performing the numerical surface integration for nonlinear Froude-Krylov and the panel method for drag. Chapters 3 and 5 demonstrated that the differences in numerical predictions between Models 1 to 3 are minor – a maximum divergence of approximately 8% in the predicted response amplitudes was observed, even for incident wave heights up to 0.05m at model scale. Nonetheless, these small differences may result in more notable differences in the APP estimates from the candidate models. However, from hereon Model 2 will not be considered as a candidate model as it provides neither the computational efficiency advantages of Model 1, nor the

more accurate computation of the buoyancy and Froude-Krylov moments using the surface integration of fluid pressure.

Each simulation is carried out at model scale using Froude scaling (see Section 4.2). Significant wave height and wave period are converted to model scale prior to simulating, then the resulting power time series is converted back to full scale. Although viscous drag does not scale per Froude scaling laws, [8] shows that the influence of incorrect scaling of the drag moment on OWSC dynamics is insignificant for model scales down to 1:100. Therefore, each simulation will be carried out using the experimentally derived drag coefficient from Section 5.1. Note that until now, the numerical OWSC models have utilized WAMIT coefficients with wall effects included; from hereon, the corresponding WAMIT coefficients without wall effects will be used.

6.1 Models for Power Production

The numerical OWSC modeling framework developed in Chapter 3 is modified to include an ideal PTO and a braking moment. Since the simulations completed for the APP are for open ocean conditions, channel effects are removed by changing the hydrodynamic coefficients for added inertia, radiation damping and wave excitation to those obtained without channel walls, as discussed in Section 2.3. These changes are implemented to both Models 1 and 3.

An ideal passive PTO model is used in this work, and its moment is given by:

$$M_{PTO}(t) = -\beta\dot{\theta}(t) \tag{6.1}$$

where the optimal PTO coefficient β as a function of incident wave frequency can be estimated based on a linear model of the OWSC [36]:

$$\beta_{opt}(\omega) = \sqrt{B_c(\omega)^2 + \left(\frac{C}{\omega} - \omega\left(I + A_c(\omega)\right)\right)^2} \tag{6.2}$$

To prevent collisions with the seafloor, the braking moment model used by Gomes *et. al.* [11] is used with the parameters specified in Table 6-1 (at model scale). This braking moment is given by:

$$M_b(t) = \begin{cases} 0, & |\theta| \le \theta_{b,i} \\ -\beta_b \dot{\theta} \left(3 \left(\dfrac{|\theta| - \theta_{b,i}}{\theta_{b,f} - \theta_{b,i}} \right)^2 - 2 \left(\dfrac{|\theta| - \theta_{b,i}}{\theta_{b,f} - \theta_{b,i}} \right)^3 \right), & \theta_{b,i} < |\theta| < \theta_{b,f} \\ -\beta_b \dot{\theta}, & |\theta| \ge \theta_{b,f} \end{cases} \quad (6.3)$$

Table 6-1: Braking moment parameters

Parameter	Value
θ_{bi}	30°
θ_{bf}	60°
β_b	1 Nm/(rad/s)

6.2 Optimal PTO Damping

The optimal PTO coefficient given in Eq. (6.2) is derived under linear assumptions. However, incorporating nonlinear effects into the model changes the associated optimal coefficient, as shown in [11]. Therefore, an optimization is performed to maximize the mean power of the OWSC for each bin in the wave histogram given in Table 4-1. This optimization is performed for Models 1 and 3 to obtain a separate set of optimal PTO coefficients for each model. The simulations are performed using regular waves whose height and period match the significant wave heights and energy periods in the histogram.

Figure 6-1

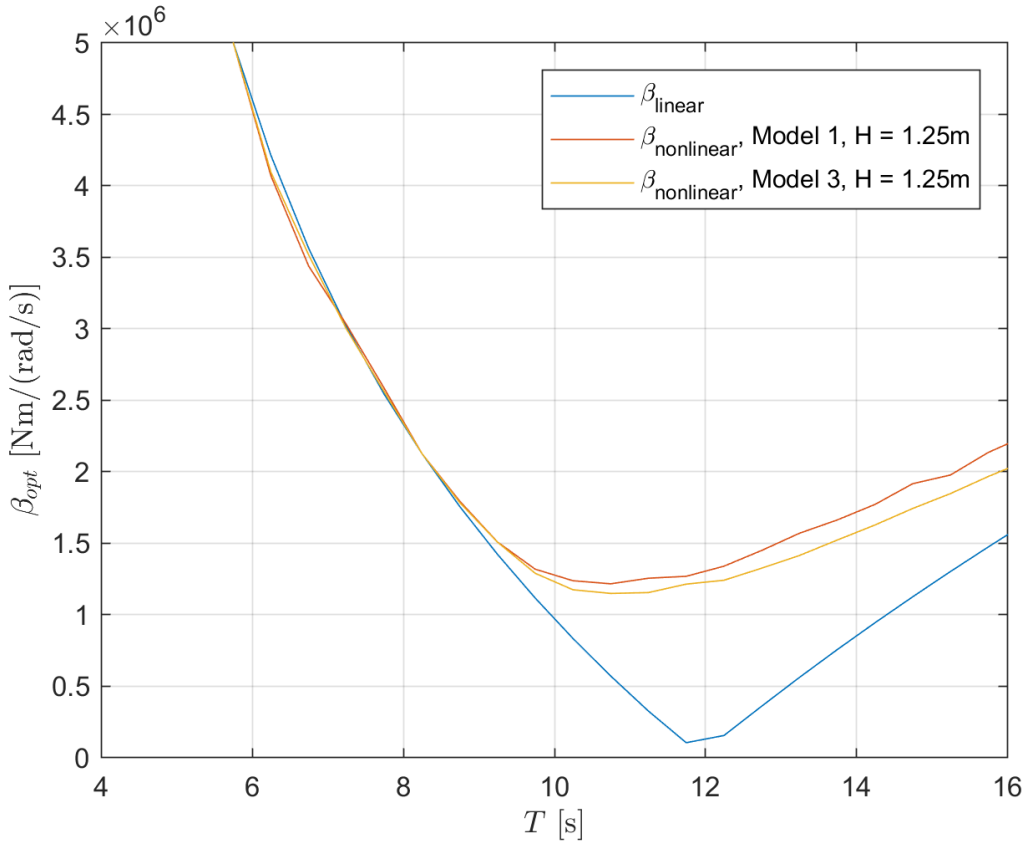

Figure 6-1 shows the PTO damping curve using Eq. (6.2), while Figure 6-2 and Figure 6-3 presents the optimal PTO coefficient values resulting from of the nonlinear optimizations for Models 1 and 3. Sample results from Figure 6-2 and Figure 6-3 for a regular wave height of 1.25m are also compared with the PTO damping curve from Eq. (6.2) in Figure 6-1.

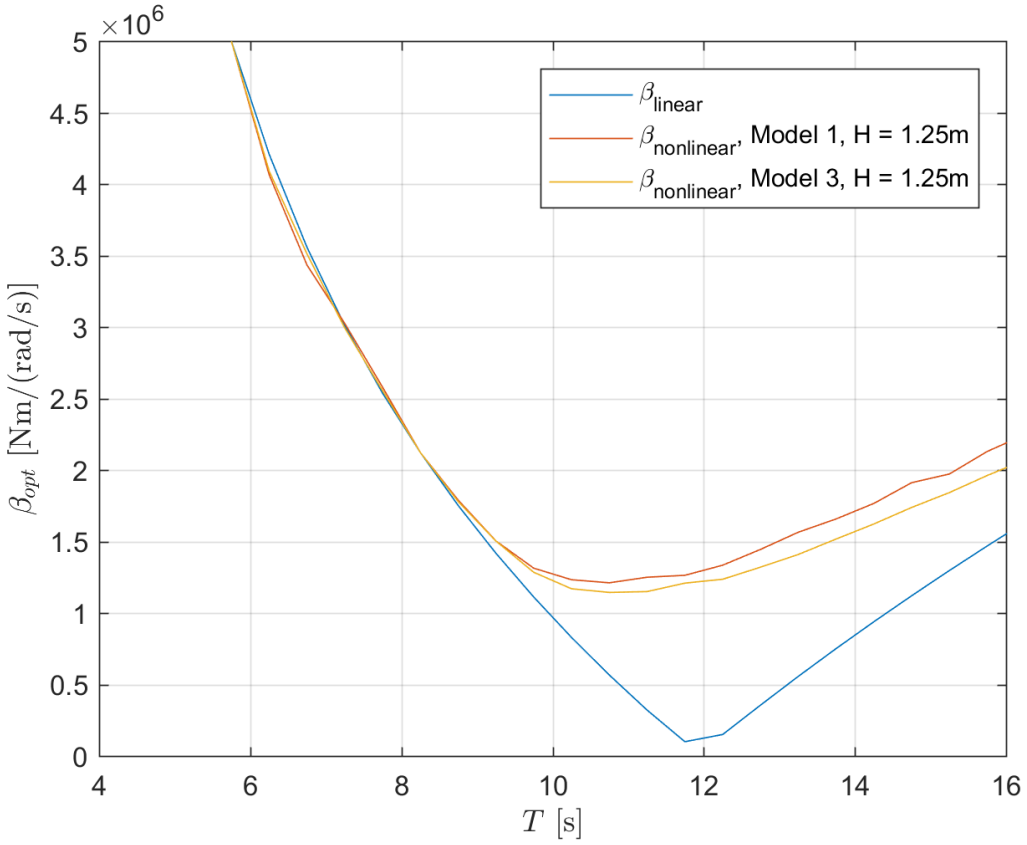

Figure 6-1: Comparison of optimal PTO coefficients from the linear OWSC model with results from the least-squares optimization procedure for Models 1 and 3 with a regular wave height of 1.25m (full scale).

The percent difference between the linear PTO coefficients from Eq. (6.2) and the corresponding values from the least-squares optimization procedure for Models 1 and 3 is also shown in Figure 6-2 and Figure 6-3, and is computed using:

$$E_{\beta} = \frac{|\beta_{nonlinear} - \beta_{linear}|}{\beta_{nonlinear}} \tag{6.4}$$

where β_{linear} are the coefficients obtained from Eq. (6.2) and $\beta_{nonlinear}$ are the coefficients obtained from the nonlinear optimization. Ultimately the linear model always underestimates the optimal PTO coefficient, especially for incident wave periods around 12s.

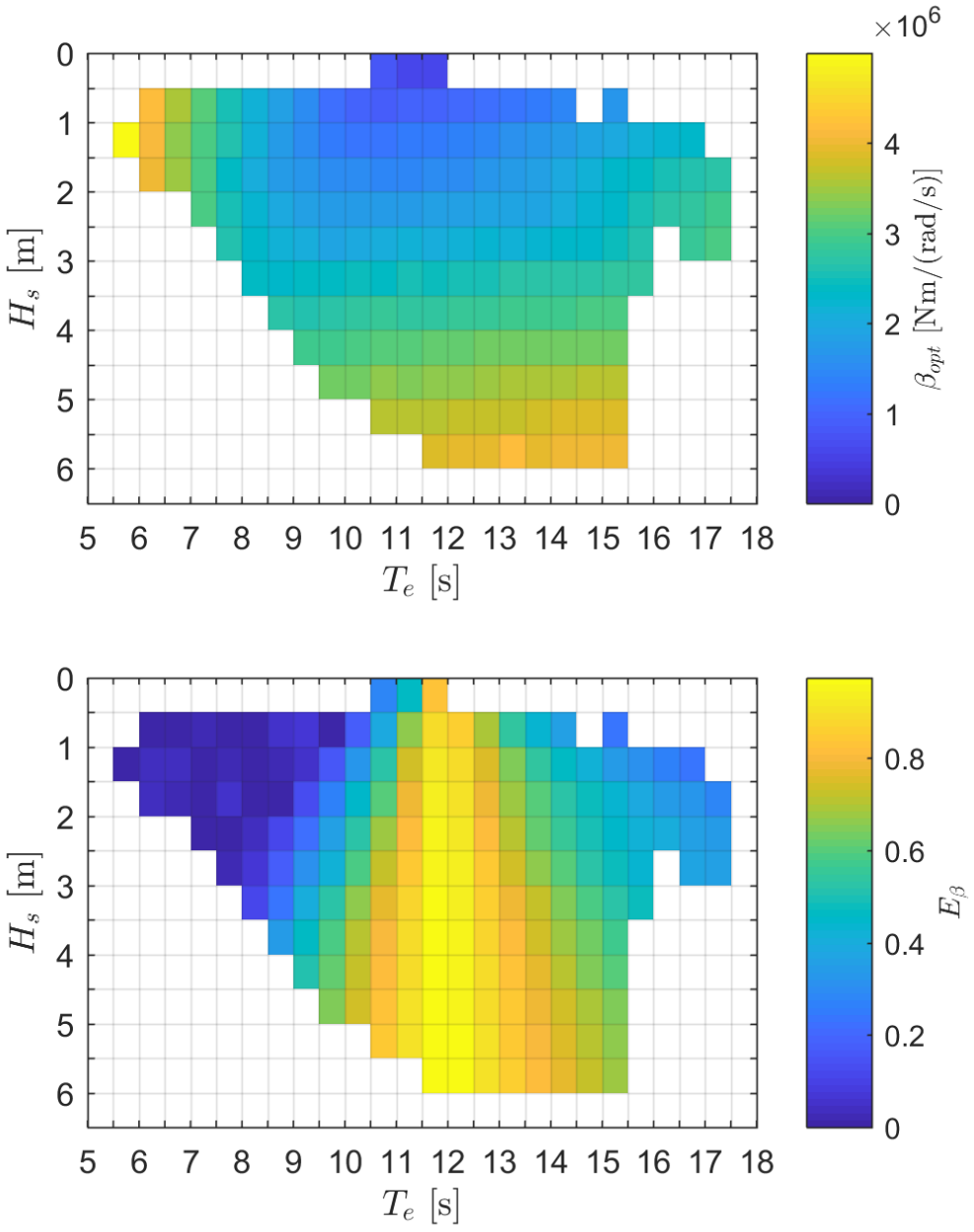

Figure 6-2: PTO coefficients for Model 1 obtained from the optimization procedure. The top figure presents the damping coefficient values at full scale, and the bottom figure presents the percent difference relative to the optimal coefficients obtained from linear theory.

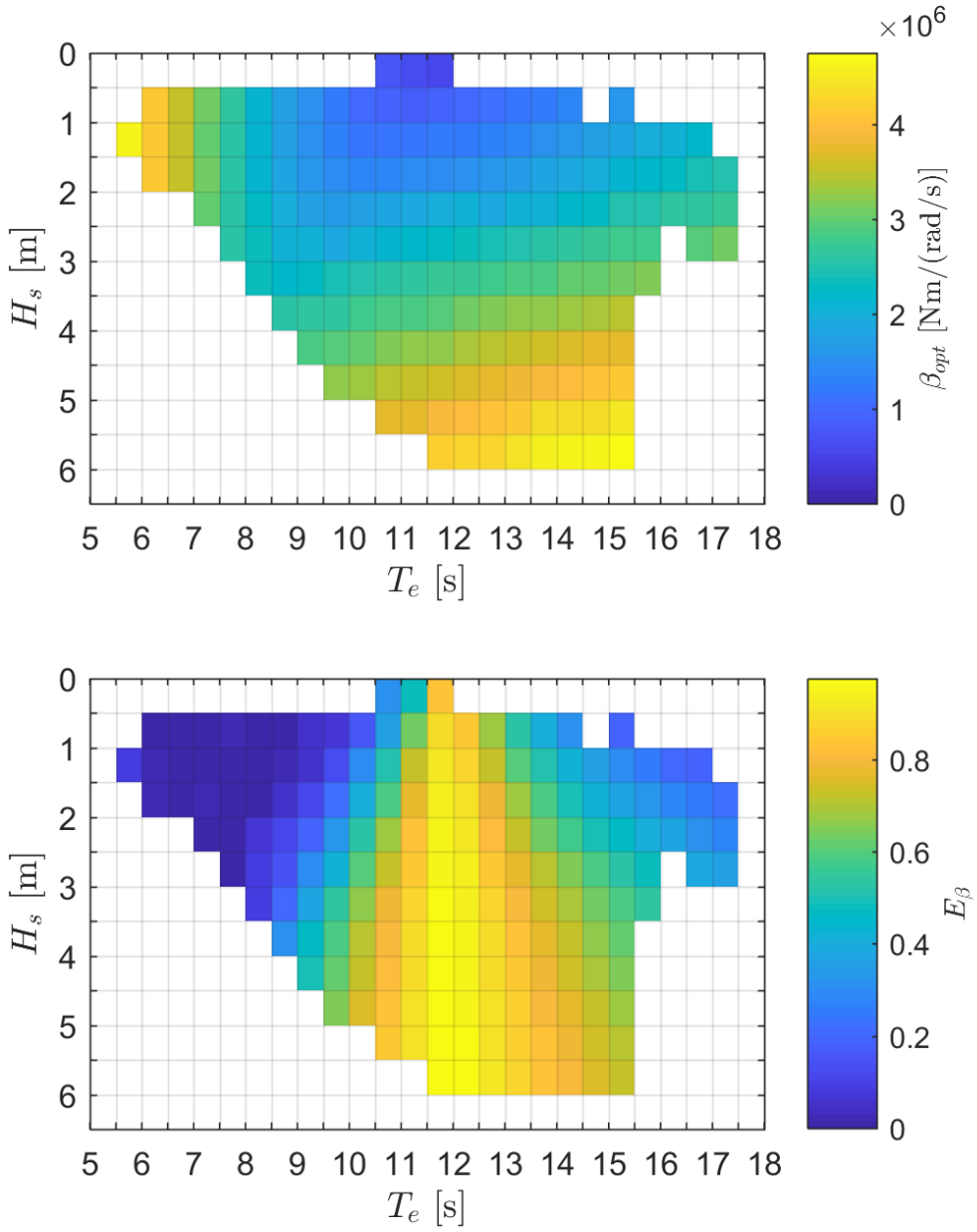

Figure 6-3: PTO coefficients for Model 3 obtained from the optimization procedure. The top figure presents the damping coefficient values at full scale, and the bottom figure presents the percent difference relative to the optimal coefficients obtained from linear theory.

6.3 Power Matrices and Cumulative Power

The mean power for each sea state in Table 4-1 is obtained by simulating the OWSC device using Models 1 and 3 for 25 minutes using the optimal PTO damping coefficients derived in Section 6.2. The first 5 minutes of each simulation are discarded to eliminate any transient effects at the start of the simulation. The resulting mean power estimates for Model 1 are presented in Table 6-3, and results for Model 3 are shown in Table 6-4. Annual power production estimates from each model are then obtained by multiplying each cell with the corresponding value in the wave histogram in Table 4-1 and summing the results. These results are summarized in Table 6-2, along with the capture width L_C non-dimensionalized by the width W (see Figure 2-1) of the OWSC [11]:

$$\frac{L_C}{W} = \frac{\bar{P}}{\bar{P}_w W} \tag{6.5}$$

where $\bar{P}_w$ is the wave power per unit wave crest length given by:

$$\bar{P}_w = \rho g \sum_n C_g(\omega_n) S(\omega_n) \Delta\omega \tag{6.6}$$

C_g is the group velocity of a wave with wavenumber k_n

$$C_g = \frac{1}{2} C_p \left(1 + \frac{2kd}{\sinh(2kd)} \right) \tag{6.7}$$

and C_p is the phase velocity given by

$$C_p = \sqrt{\frac{g}{k} \tanh(kd)} \tag{6.8}$$

Table 6-2: Annual power production and capture width estimates with and without drag. The capture width is non-dimensionalized by the width of the flap W

	APP [MWh/yr]	**Capture Width L_C/W**
Model 1	337	0.208
Model 3	361	0.223

Table 6-3: Power matrix for Model 1, using the experimentally derived drag coefficient. The value in each cell is the mean power production estimate in kW.

Wave Energy Period [s] \ Significant Wave Height [m]	0.25	0.75	1.25	1.75	2.25	2.75	3.25	3.75	4.25	4.75	5.25	5.75	6.25
5.25													
5.75													
6.25		7.5	20.4										
6.75		8.1	20.5	38.3									
7.25		6.9	19.5	38.6									
7.75		7.6	18.9	34.6	55.3	79.9							
8.25		7.9	17.9	35.4	51.8	72.9	107						
8.75		6.7	17.3	32.2	51.0	68.9	94.7	128					
9.25		6.5	17.1	30.4	52.1	69.5	93.3	112					
9.75		6.3	16.6	32.9	44.2	71.6	86.3	109	138	163			
10.25		5.7	15.3	26.1	43.3	64.1	87.2	107	130	164			
10.75	0.9	5.6	15.5	27.2	44.8	61.1	82.5	95.4	130	141	169		
11.25		5.3	13.5	26.3	40.0	51.0	77.5	97.4	113	141	164		
11.75	0.7	5.9	13.5	25.0	36.0	51.9	73.7	87.8	109	145	163	173	
12.25		5.8	11.5	22.1	33.3	45.4	66.5	84.8	97.5	118	141		
12.75		4.5	11.3	24.2	32.9	46.2	59.0	75.8	98.3	117	140	148	
13.25		4.6	10.8	21.0	34.7	46.5	59.9	70.3	86.0	107	132	146	
13.75		5.0	11.2	20.5	31.4	42.2	55.4	76.8	87.6	100	114	133	
14.25		4.3	11.5	16.6	26.7	41.9	50.6	61.3	81.1	96.6	110	125	
14.75			10.1	16.8	25.0	34.6	46.4	64.3	81.4	92.1	102	120	
15.25			9.1	15.8	26.0	34.9	47.6	56.7	69.3	81.5	104	120	
15.75			8.4	15.9	22.6	32.6	45.1						
16.25			8.3	14.5	21.0								
16.75			8.6	13.6		31.4							
17.25						27.8							
17.75													

Table 6-4: Power matrix for Model 3, using the experimentally derived drag coefficient. The value in each cell is the mean power production estimate in kW.

Wave Energy Period [s] \ Significant Wave Height [m]	0.25	0.75	1.25	1.75	2.25	2.75	3.25	3.75	4.25	4.75	5.25	5.75	6.25
5.25													
5.75													
6.25		7.4	19.7										
6.75		8.0	20.0	37.9									
7.25		6.8	19.3	37.8									
7.75		7.4	19.0	33.9	53.8	79.5							
8.25		7.7	17.7	35.3	52.2	75.2	108						
8.75		6.5	17.5	32.3	51.2	69.5	96.4	132					
9.25		6.4	17.2	31.1	53.7	71.8	96.2	116					
9.75		6.3	17.3	34.5	45.7	76.9	91.4	115	148	169			
10.25		5.7	15.7	27.1	46.8	68.0	92.3	116	140	175			
10.75	0.9	5.6	16.5	28.7	47.7	65.9	88.7	104	146	152	187		
11.25		5.4	14.2	28.2	43.3	55.9	83.8	105	122	153	179		
11.75	0.7	6.0	14.0	26.4	38.4	57.6	81.8	96.1	122	159	178	194	
12.25		5.8	12.1	23.8	35.9	50.0	73.9	94.7	108	133	155		
12.75		4.6	11.9	26.3	36.3	51.2	65.7	85.5	112	133	158	163	
13.25		4.7	11.5	23.0	38.3	51.8	67.4	78.9	96.5	123	152	166	
13.75		5.1	11.9	22.3	34.8	47.0	63.9	89.3	101	114	131	149	
14.25		4.4	12.1	17.7	30.0	46.8	57.2	71.5	94.2	116	129	142	
14.75			10.5	18.0	27.8	38.8	54.2	75.4	95.5	107	121	141	
15.25			9.6	17.0	29.5	40.2	56.2	66.3	81.7	98.9	123	143	
15.75			8.6	17.4	25.2	37.1	52.6						
16.25			8.7	16.0	23.3								
16.75			9.1	15.0		36.3							
17.25						32.1							
17.75													

Power production and cumulative energy conversion are plotted in Figure 6-4 and Figure 6-5 using the time series of wave spectra produced by the SWAN model introduced in Chapter 6. The power matrices in Table 6-3 and Table 6-4 are interpolated with time series of H_s and T_e from the SWAN model to obtain the time series of power production over three years shown in Figure 6-4. Cumulative energy conversion for Models 1 and 3 are then obtained by integrating the power production time series.

Divergence in the power outputs predicted by Models 1 and 3 can be observed in the power matrices for each model for sea states with high significant wave heights, as well as in the peaks of the power production time series. Ultimately this leads to a divergence of 24 MWhr/yr in the APP estimates provided by each model. Since Model 3 more accurately represents the overall FSI problem, the APP estimate from Model 3 should be more accurate, and Model 1 therefore under predicts the APP of the OWSC.

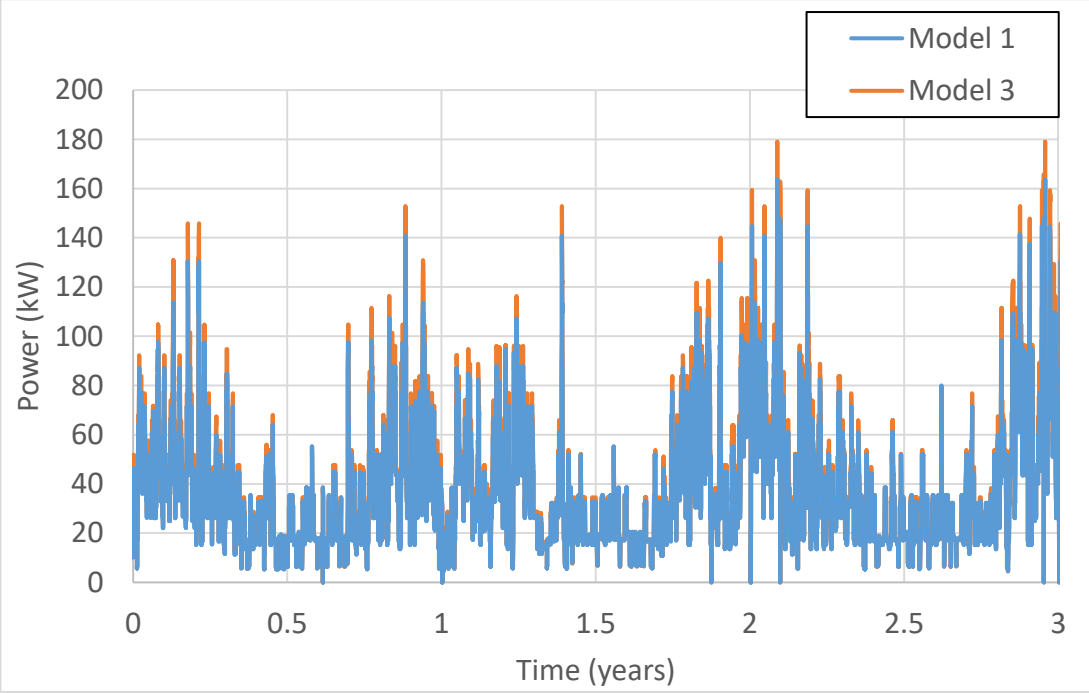

Figure 6-4: Power production over three years predicted by Models 1 and 3

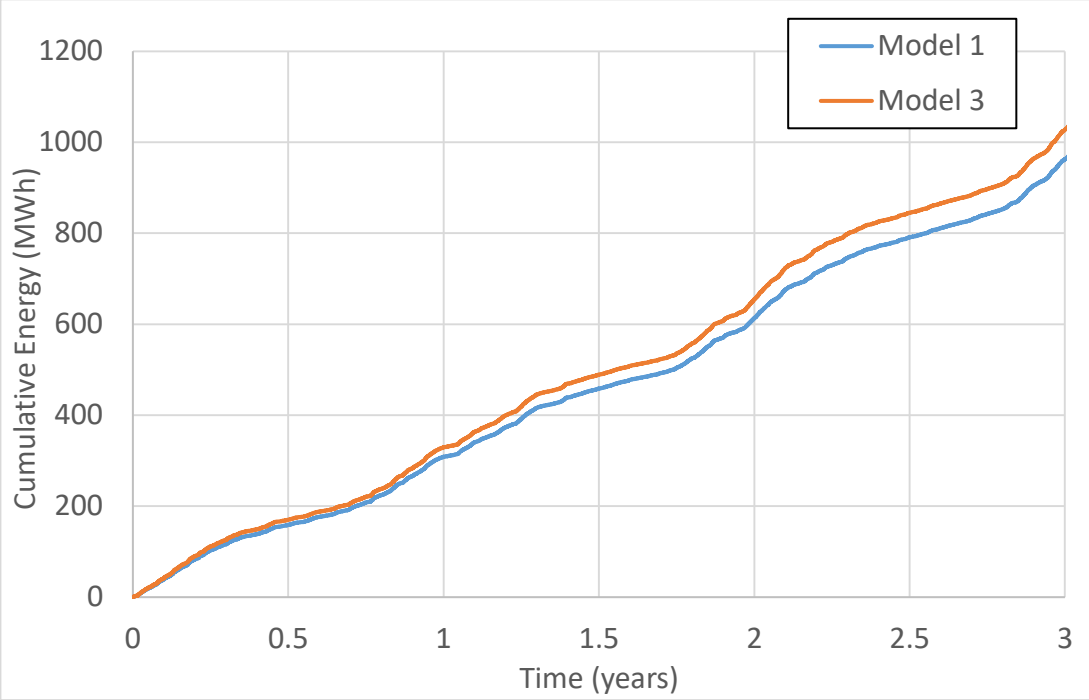

Figure 6-5: Cumulative energy conversion over three years predicted by Models 1 and 3

6.4 Chapter Summary

In this chapter, candidate Models 1 and 3 were modified to estimate APP at the target deployment site. The models were first modified by switching the WAMIT coefficients to values obtained without channel walls. Braking and PTO damping moments were then incorporated in the models. The optimal PTO damping coefficient for each candidate model was estimated by performing a least squares optimization to maximize mean power in regular waves with various amplitudes and frequencies. These coefficients were then used to calculate the power matrix and APP of the OWSC at full scale.

The power matrices for Models 1 and 3 indicated that differences in mean power production estimates from the two models arise as significant wave height increases. This agrees with the observations in Chapter 3, where divergence in the candidate model predictions was observed to increase with wave height. These differences result in a 24 MWh/yr divergence in the APP estimates between Models 1 and 3. Since Model 3

implements the surface integration of total fluid pressure, which provides a more accurate representation of the Froude-Krylov and buoyancy moments (see Section 3.3), the APP estimate from Model 3 is expected to be more accurate. However, note that in Chapter 5 the accuracy of the candidate models was only checked for wave heights up to 0.03m at model scale, or 1.2m full scale. In contrast, referring to the power matrices from Table 6-3 and Table 6-4, divergences in mean power production between Models 1 and 3 can be observed for wave heights greater than 3m. The accuracy of the candidate models should therefore be verified in these large wave height conditions, especially because in these extreme conditions wave slamming events are expected to occur [9].

Selecting a recommended model between Models 1 and 3 are dependent on the time constraints of a given study. If the longer computation times of Model 3 are acceptable, then this model should be implemented as it implements the more accurate algorithm for computing the Froude-Krylov and buoyancy moments, and therefore should provide a more accurate estimate of the OWSC dynamics relative to Model 1. However, if computation time is an issue, then Model 1 can be implemented instead, and the resulting APP can be regarded as a slightly conservative estimate.

Chapter 7: Conclusion

Analyzing experimental data in the small-scale wave flume at UVic presents unique challenges, due to the short length and large wave reflections from the end of the tank. These challenges prevent conventional techniques from being applied to measure the experimental wave system, and required a modified wave reflection algorithm to be implemented. The resulting algorithm was used to provide a recommended numerical modelling approach for a specific OWSC device, which was then used to estimate the APP at a promising deployment site along the west coast of Canada.

The concluding remarks in this section are separated into two parts. First, the required steps for the three contributions of this thesis are summarized, along with the relevant findings. The second part provides recommendations for future work to build upon the contributions of this thesis.

7.1 Contributions

This section summarizes the primary three contributions of the thesis, originally presented in Section 1.4 of the introduction.

1) Develop candidate numerical OWSC models

Three candidate nonlinear OWSC models were considered in this thesis, each incorporating different modelling techniques used in literature. In Chapter 2, the linear model foundation upon which each model is based were developed. Hydrodynamic coefficients were calculated using the BEM software WAMIT. To assess the influence of tank channel walls upon the OWSC dynamics, WAMIT coefficients with and without

channel walls were computed, and the OWSC pitch response using both sets of coefficients were compared. This comparison demonstrated that channel walls have a significant effect on model dynamics, effectively shifting the peak motion frequency of the device, and these effects were necessary to include in the candidate numerical models to accurately compare numerical predictions to experimental data.

Chapter 3 established the algorithms for computing the nonlinear extensions in each candidate model. Model 1 was the same used in [11], Model 2 built upon Model 1 by implementing a panel approach for computing the drag moment, and Model 3 built upon Model 2 by implementing nonlinear extensions to the Froude-Krylov and buoyancy moments. The computational requirements for each model were also estimated. Ultimately Model 1 had the lowest computations since it does not require numerically integrating fluid pressure over the surface of the OWSC. An initial, purely numerical study was conducted to compare the OWSC pitch response amplitude predictions from each candidate model. Divergence between the candidate model predictions was observed to be largest at the resonant frequency of the device, and to increase with incident wave height.

Experimental data collected in a small-scale wave tank at UVic was used as a reference to observe candidate model divergence from the true dynamics of the OWSC device. The results of these experimental/numerical comparisons are further discussed in Contribution 2.

2) Establish methodology for experimental/numerical model comparisons

Due to the short length of the wave tank, and the presence of large amplitude reflected waves from the end of the tank, conventional methods of identifying the experimental wave system resulted in large errors in numerical model predictions. A modified wave reflection algorithm was used to separate the experimental wave field into incident and reflected components. The modified algorithm accounts for the presence of the OWSC body in the tank by utilizing numerical predictions from WAMIT for the radiated and scattered wave elevations.

The utility of the modified reflection algorithm was demonstrated using fixed flap test results, where the OWSC model was fixed vertically and the total wave excitation moment

upon the model was measured. Numerical predictions from the three candidate models for the total moment were obtained for three cases: (1) the free surface at the model location is measured without the model in the tank, and treated as the incident wave; (2) the incident and reflected waves in the tank are identified using the Mansard and Funke reflection algorithm, again without the model in the tank; and (3) the incident and reflected waves in the tank are identified using the modified reflection algorithm, with the model in the tank. Overall the numerical predictions from case 3 best matched the experimental measurements, although the amount of improvement varied and case 2 in general also provided good results.

The modified reflection algorithm was then applied to unconstrained OWSC model tests in both regular and irregular waves, to assess the accuracy of the candidate numerical model predictions. Suitable ranges of wave heights and periods for the experimental studies were established in Chapter 4. Experimental decay tests were also conducted to estimate the drag coefficient for the numerical models, for which a value of 1.4 was obtained. Unfortunately, due to the limited stroke length of the wavemaker, the accuracy of the models could only be assessed in low to moderate wave height conditions, where little divergence between the candidate models occurs. Ultimately there was too much uncertainty in the experimental data to be able to select a recommended model from the three candidates based solely on the experimental/numerical model comparisons.

Overall there was good agreement between the experimental observations and the numerical predictions from the three candidate models. However, the decay and regular wave test results suggested that a correction to the infinite added inertia coefficient may be necessary to compensate for the inviscid flow assumptions applied to added inertia using potential flow theory. For the decay tests, a correction to infinite added inertia was used to match the experimental and numerical decay frequencies. For the regular wave tests, a correction was used to resolve large errors in phase observed between experimental and numerical results at the resonant frequency of the OWSC device. Preliminary estimates for the magnitude of these corrections to infinite added inertia were presented, however these results were not included in the irregular wave experimental analysis, nor when obtaining

APP estimates in Chapter 6. This is due to uncertainty regarding whether the error between experimental and numerical results is due to unmodeled viscous effects, or due to other sources of error for example from the wave reflection algorithm. Further investigation is required to determine whether these corrections should be implemented, ideally by performing further experimental work at a larger model scale and in a wave tank facility with lower wave reflections.

3) Estimate annual power production at a potential OWSC deployment site

The APP of the OWSC device was estimated at a potential deployment site at Florencia Bay on the west coast of Vancouver Island, BC. Initial APP estimates were obtained from candidate Models 1 and 3. Model 2 was dropped as a candidate model at this stage because it requires much longer computation times than Model 1, and yet it does not implement the more accurate representation of the Froude-Krylov and buoyancy moments which Model 3 computes using the numerical surface integration of fluid pressure.

Linear passive damping PTO was incorporated into Models 1 and 3 to represent the power generation process. The optimal damping coefficient for the PTO was determined as a function of incident wave height and period using a nonlinear least-squares optimization procedure. The resulting coefficients for each candidate model were compared with linear theory, and demonstrated the influence of nonlinear modelling techniques on optimal control strategies.

The resulting APP estimates from Models 1 and 3 were 337 and 361 MWh per year, respectively. The APP resulting from Model 3 is considered more accurate as Model 3 implements the more accurate surface integration approach for computing the Froude-Krylov and buoyancy moments. However, for future power assessment studies, it may be desirable to utilize Model 1 instead as it requires significantly less computation time. The resulting APP from Model 1 can then be regarded as a conservative estimate.

7.2 Future Work

This section discusses future work to improve and expand upon the contributions of this thesis, along with some ideas in which the techniques applied in this work can be applied to other avenues of research.

Improvements in the modified wave reflection algorithm

The modified wave reflection algorithm was founded upon the Mansard and Funke reflection algorithm, the accuracy of which is sensitive to the relative spacing of wave probes. Noise in the results of both algorithms can therefore be reduced by using more wave probes. Future experimental investigations in the small-scale wave tank should consider adding more wave probes to provide more accurate estimates of the incident and reflected wave profile.

The modified algorithm is also dependent upon numerical predictions for the radiated and diffracted wave elevations from WAMIT, which are fundamentally based upon small incident wave and body motion amplitudes. The accuracy of these predictions should be assessed, using for example the experimental procedure implemented by McNatt *et. al.* [49] for moderate to high wave heights. In addition, the accuracy of the reflection algorithm could be assessed by using particle image velocimetry (PIV) to measure the fluid velocity in a region of the tank near the OWSC model. The resulting velocity field could then be compared to numerical predictions obtained from the incident and reflected wave fields estimated from the modified reflection algorithm.

Nonlinear extensions to the radiation and wave scattering moments

The nonlinear numerical models used in this thesis only implement nonlinear extensions to the buoyancy and Froude-Krylov moments. However, previous studies such as [14] have shown that the Froude-Krylov moment being less dominant than the radiation and scattering moments for OWSCs. Since the radiation and scattering moments are dominant for OWSCs, implementing nonlinear extensions to these moments may improve the accuracy of model predictions. Extensions to these moments have been developed by [12],

[39], and implementing these extensions may provide better agreement with experimental observations.

Corrections to added inertia

The experimental observations in this thesis hinted that a correction to added inertia may be required in numerical models to more accurately predict OWSC dynamics. However, there is large uncertainty in these results, since the errors in model predictions can also be attributed to uncertainties in the wave reflection algorithm, or due to the linear approximations of the radiation and scattering moments. Corrections to added inertia should therefore be verified at a larger model scale, and ideally without incident waves to eliminate uncertainties associated with the incident wave field. Some examples of tests are:

1. Performing decay tests using torsional springs with different stiffness coefficients to vary the decay frequency of the model. The pitch decay is measured and used to find the added inertia coefficient that matches experimental and numerical model pitch motions.

2. Performing forced oscillation tests, where the OWSC model is moved sinusoidally at different frequencies using a motor. The torque required to perform the motions is measured and compared with numerical model predictions to estimate the added inertia coefficient

Candidate model accuracy in large wave height conditions

The experimental investigations in this work were limited by the stroke length of the wavemaker, which prevented large amplitude waves from being generated. The accuracy of the candidate models should be further assessed in a wave tank capable of generating the entire range of possible wave conditions at the deployment site.

Future experimental work could also involve observing the dynamics of the model under controlled conditions and re-examine the significance of nonlinear extensions for such conditions. By implementing PTO simulation techniques such as those used in [30], [48], a variety of control strategies can be implemented. For each control strategy, the

significance of the nonlinear extensions, along with any potential corrections to added inertia, can be re-assessed.

Bibliography

[1] I. Lopez, J. Andreu, S. Ceballos, I. Martinez De Alegria, and I. Kortabarria, "Review of wave energy technologies and the necessary power-equipment," *Renew. Sustain. Energy Rev.*, vol. 27, pp. 413–434, 2013.

[2] A. Cornett, "A global wave energy resource assessment," *Proc. ISOPE*, vol. 8, pp. 318–326, 2008.

[3] J. Cruz, *Ocean Wave Energy: Current Status and Future Prepectives*. Springer-Verlag Berlin Heidelberg, 2008.

[4] M. Previsic, R. Bedard, and G. Hagerman, "E2I EPRI Assessment: Offshore Wave Energy Conversion Devices," 2004.

[5] A. Babarit, J. Hals, M. J. Muliawan, A. Kurniawan, T. Moan, and J. Krokstad, "Numerical benchmarking study of a selection of wave energy converters," *Renew. Energy*, vol. 41, pp. 44–63, 2012.

[6] M. Folley, A. Henry, and T. Whittaker, "Contrasting the hydrodynamics of heaving and surging wave energy converters," *Eur. Wave Tidal Energy Conf. EWTEC*, pp. 1–7, 2015.

[7] V. Baudry, S. Marrone, A. Babarit, D. Le Touze, and A. H. Clement, "Power matrix assessment and extreme loads estimation on a flap type wave energy converter in front of a dike," *Proc. 11th Eur. Wave Tidal Energy Conf.*, no. August 2016, pp. 1–10, 2015.

[8] "Wave interaction with an oscillating wave surge converter, Part I: Viscous effects," *Ocean Eng.*, vol. 104, pp. 185–203, Aug. 2015.

[9] Y. Wei, T. Abadie, A. Henry, and F. Dias, "Wave interactions with and Oscillating Wave Surge Converter. Part II: Slamming," *Ocean Eng.*, vol. 113, pp. 319–334, 2016.

[10] M. Peñalba Retes, G. Giorgi, and J. V Ringwood, "A Review of non-linear approaches for wave energy converter modelling," *11th Eur. Wave Tidal Energy Conf.*, no. 1, pp. 1–10, 2015.

[11] R. P. F. Gomes, M. F. P. Lopes, J. C. C. Henriques, L. M. C. Gato, and A. F. O. Falcão, "The dynamics and power extraction of bottom-hinged plate wave energy converters in regular and irregular waves," *Ocean Eng.*, vol. 96, pp. 86–99, 2015.

[12] J. Gilloteaux, "Mouvements de grande amplitude d'un corps flottant en fluide parfait . Application a la recuperation de l'energie des vagues. To cite this version : Ecole

Centrale de Nantes Université de Nantes," 2010.

[13] M. Guerinel, A. S. Zurkinden, M. Alves, and J. N. A. Sarmento, "Validation of a Partially Nonlinear Time Domain Model using instantaneous Froude-Krylov and Hydrostatic Forces," *Eur. Wave Tidal Energy Conf. EWTEC*, 2013.

[14] G. Giorgi, M. Penalba, and J. V. Ringwood, "Nonlinear Hydrodynamic Force Relevance for Heaving Point Absorber and Oscillating Surge Converters," in *Proceedings of the 3rd Asian Wave and Tidal Energy Conference*, 2016, no. October, pp. 154–162.

[15] M. Folley, T. Whittaker, and A. Henry, "The effect of water depth on the performance of a small surging wave energy converter," *Ocean Eng.*, vol. 34, no. 8–9, pp. 1265–1274, 2007.

[16] B. Robertson, C. Hiles, E. Luzko, and B. Buckham, "Quantifying the Wave Energy Resource and Farm Siting Opportunities for Western Canada," *Int. Conf. Ocean energy*, vol. 1, no. 250, 2014.

[17] G. Clauss, E. Lehmann, and C. Ostergaard, *Offshore Structures Volume I: Conceptual Design and Hydromechanics*, vol. 1. Springer-Verlag London, 1992.

[18] O. M. Faltinsen, *Sea loads on ships and offshore structures*, vol. 1. 1990.

[19] B. R. D. Robertson, C. E. Hiles, and B. J. Buckham, "Characterizing the near shore wave energy resource on the west coast of Vancouver Island, Canada," *Renew. Energy*, vol. 71, pp. 665–678, 2014.

[20] Det Norske Veritas, "Environmental Conditions and Environmental Loads." DNV-RP-C205, 2010.

[21] R. A. Dean, R. G. and Dalrymple, *Water wave mechanics for engineers and scientists*. Singapore: World Scientific, 1991.

[22] S. Nallayarasu, H. F. Cheong, and N. Jothi Shankar, "Estimation of incident and reflected waves in regular wave experiments," *Ocean Eng.*, vol. 22, no. 1, pp. 77–86, 1995.

[23] E. P. D. Mansard and E. R. Funke, "The Measurement of Incident and Reflected Spectra Using a Least Squares Method," *Proc. 17th Conf. Coast. Eng. Sydney, Aust.*, pp. 154–172, 1980.

[24] J. V Ringwood, G. Bacelli, and F. Fusco, "Energy-Maximizing Control of Wave-Energy Converters: The Development of Control System Technology to Optimize Their Operation," *IEEE Control Syst.*, vol. 34, no. 5, pp. 30–55, 2014.

[25] M. Folley, T. W. T. Whittaker, and J. V. Hoff, “The design of small seabed-mounted bottom-hinged wave energy converters,” *Proc. 7th Eur. Wave Tidal Energy Conf.*, pp. 1–10, 2007.

[26] J. R. Morison, “The Force Distribution Exerted by Surface Waves on Piles,” p. 16, 1953.

[27] J. M. J. Journée and W. W. Massie, *Offshore Hydromechanics*. TU Delft, 2001.

[28] M. A. Bhinder, A. Babarit, L. Gentaz, and P. Ferrant, “Potential time domain model with viscous correction and CFD analysis of a generic surging floating wave energy converter,” *Int. J. Mar. Energy*, vol. 10, pp. 70–96, 2015.

[29] A. J. Caska and T. D. Finnigan, “Hydrodynamic characteristics of a cylindrical bottom-pivoted wave energy absorber,” *Ocean Eng.*, vol. 35, pp. 6–16, 2008.

[30] A. S. Zurkinden, F. Ferri, S. Beatty, J. P. Kofoed, and M. M. Kramer, “Non-linear numerical modeling and experimental testing of a point absorber wave energy converter,” *Ocean Eng.*, vol. 78, pp. 11–21, 2014.

[31] R. Nicoll, C. Wood, and A. Roy, “Comparison of physical model tests with a time domain simulation model of a wave energy converter,” in *ASME 2012 31st International Conference on Ocean, Offshore and Arctic Engineering*, 2012, pp. 1–10.

[32] E. Renzi and F. Dias, “Resonant behaviour of an oscillating wave energy converter in a channel,” *J. Fluid Mech.*, vol. 701, no. 2007, pp. 482–510, 2012.

[33] E. Renzi and F. Dias, “Hydrodynamics of the oscillating wave surge converter in the open ocean,” *Eur. J. Mech. B/Fluids*, vol. 41, pp. 1–10, 2013.

[34] van ’t Hoff, “Hydrodynamic Modelling of the Oscillating Wave Surge Converter,” PhD thesis, Queen’s University of Belfast, 2009.

[35] W. E. Cummins, “The impulse response function and ship motions,” *Schiffstechnik*, vol. 57, no. 9. pp. 101–109, 1962.

[36] J. Falnes, *Ocean Waves and Oscillating Systems*. Cambridge, UK: Cambridge University Press, 2002.

[37] T. Perez and T. I. Fossen, “A Matlab toolbox for parametric identification of radiation-force models of ships and offshore structures,” *Model. Identif. Control*, vol. 30, no. 1, pp. 1–15, 2009.

[38] G. Bacelli, R. Genest, and J. V. Ringwood, “Nonlinear control of flap-type wave energy converter with a non-ideal power take-off system,” *Annu. Rev. Control*, vol.

40, pp. 116–126, 2015.

[39] A. Merigaud and J. Gilloteaux, “A non linear extension for linear doundary element methods in wave energy device modellind,” in *ASME 2012 31st International Conference on Ocean, Offshore and Arctic Engineering*, 2012, pp. 1–7.

[40] D. Logan, *A First Course in the Finite Element Method*, Fourth. Stamford: Cengage Learning, 2006.

[41] H. J. Choi, H. H. Chun, I. R. Park, and J. Kim, “Panel cutting method: New approach to generate panels on a hull in Rankine source potential approximation,” *Int. J. Nav. Archit. Ocean Eng.*, vol. 3, no. 4, pp. 225–232, 2011.

[42] M. S. Longuet-Higgins, “On the Joint Distribution of Wave Periods and Amplitudes in a Random Wave Field,” *Proc. R. Soc. London. A. Math. Phys. Sci.*, vol. 389, no. 1797, pp. 241–258, 1983.

[43] P. Lenee-Bluhm, R. Paasch, and H. T. Özkan-Haller, “Characterizing the wave energy resource of the US Pacific Northwest,” *Renew. Energy*, vol. 36, no. 8, pp. 2106–2119, 2011.

[44] B. Robertson, H. Bailey, D. Clancy, J. Ortiz, and B. Buckham, “Influence of wave resource assessment methodology on wave energy production estimates,” *Renew. Energy*, vol. 86, pp. 1145–1160, 2016.

[45] I. Cho and M. Kim, “Wave absorbing system using inclined perforated plates,” *J. Fluid Mech.*, vol. 608, pp. 1–20, 2008.

[46] M. S. Longuet-Higgins, “On the joint distribution of wave periods and amplitude in random wave field,” *Proc. R. Soc. Lond. A*, vol. 389, no. 1797, pp. 241–258, 1983.

[47] J. C. C. Henriques, M. F. P. Lopes, M. C. Lopes, L. M. C. Gato, and A. Dente, “Design and testing of a non-linear power take-off simulator for a bottom-hinged plate wave energy converter,” *Ocean Eng.*, vol. 38, no. 11–12, pp. 1331–1337, 2011.

[48] S. J. Beatty, M. Hall, B. J. Buckham, P. Wild, and B. Bocking, “Experimental and numerical comparisons of self-reacting point absorber wave energy converters in regular waves,” *Ocean Eng.*, vol. 104, pp. 370–386, 2015.

[49] J. C. McNatt, V. Venugopal, D. Forehand, and G. S. Payne, “Experimental Analysis of Cylindrical Wave Fields,” *Proc. 11th Eur. Wave Tidal Energy Conf., Nantes, Fr.*, pp. 1–10, 2015.

[50] IEC, “Marine energy - Wave, tidal and other wave current converters - Part 100: Electricity producing wave energy converters - Power performance assessment, IEC/TS 62600-100,” 2012.